Anisotropic Dewetting in Ultra-Thin Single-Crystal Silicon-on-Insulator Films

By

David T. Danielson

B.S. Materials Science and Engineering
University of California, Berkeley, 2001

Submitted to the Department of Materials Science and Engineering in Partial Fulfillment of the Requirements for the Degree of

Doctor of Philosophy in Electronic, Photonic and Magnetic Materials
at the
Massachusetts Institute of Technology

February 2008

Signature of Author:_____
Department of Materials Science and Engineering
Nov 20th, 2007

Certified by:_____
Lionel C. Kimerling
Thomas Lord Professor of Materials Science and Engineering
Thesis Supervisor

Accepted by: _____
Samuel M. Allen
POSCO Professor of Physical Metallurgy
Chair, Departmental Committee on Graduate Students

Anisotropic Dewetting in Ultra-Thin Single Crystal Silicon-on-Insulator Films

By

David T. Danielson

Submitted to the Department of Materials Science and Engineering
on November 20th, 2007 in Partial Fulfillment of the Requirements for the
Degree of Doctor of Philosophy in Electronic, Photonic and Magnetic Materials

ABSTRACT

The single crystal silicon-on-insulator thin film materials system represents both an ideal model system for the study of anisotropic thin film dewetting as well as a technologically important system for the development of the next generation of MOSFET devices. The scientific community has misinterpreted the mechanism behind SOI dewetting, attributing it to a stress-driven instability. In this work, we characterize and measure the kinetics and geometry of thermally-activated dewetting in ultra-thin SOI films as a function of SOI thickness, crystallographic patterned-edge orientation, and temperature. Using experimental data and physical reasoning, we strongly argue against the previously existing scientific consensus that SOI dewetting is a stress-driven instability and present a 5-step isotropic surface-energy-driven dewetting model based upon the capillary film edge instability and the generalized Rayleigh instability, in which we integrate existing theories and in addition develop an expression for the edge retraction distance during the initial uniform edge thickening and retraction phase of dewetting at a patterned mesa edge for the first time, predicting a square root dependence with time and an inverse power dependence on film thickness. In our study, we observe and quantify the kinetics of the initial edge retraction dewetting mechanism experimentally for the first time and confirm the square root time dependence and inverse power law film thickness dependence predicted by our new model. We also quantify the edge dewetting front propagation velocity in SOI and determine that it depends on the negative third power of the film thickness, agreeing with the prediction of Jiran and Thompson and with our model. We also extract an activation energy for the edge dewetting front propagation velocity of 2.9±0.3eV, in reasonable agreement with reported values for Si surface diffusion on (111) planes. Furthermore, we present for the first time an anisotropic model for void finger propagation that is able to accurately explain the detailed anisotropic dewetting geometries observed in SOI dewetting. A technique for stabilizing ultra-thin SOI films, dielectric layer edge coverage, is also demonstrated that may prove useful to enable the stabilization of ultra-thin SOI films during fully-depleted SOI transistor fabrication. We also report on the effect of Ge coverage on SOI dewetting kinetics.

Thesis Supervisor: Lionel C. Kimerling
Title: Thomas Lord Professor of Materials Science and Engineering

Acknowledgements

I would like to first and foremost thank my thesis advisors Professor Lionel C. Kimerling and Jurgen Michel for their profound intellectual, emotional, and financial support throughout the course of my thesis work at MIT.

I would also like to thank the other members of my thesis committee, Professors Carl V. Thompson and W. Craig Carter. Professor Thompson's passion and enthusiasm for the topic of dewetting filled my reserves when they were down and his deep knowledge of the field pointed me in the right direction innumerable times. Professor Carter was incredibly helpful in providing a number of insights into the capillary behavior of solid state materials, especially the effects of surface energy anisotropy.

I would also like to thank the many collaborators who were instrumental to the completion of this work. I would like to especially emphasize the support that Intel Corporation provided me in this work. Intel graciously hosted me to work on SOI dewetting at their prestigious Components Research Division in Oregon during the summer of 2005. Furthermore, without the generous supply of state-of-the-art SOI material by Intel, this thesis work would not have been possible. I am particularly indebted to Mohamad Shaheen, Peter Tolchinsky, Joanne Qiu, and Micheal McKeag from Intel for all of their individual efforts as excellent collaborators. I am also forever indebted to the team of staff and fellow graduate students who helped me maintain (and frequently rebuild) the Kimerling EMAT group's UHV-CVD system, upon which this work depended heavily. MIT MTL staff member Bob Bicchieri went above and beyond the call of duty a thousand times and fellow EMAT members Anat Eshed, Jifeng Liu, Nok Jongthammanurak, and Douglas Cannon were an absolute pleasure to work with as I learned how to turn a bolt. I would also like to thank the many members of the MIT MTL staff who were incredibly supportive at every turn during the semiconductor processing required in this work, including Bob Bicchieri, Donal Jamieson, Dave Terry, Paul Tierney, Kurt Broderick, and Bernard Alamiriu. I would specifically like to thank Vicky Diadiuk for always being incredibly supportive and finding solutions when I got lost in the processing matrix maze at MTL.

I would like to thank the "Silicon Wafer Engineering and Defect Science" (SiWEDS) NSF Industry/University Cooperative Research Center for providing significant financial and mentorship support for my thesis work. Through SiWEDS, I got the opportunity to give my first public scientific talk and to become part of a broader scientific community for the first time. I am especially thankful to SiWEDS director and NCSU Professor George Rozgonyi, who has provided me with caring mentorship and direction throughout the course of this work. I would also like to thank the United States Department of Defense for providing me full fellowship support during my first three years at MIT through a National Defense Science & Engineering Graduate Fellowship.

I am also deeply thankful to those individuals whose academic tutelage gave me the basic tools and understanding to allow me to be the scientist I am today. I wholeheartedly thank the Department of Materials Science & Engineering at the University of California,

Berkeley for giving me the best undergraduate materials education I could have ever hoped for. I am particularly thankful to Professors Tim Sands, Ron Gronsky, and Eugene Haller for lighting an academic fire in my mind and in my belly. Most importantly, I would like to thank my undergraduate advisor and beloved mentor from U.C. Berkeley, Professor Andreas M. Glaeser, for everything.

A complete education at MIT is also more than experiments, lectures, characterization, analysis, and writing. At MIT, I learned almost as much about leadership and community development as I did about dewetting. Outside of my research experience at MIT, my experience founding and growing the MIT Energy Club and the MIT Energy Conference has been my one true joy. I only wish that I had the space here to acknowledge and thank the hundreds of MIT students, faculty, and alumni with whom I have had the distinct pleasure to work through the MIT Energy Club. I am immensely thankful to Joost Bonsen for teaching me how to make my passion and ideas become reality; to Nol Browne for teaching me everything I know about business; to Mike Berlinski for being there when no one else was; and to Libby Wayman, Kristian Bodek, Nol Browne, Brian Walsh, Alissa Jones, James Schwartz, and Daniel Enderton for being the best colleagues one could every ask for.

On a more personal note, I would like to thank all of those who offered support of a more emotional nature over the years as I worked toward completing this thesis work. My parents, Paul and Margaret Danielson, offered constant and unwavering love and support through the highs and lows of 6.5 years of PhD research. I thank fellow EMAT colleagues and friends Jifeng Liu, Nok Jongthammanurak, Anu Agarwal, and Jurgen Michel for always being there for me when I needed an ear. Without the ability to complain to and hear the complaints of my fellow grad students and best pals Ryan Williams and Dan Sparacin over the years, I don't think I would have made it. And very importantly, I offer huge thanks to Anu Agarwal and MIT Professor Sam Allen for getting me through my toughest moment.

Table of Contents

Chapter 1:
Introduction

As materials dimensions shrink into the nanoscale, surface effects become increasingly important and will tend to dominate materials behavior in structures with sufficiently small dimensions. This is due to the geometrical fact that the surface area-to-volume ratio of a structure scales with the inverse of the structure's characteristic dimension, r_c, as illustrated in Figure 1.1. For this simple reason, nanoscale structures possess an immense amount of surface energy and thus have an extremely high driving force to evolve morphologically to lower their surface energy. This presents major challenges for the fabrication of ever-shrinking nanodevices and also, interestingly, presents the opportunity to use surface-energy-driven instabilities to fabricate useful nanostructures. Friend or foe: surface-energy-driven morphological evolution will become ever more important as we continue to dive deeper into the realm of nanotechnology.

Dewetting in ultra-thin (< 30nm) silicon-on-insulator (SOI) films has emerged as a very important example of this increased susceptibility of nanometer-scale structures to surface-energy-driven morphological instabilities. This surface-energy-driven layer instability has significant implications both for furthering our understanding of the basic science of surface-energy-driven morphological instabilities, as well as for the development of the next generation of integrated circuit (IC) technology.

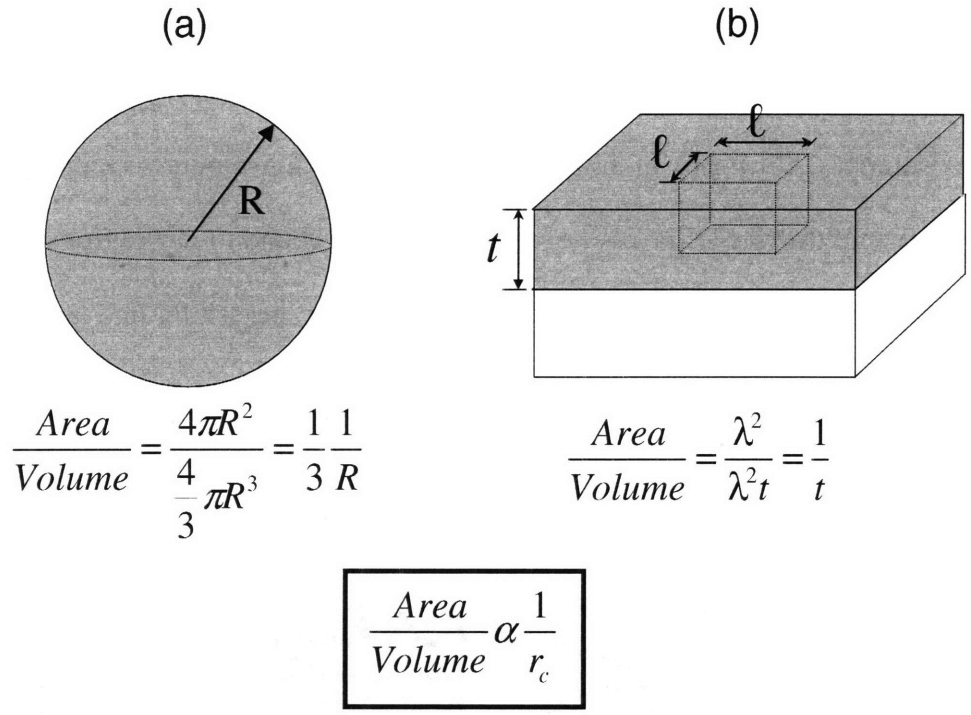

Figure 1.1: Illustration of the increase in the surface area-to-volume ratio with decreasing characteristic materials dimension in: a.) a spherical particle with radius R, and b.) a thin film with thickness *t*. As characteristic materials dimensions shrink into the nanoscale, this simple geometrical effect causes surface effects to dominate materials behavior.

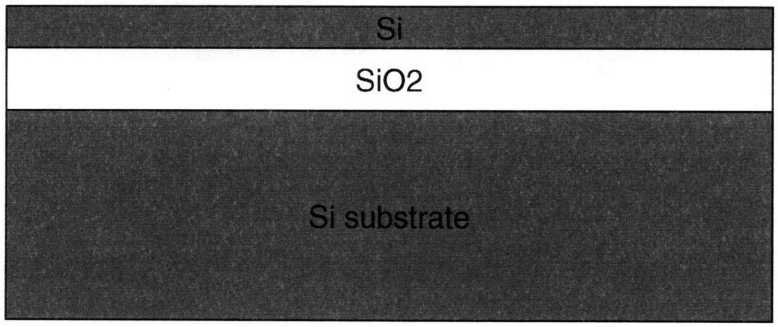

Figure 1.2: Schematic illustration of a silicon-on-insulator (SOI) substrate. The most significant properties of the top Si layer in SOI, from a dewetting perspective, are its single crystallinity and its very low defect density. (Note: The thicknesses of the top Si and SiO_2 layers relative to the underlying Si substrate are grossly exaggerated here for the sake of illustration. Typical thickness values for an ultra-thin SOI substrate are: top Si layer ~ 15nm, SiO_2 layer ~ 145nm, Si substrate ~775μm).

SOI is a multilayer thin film structure consisting of a thin layer of crystalline silicon (Si) atop a layer of thermally grown silicon dioxide (SiO_2) on top of a standard silicon wafer, as illustrated in Figure 1.2. Upon high temperature vacuum annealing, sufficiently thin top Si SOI layers (< 30nm) have been found to dewet from, or uncover, the underlying SiO_2 layer, resulting in the breakdown of the Si film into a discontinuous array of Si fingers and islands, as show in Figure 1.3.[1-11]

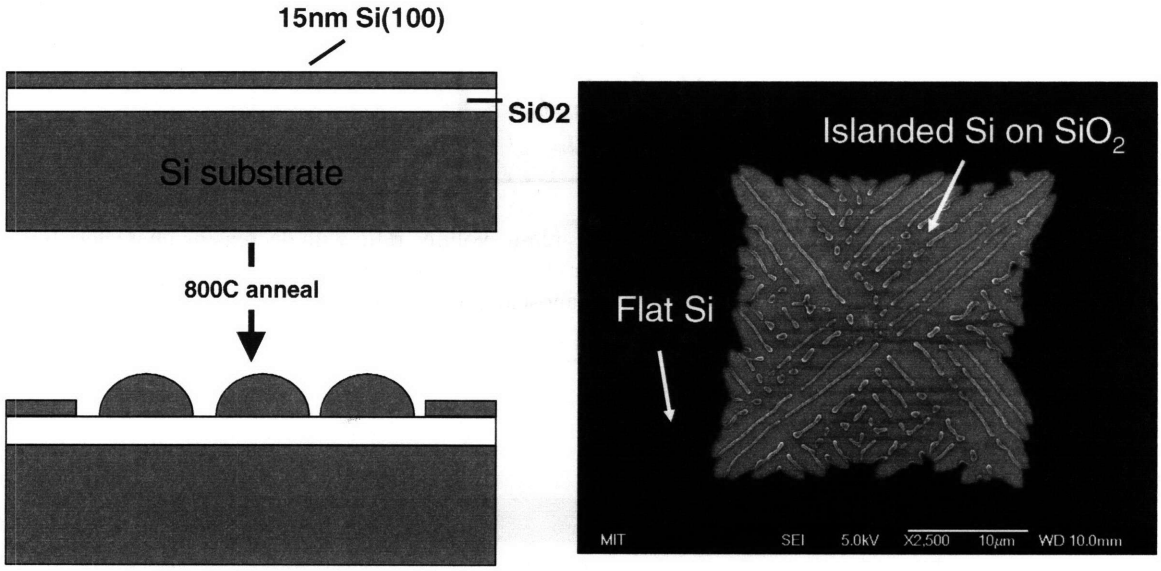

Figure 1.3: Schematic illustration and SEM image of dewetting in an initially continuous, flat 15-nm-thick (100)-oriented top Si SOI layer UHV annealed at 800C for 1360 minutes.

For reference, we provide background here on SOI substrates and how they are made. Fabricating SOI substrates has been a challenge, as the direct epitaxial growth of perfect single-crystal layers on amorphous insulators is not possible. There exist two commercially available types of SOI substrates, termed bonded SOI and SIMOX SOI.

In bonded SOI, a thin single crystal Si layer is transferred to a SiO_2 coated Si wafer using a hydrogen ion implantation/wafer bonding/Si layer exfoliation process. First,

a thin film of SiO_2 is grown on both a "substrate" and a "donor" silicon wafer using thermal oxidation. Hydrogen ions are then implanted into the donor wafer through the SiO_2 layer, such that the peak of the implanted hydrogen concentration is a short distance below the Si wafer's surface. The donor and substrate wafer are then bonded together such that their SiO_2 layers face one another. The bonded sandwich is then annealed at a low temperature (~650C) at which point the hydrogen present in the donor wafer forms hydrogen gas filled microvoids at the depth of maximum hydrogen concentration from the implantation step, which results in crack propagation and exfoliation of the bulk of the donor silicon wafer, leaving a rough thin crystalline silicon film on the substrate wafer. The sandwich is then annealed at high temperature (~1200C) to create a strong bond between the transferred layers and the underlying substrate. The top silicon film is then annealed and polished to create a finished atomically smooth single-crystal bonded SOI wafer. The experimental study of dewetting presented in this thesis focuses on bonded SOI substrates.

SIMOX SOI substrates (standing for "Separation by IMplantation of Oxygen") are fabricated using a quite different process based upon oxygen implantation into a silicon wafer and the subsequent nucleation and lateral growth of a subsurface layer of SiO_2. Oxygen is first implanted into a silicon wafer, creating an oxygen distribution in the wafer with a peak at some desired distance below its surface. The wafer is then annealed at 1200C for a long duration in order to nucleate and laterally grow a buried thin film of SiO_2 beneath a thin crystalline layer of silicon, resulting in a SIMOX SOI substrate. We compare dewetting in bonded and SIMOX wafers in the experimental work presented in this thesis to compare the dewetting behavior of the two substrates.

Here, we briefly motivate and discuss the importance of SOI dewetting from the three distinct perspectives of basic dewetting science, the integrated circuit industry, and the field of nanoscale self assembly.

The Scientific Opportunity

From a scientific perspective, ultra-thin SOI represents an important new materials system available for the study of dewetting science. Ultra-thin SOI is the first single-crystal thin film dewetting materials system ever made available for study, making it an ideal model system for the study of the fundamental physical mechanisms behind thin film dewetting. Model dewetting systems studied until now have been polycrystalline deposited films with high densities of grain boundaries and other defects, as well as grains representing multiple crystalline orientations. This high defectivity and lack of microstructural control has resulted in various types of dewetting behavior being observed in these systems, as discussed in Chapter 2. Furthermore, the underlying anisotropic surface energies present in crystalline Si allow anisotropic dewetting to be observed for the first time in the model SOI dewetting system, presenting us with the unique opportunity to perform a first-of-a-kind experimental and theoretical study of anisotropic dewetting.

The Integrated Circuit Industry Challenge

However, from the perspective of the integrated circuit (IC) industry, ultra-thin SOI dewetting has emerged not as an opportunity, but as a critical process *problem* that threatens to delay or even prevent the scheduled deployment of fully-depleted SOI

transistors.[11,12] This is a critical issue for the industry, as it is relying on the imminent deployment of fully-depleted SOI technology to allow it to continue the exponential improvements in IC performance and cost that have driven the development of the digital age.[12]

The primary reason that such high quality single-crystal SOI substrates are even available for dewetting studies is that the IC industry has been forced to develop SOI substrates in order to enable continued dimensional scaling beyond the "end of the roadmap" for traditional Si substrate-based metal-oxide-semiconductor field effect transistors (MOSFET's) to continue Moore's Law-type industry growth, a long time exponential industry trend in which the number of transistors per chip has doubled every 2 years.[13] According to the International Technology Roadmap for Semiconductors, the use of fully-depleted SOI transistors based upon "ultra-thin" top Si layers (defined as having top Si layer thickness < 10nm) will be required to deploy the state-of-the-art 45nm IC technology node in 2010.[12]

In order to motivate the industrial significance of the development of a fundamental understanding of SOI dewetting, along with techniques for its suppression, we explain here why ultra-thin SOI technology is needed by the IC industry and why SOI dewetting has become a critical process problem for the industry.

During operation of a MOSFET device, a constant voltage is applied between the source and drain electrodes across the device channel (See Figure 1.4 for a labeled schematic of a MOSFET device). The voltage applied to the gate electrode controls whether the channel is conducting or not and thus whether current flows through the

device or not (representing either a "1" or "0" in binary code). When an appropriate non-zero gate voltage is applied, the channel is made conducting and significant current flows

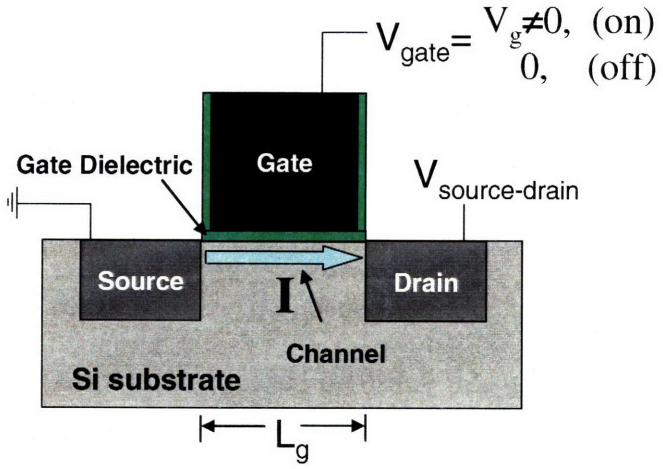

Figure 1.4: Schematic of a traditional Si-substrate based MOSFET device.

through the device ("1" or "on" state); when zero gate voltage is applied, the channel does not conduct and a very low current flows through the device ("0" or "off" state).

The IC industry has almost exclusively used a scaling down of the MOSFET device gate length (L_g) to enable the exponential increases in operating speeds and device integration density that have driven Moore's Law performance growth. However, as the industry looks toward the development of its next technology generation (the 45nm technology node) having a gate length (L_g) of 18nm, it has run up against a fundamental device problem that requires a move away from traditional Si substrate based devices. When the gate length is shrunk down to ~20nm and below, the device gate electrode begins to lose control of the conductivity of the channel, yielding control to the source and drain electrodes and to the channel itself (termed "short channel effects"). The loss of control of the channel to the source and drain electrodes results in a choking off of the device current, while the loss of control to the channel itself causes the current to not

completely turn off when the device is in the "off state", resulting in unacceptable off-state current and power dissipation. Furthermore, the capacitances between the source/substrate and drain/substrate begin to limit the operating speed of the device.

Moving to fully-depleted SOI transistor technology increases the electrostatic integrity of deeply-scaled MOSFET's, reducing or eliminating short channel effects. In fully-depleted SOI MOSFET's, the gate regains control over the channel: reducing the choking off of device current by the source/drain, providing nearly ideal off-state currents, and allowing for high speed operation by eliminating the source/substrate and drain/substrate capacitances.

In order for SOI-based transistors to be fully-depleted, the top Si thickness must be ≤ 0.3 times the physical gate length (L_g). As seen in Table 1.1, this means that fully-depleted SOI transistors at the upcoming 45nm technology node will require the use of SOI substrates with 6.2nm-thick top Si layers; while the 22nm technology node, scheduled to be deployed less than 10 years from now, will require top Si layers as vanishingly thin as 2.7nm (only 20 atomic layers of Si thick!).[12]

Year of Implementation	2007	2010	2013	2016
Technology Node (nm)	65	45	32	22
Actual Gate Length (nm)	25	18	13	9
Fully-Depleted SOI Top Si Layer Thickness (nm)	N/A	6.2	4.4	2.7

Table 1.1: Future MOSFET technology nodes with expected year of implementation and required top Si SOI layer thickness for fully-depleted SOI according to the ITRS.[12]

However, these extremely thin top Si layers required for the coming generations of fully-depleted SOI MOSFET's at and beyond the 45nm technology node have been found to be highly morphologically unstable to dewetting when vacuum processed at high temperature, making successful device processing using traditional semiconductor processes impossible.

The standard semiconductor processing step during which ultra-thin SOI films have been found to be the most susceptible to dewetting is the raised source/drain selective silicon epitaxy step. In order to maintain a tolerably low series resistance in ultra-thin SOI-based MOSFET's, elevated source/drain structures must be grown to locally thicken the top Si SOI layer via selective epitaxy of silicon on the source/drain regions of the device, as illustrated in Figure 1.5. This standard IC processing step consists first of an initial 950C, 2min *in-situ* hydrogen pre-bake in a silicon epitaxy vacuum system (known as the "Shiraki clean") to remove the thin native SiO_2 layer that inevitably forms when Si is exposed to air and to remove residual C, O, and F contamination typically introduced during previous processing and cleaning steps. This pre-bake step is immediately followed by selective epitaxy of silicon on the source/drain regions by pyrolysis of dichlorosilane (SiH_2Cl_2) on the silicon surface at a temperature of ~800C to allow for an acceptable growth rate.

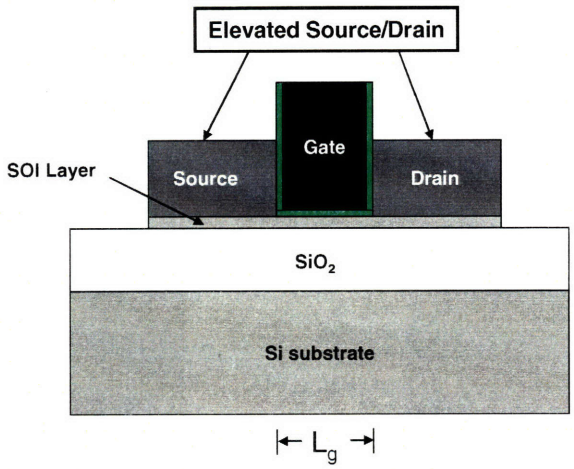

Figure 1.5: Schematic diagram of a fully-depleted SOI MOSFET showing the elevated source/drain structures required to reduce device series resistance to tolerable levels.

It is the high temperature pre-bake within the selective silicon epitaxy step, during which the ultra-thin SOI film is exposed to high temperature without the presence of any stabilizing capping film, that has been found to result most readily in SOI dewetting. Figure 1.6(a) shows a scanning electron micrograph of an 8nm-thick top Si SOI mesa after exposure to the standard 950C, 2min hydrogen pre-bake in a selective silicon epitaxy vacuum system.[11] The top Si film can clearly be seen to have fully dewetted upon the underlying SiO_2 layer under this standard pre-bake condition. Figure 1.6(b) shows that even pre-bake temperatures as low as 800C result in significant SOI layer edge retraction, making further device processing difficult, if not impossible.[11]

It is clear that SOI dewetting during the elevated source/drain pre-bake of standard MOSFET selective silicon epitaxy process step will only become an even more severe process limitation as the industry moves to the ~6nm, ~4nm, and ~3nm SOI layer thicknesses required to deploy fully-depleted SOI transistors at the 45nm, 35nm, and 22nm nodes, respectively, over the next 3 to 10 years. A deeper understanding of the SOI dewetting phenomenon will be required to develop novel techniques to stabilize ultra-thin

SOI layers against dewetting during high temperature vacuum processing to enable the successful deployment of fully-depleted SOI MOSFET's.

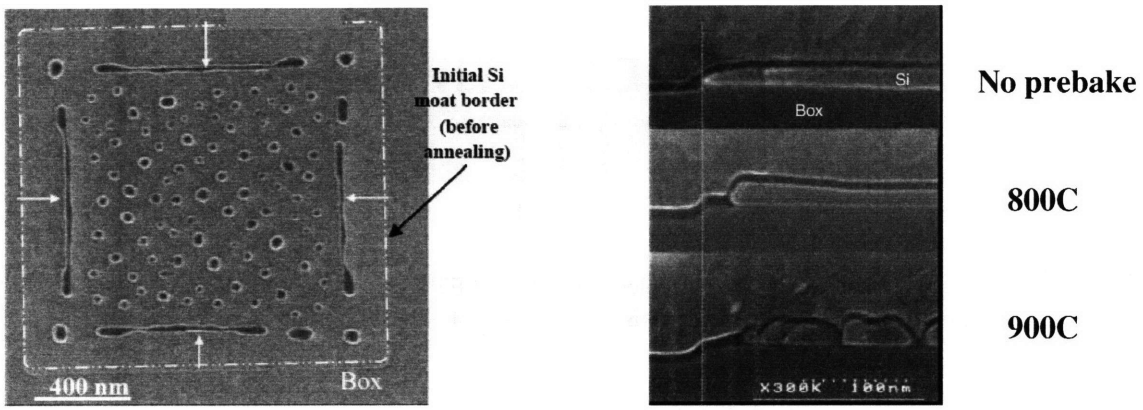

Figure 1.6: SEM micrographs of SOI dewetting occurring during the 20 torr H_2 Si selective epitaxy pre-bake step on a patterned 8nm-thick SOI film. a.) Plan view of an 8nm-thick SOI mesa after the standard 950C, 2 min H_2 pre-bake. B.) Cross-sectional view of the edge of an 8nm-thick SOI mesa: before pre-bake (top) and after 2 minute hydrogen pre-bakes at 800C (middle) and 900C (bottom). Note the edge retraction in the case of 800C and the complete dewetting that occurs at 900C.[11]

The Nanoscale Self-Assembly Opportunity

In contrast to representing a major process problem for the development of the next generation of MOSFET devices, anisotropic dewetting may also represent a promising new opportunity for "bottom up" self-assembly of highly ordered, monodisperse nanostructures. The extremely small size and large numbers typically associated with any assembly of nanoparticles precludes the use of deliberate externally controlled serial processes to fabricate practical nanostructures. Therefore, scientists have turned to the concept of self-assembly, in which nanoparticles naturally assemble into extensive ordered structures without direct ongoing external intervention given appropriate pre-conditions. A number of rudimentary self-assembling chemical and physical processes are currently being investigated, from the chemistry of solution-based

compound semiconductor nanocrystal fabrication[14] and self-assembled molecular monolayers on crystalline surfaces[15-17], to the physical processes of solid-state nucleation and growth of silicon nanocrystals[18] and dewetting of polycrystalline ultra-thin metal films.[19]

The self-assembling (or perhaps more aptly the "self-disassembling") process of surface-energy-driven dewetting in ultra-thin films is currently used to fabricate arrays of nanoscale metal catalyst islands to enable carbon nanotube and semiconductor nanowire growth and nanocrystal-based non-volatile memory applications.[20-25] However, the lack of order and poor size uniformity of the nanoisland arrays formed via uncontrolled dewetting from polycrystalline, highly defected deposited films[22,23,26], as illustrated in Figure 1.7, currently limits the use of nanoparticles, nanotubes, and nanowires in novel nanodevices with new functionalities.

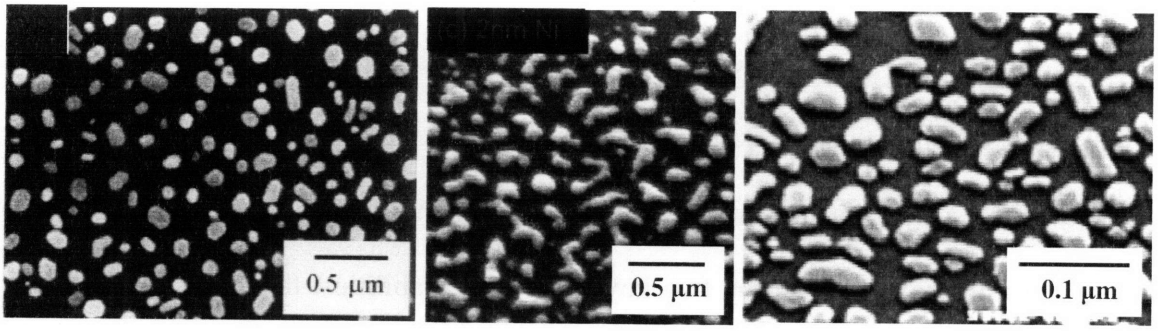

Figure 1.7: SEM micrographs illustrating the lack of order and size uniformity in island arrays formed via dewetting of deposited polycrystalline thin films: a.) 5nm sputtered Au film on SiO_2 annealed at 700C, 15min in H_2,[26] b.) 2nm sputtered Ni film on SiO_2 annealed at 750C, 15min in H_2,[22] and c.) 1.2nm sputtered Pt film on SiO_2 annealed at 700C, 60s in Ar.[23]

The single-crystal nature, crystalline symmetry, and anisotropic surface energies in SOI films provide ordering forces that hold promise for the fabrication of much more

ordered, uniformly sized nanoisland arrays via dewetting than has been achieved to date in deposited highly defective polycrystalline thin films. A comparison of the highly ordered uniform array of Si islands formed via SOI dewetting shown in Figure 1.6(a) relative to what is seen in Figure 1.7, highlights this opportunity.

Organization of Thesis

In Chapter 2 of this thesis, we present a review of the relevant previous theoretical and experimental literature on solid state thin-film dewetting, with an emphasis on the work that has elucidated the kinetic mechanisms of dewetting.

In Chapter 3, we present a review of the existing literature on SOI dewetting, summarizing key experimental observations, experimental shortcomings, and the currently dominant perspective in the literature that SOI dewetting is a stress-driven morphological evolution phenomenon.

In Chapter 4, we present an isotropic surface-energy-driven theory of SOI dewetting which includes a description of both the thermodynamics of the phenomenon and a 5-step surface-energy-driven kinetic dewetting mechanism based upon critical void formation and void growth via two key capillary instabilities: the generalized Rayleigh instability and the capillary film edge instability. We use this model to argue against the dominant perspective in the SOI dewetting literature that SOI dewetting is a stress-driven phenomenon. We also show that this model is able to account for the key experimental observations from the literature on SOI dewetting.

In Chapter 5, we present the experimental details of our SOI dewetting study, including a quantitative UHV annealing study of dewetting in 5.0-50.0nm patterned SOI

mesas having various in-plane edge orientations, an SOI defect study, and a proof-of-concept of the dielectric edge coverage stabilization technique for stabilizing SOI films against dewetting.

In Chapter 6, we present the experimental results and interpretation of the results of our UHV annealing study in ultra-thin SOI films, including quantitative measurements of the initial edge retraction dewetting process and the propagation rate of dewetting propagation by void finger formation and growth. In this chapter, we also extend our isotropic dewetting model to account for the effects of anisotropic surface energy where necessary to interpret our experimental results.

In Chapter 7, we discuss promising avenues for future work on SOI dewetting.

In Chapter 8, we summarize this thesis work and provide closing thoughts.

In Appendix A, we briefly discuss the key anisotropic surface energy properties of Si.

In Appendix B, we present and discuss experimental results on the effect of the presence of a Ge layer on the SOI surface on SOI dewetting.

Chapter 2:
Literature Review – Dewetting in Thin Solid Films

In this chapter, we review the existing literature on dewetting in thin solid films. We review the theoretical literature, with a focus on the thermodynamics of surface-energy-driven dewetting and the dominant kinetic dewetting mechanisms that have been proposed in the literature, with a focus on critical void formation, initial dewetting by critical void edge thickening and retraction, and continued dewetting by thickened edge breakdown and void finger formation and propagation. We then review the existing experimental dewetting literature in the context of these proposed kinetic mechanisms. The literature has identified these mechanisms as separate and incompatible. However, we propose that they are consistent with one another, simply representing different stages of a single dewetting process.

I. Theory Review – Solid-State Thin Film Dewetting

A. Thermodynamics of Dewetting

It has long been known that systems tend to evolve toward energy states that lower their total surface energy. It is this thermodynamic driving force that drives a number of well-known materials phenomena including sintering,[27] Ostwald ripening,[28] and thin film dewetting, amongst many others.

Depending on the relative interfacial energies of a thin film materials system (assuming isotropic surface energies, no film stress, and a rigid substrate), the equilibrium state of the system is either a flat film or a single hemispherical island

characterized by the contact angle its edge makes with the substrate, as shown in Figure 2.1. Young derived from a horizontal surface tension balance at the film edge that this equilibrium contact angle is given by

$$\Theta_c = \cos^{-1}\left[\frac{\gamma_{sv} - \gamma_{fs}}{\gamma_{fv}}\right], \tag{2.1}$$

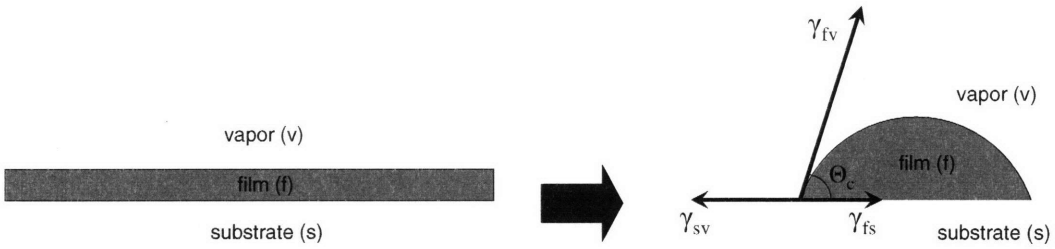

Figure 2.1: Schematic illustration of the equilibrium shape of a thin film, assuming isotropic surface energies and a rigid substrate, as determined first by Young.[29]

where γ_{sv} is the substrate-vapor surface energy density, γ_{fv} is the film-vapor surface energy density, and γ_{fs} is the film-substrate surface energy density.[29] If $\gamma_{sv} \geq \gamma_{fv} + \gamma_{fs}$, then the equilibrium contact angle is zero and the equilibrium state is a flat film. Otherwise, the equilibrium contact angle is finite and the equilibrium state of the film is one single hemispherical island making this equilibrium angle with the substrate. (In this work, any thin film system with a non-zero equilibrium wetting angle is considered to be a "dewetting system".) In general, the magnitude of the equilibrium contact angle represents the driving force for a thin film to dewet, with thin film systems with larger contact angles having a larger driving force to dewet. The equilibrium contact angle also figures prominently in all isotropic dewetting analyses, as will be shown in Chapter 4.

Although the thermodynamic equilibrium state of any dewetting system is given by one single island on a substrate, a range of states consisting of arrays of identical smaller islands each making the equilibrium contact angle with the substrate are also stable relative to a flat-film. Srolovitz and Goldiner showed that for a given film thickness, h_f, there exists a minimum island radius such that a final state consisting of an array of islands of that radius is more stable than the flat film.[30] The minimum island radius for which such an islanded state is stable relative to the flat film is given by

$$r_{\min} = \frac{3\sin\Theta_c}{1-\cos\Theta_c} h_f . \tag{2.2}$$

Thus, in a dewetting system, a range of islanded film geometries are more stable than a flat film, from a marginally more stable array of islands having radii just greater than $r_{\min}$ to a single island representing the most stable final state.

B. Kinetics of Dewetting

Although thermodynamics dictates the range of final islanded states to which a dewetting flat film can evolve, it is the specific kinetic mechanism by which a thin film dewets that determines the islanded state to which the system will actually evolve. Here, we describe the key existing literature describing the theory behind the kinetics of dewetting.

Gibbs derived the expression for the excess free energy per atom at a surface (known as the Gibbs-Thompson equation),[31] leading to the following expressions for the surface chemical potential, $\mu(s)$, and surface-energy-driven atomic surface diffusion flux J_s, respectively, below:

$$\mu(s) = \mu^{\circ} + \Omega\gamma\kappa(s) \tag{2.3}$$

$$J_s = -\frac{D_s}{\Omega kT}\nabla\mu(s) = -\frac{D_s\gamma}{kT}\nabla\kappa(s) \tag{2.4}$$

where μ° is the chemical potential at a flat surface, Ω is the atomic volume, γ is the surface free energy density, D_s is the surface diffusivity, k is Boltzmann's constant, T is the absolute temperature, and $\kappa(s)$ is the mean surface curvature at the surface coordinate s. In this convention, the curvature of a convex surface is considered positive, while that of a concave surface is considered negative. Thus, convex surface regions have higher chemical potential and concave regions have lower chemical potential, driving a surface-energy-driven atomic flux from surface "hills" to "valleys".

i.) Critical Void Formation

Mullins applied the divergence theorem to Equation 2.4 to derive an expression for the velocity of the surface normal, $V_n(s)$, during surface-energy-driven morphological evolution via surface diffusion to be

$$V_n(s) = -\frac{D_s\gamma\Omega^2\nu}{kT}\nabla^2\kappa(s) = -B\nabla^2\kappa(s), \tag{2.5}$$

where ν is the atomic surface density and all other parameters are as previously defined.[32] The prefactor in this equation is a common materials constant found in dewetting theory and will be often be referred to by the constant B going forward. (Note: Due to the fact that curvature represents a second derivative, this equation is a fourth order partial differential equation). Mullins solved Equation 2.5 in the small slope limit to demonstrate theoretically that initially flat films in dewetting systems are metastable against dewetting.[33] He showed that any non-through-thickness surface morphology perturbation of an initially flat film would spontaneously decay back to a flat film and thus that the

pre-existence or formation of substrate-exposing voids is required for a thin film to spontaneously dewet.[33] (This makes physical sense in that any non-through-thickness surface perturbation from a flat film introduces additional surface area and surface energy without destroying any.) Srolovitz and Safran determined further on pure thermodynamic grounds that not only must a substrate-exposing film void exist for dewetting to spontaneously proceed, but that such a void must also be greater than a critical size for subsequent continuous void growth and dewetting to be energetically favored.[30] For a truncated conical film void making the equilibrium contact angle with the substrate, their results predict a critical void radius of

$$r_{crit} = \frac{h_f}{\sin\Theta_c}. \tag{2.6}$$

Under this model, subcritical substrate-exposing film voids with $r < r_{crit}$ will spontaneously fill in, restoring the flat film; whereas supercritical voids with $r > r_{crit}$ will spontaneously grow.

Srolovitz and Safran provided further theoretical credence for this critical void phenomenon in another paper by numerically solving for the kinetic morphological evolution of the same truncated conical film void described above in a dewetting film in the small slope limit (an approximation).[34] They found a critical void radius value to exist between $2\frac{h_f}{\tan\Theta_c} - 3\frac{h_f}{\tan\Theta_c}$, below which their simulations showed the void to fill in and restore the flat film and above which they showed spontaneous hole growth by continuous edge thickening and retraction.

ii.) Initial Void Growth via Void Edge Retraction and Thickening

Two authors have proposed kinetic models for how dewetting proceeds once a supercritical thin film void is made present in a thin film dewetting system. Brandon and Bradshaw proposed a simple analytical model for dewetting void growth by continuous edge thickening and retraction.[35] In this model, they assumed a *circular* film void geometry and that all of the mass originally contained within the void region builds up in an edge region with a semicircular cross-section making a 90° equilibrium contact angle at the retracting void edge, as shown in Figure 2.2.

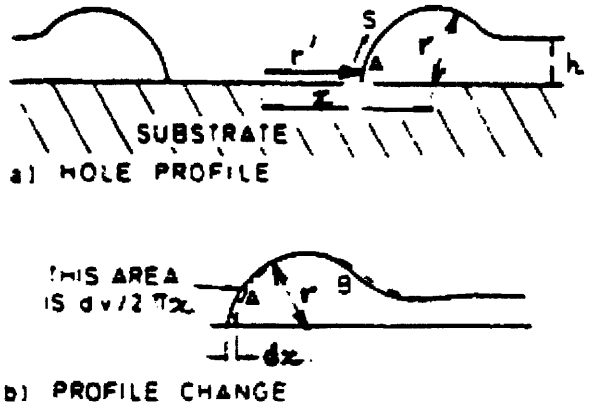

Figure 2.2: Schematic illustration of the analytical model for dewetting void growth via edge thickening and retraction initially posed by Brandon and Bradshaw.[35]

We use a derivation for void growth via edge thickening and retraction at a *straight* film edge, as opposed to a *circular* film void edge, similar to that of Brandon and Bradshaw in developing our own dewetting theory in Chapter 4, so we forego the derivation here and just share the result. Using this model, Brandon and Bradshaw derived an expression for the void radius versus time, defined as the distance between the center of the void and the edge of the thickening void front, given by

$$r_{void} = \left(\frac{25\pi}{4}\right)^{\frac{1}{5}} B^{2/5} \frac{t^{\frac{2}{5}}}{h_f^{\frac{3}{5}}}, \tag{2.7}$$

where t denotes time and all other parameters are as previously defined,[35] thus predicting a void growth velocity, v_{void}, with the following key dependencies

$$v_{void} \propto \frac{B^{\frac{2}{5}}}{h_f^{\frac{3}{5}}} \frac{1}{t^{\frac{3}{5}}}. \tag{2.8}$$

where t is the annealing time and all other parameters are as previously defined.

It can clearly be seen from this expression that this model predicts that the retracting film void edge motion continuously slows down with time as the edge becomes thicker and the curvature gradient at the edge continuously decreases. Thus, this model predicts that dewetting at a supercritical film void should be observed to slow and ultimately stop with sufficient annealing time.

The only other theoretical treatment of initial void growth via edge curvature driven edge thickening and retraction was performed by Srolovitz and Safran.[34] They used the same numerical technique discussed above to attempt to model the kinetics of supercritical void growth via edge thickening and retraction. Their modeling predicts a rather complex dependency for the void growth velocity, valid for large void sizes and times, of

$$v_{void} \propto \frac{B^{\frac{1}{4}}}{t^{\frac{3}{4}}} \ln^3\left(Bt\left(\frac{\tan\Theta_c}{h_f}\right)^4\right). \tag{2.9}$$

The physical meaning of this result is not immediately transparent.

Perhaps the most interesting result from this work by Srolovitz and Safran was the observation in their simulation that a trough of ever increasing depth formed ahead of the thickening dewetting void edge, as shown in Figure 2.3. They hypothesized that the growth of a trough such as this in a real dewetting film could proceed until it reached the substrate, allowing for the creation of a new void edge with a high edge curvature and that the iterative process of void edge thickening and new void edge creation by leading trough growth could allow for an apparent constant dewetting propagation rate over time scales longer than a few pinch off cycles. In contrast with the mechanism proposed by Brandon and Bradshaw, such a mechanism would allow for continued dewetting of a thin film with time with an apparent constant velocity over sufficiently long times.

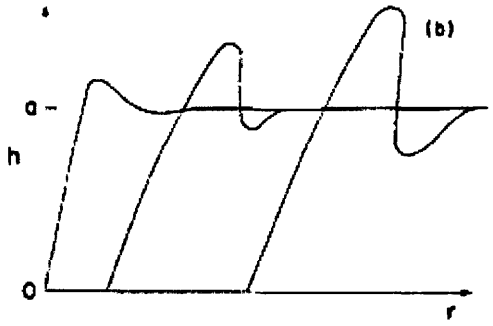

Figure 2.3: Schematic illustration of trough formation observed in front of a dewetting thickening void edge from the numerical kinetic simulation of Srolovitz and Safran.[34]

iii.) Continued Dewetting via Thickened Void Edge Breakdown and Void Finger Formation and Propagation

The most important recent breakthrough in the theory of thin film dewetting was made when Jiran and Thompson posed a new thin film dewetting mechanism by considering the instability of a uniform thickening retracting dewetting void edge to

breakdown along its length.[36,37] (We discuss and extend the Jiran-Thompson in the context of our own theory for SOI dewetting in Chapter 4, so we only briefly describe the model here.) Jiran and Thompson proposed that dewetting occurs via an initial continuously slowing void edge thickening and retraction mechanism, as described by Brandon and Bradshaw,[35] followed by thickened void edge breakdown via a generalized Rayleigh instability. Under their model, illustrated schematically in Figure 2.4, this edge breakdown results in the formation of periodic, locally-thin film edge regions with access to a very small local edge thickness (and high local edge curvature) given by the film thickness. Under their model, mass flows continuously away from these local thin void edge regions to neighboring thicker regions, causing void fingers to penetrate the slow moving thickened void edge and grow into the neighboring thin film region at a constant, relatively fast velocity dictated only by the initial film thickness. Under their model, the fingers of film material left between the growing void fingers then break up via a further Rayleigh instability to form islands.[36]

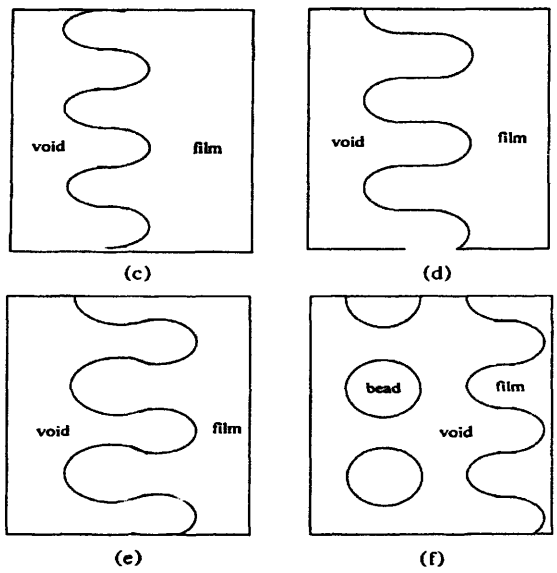

Figure 2.4: Schematic illustration of the thickened edge breakdown/void finger formation and propagation model of Jiran and Thompson.[36]

Assuming that these void finger tips maintain a thickness equal to the film thickness and that mass flows quickly away from these tips, their model predicts that these void fingers should grow at a constant velocity given by[36]

$$v_{finger} = \frac{2}{\pi}\frac{D_s \gamma \Omega^2 \nu}{kT}\frac{1}{h_f^3} = \frac{2}{\pi}\frac{B}{h_f^3}. \qquad (2.10)$$

II. Experimental Review – Solid-State Thin Film Dewetting

Due to the practical significance of dewetting of thin film systems for nanotube and nanowire growth, nanocrystal-based non-volatile memory applications, and semiconductor device layer stability, a large body of literature exists on thin film dewetting. These studies have focused primarily on metal-on-insulator systems such as Cu, Au, Ni, Pt, Sn, Pb, and Co on dielectric substrates such as SiO_2, pyrex, and mica[22-26,36-60]. Nearly all of this literature has focused on the determination of the critical temperature at which dewetting occurs and on the geometrical nature of the island array that results from dewetting, as these are the most important parameters from a purely technological standpoint. This literature focuses only on the state of the film after complete dewetting, and thus gives little to no direct information about the physical mechanism by which dewetting occurs. The most important results from this literature are that 1.) thinner films tend dewet at lower temperatures and times than thicker films and 2.) thinner films tend to form smaller islands.

A small subset of this experimental dewetting literature has focused on revealing the basic physical mechanisms behind dewetting and quantitative measurements of dewetting kinetics and is discussed in detail below.

A. Dewetting via Void Growth by Edge Thickening and Retraction

A few authors have observed a physical dewetting mechanism in which film voids form in initially continuous films and grow via edge thickening and retraction until the voids impinge, creating an array of film ridges, which subsequently break up into islands.[35,39-47,61] Sieradzki et al. studied dewetting in evaporated Ag films on SiO_2 layers under vacuum annealing conditions.[47] As shown in Figure 2.5, illustrating the early stages of Ag film dewetting, they clearly observed the void growth via edge thickening and retraction dewetting mechanism in a 100nm thick polycrystalline evaporated Ag film annealed at 635C for various times. Kwon et al. studied dewetting in polycrystalline sputtered Cu films on SiO_2 layers annealed in a hydrogen ambient. As shown in Figure 2.6, they also clearly observed dewetting to occur via a void edge thickening and retraction mechanism followed by void edge impingement to form isolated Cu islands.[26]

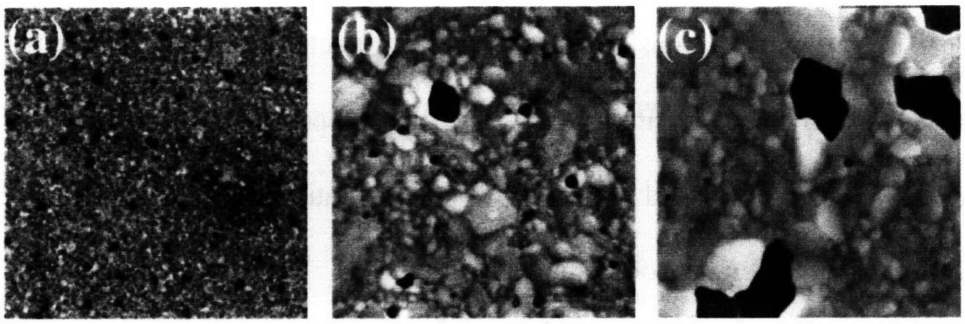

Figure 2.5: SEM micrographs showing the early stage time evolution of dewetting in a polycrystalline evaporated 100nm Ag-on-SiO2 film vacuum annealed at 635C: a.) as deposited, b.) 1 min anneal, and c.) 5 min anneal. (Image size 10x10 μm). Film void growth via edge thickening and retraction is evident.[47]

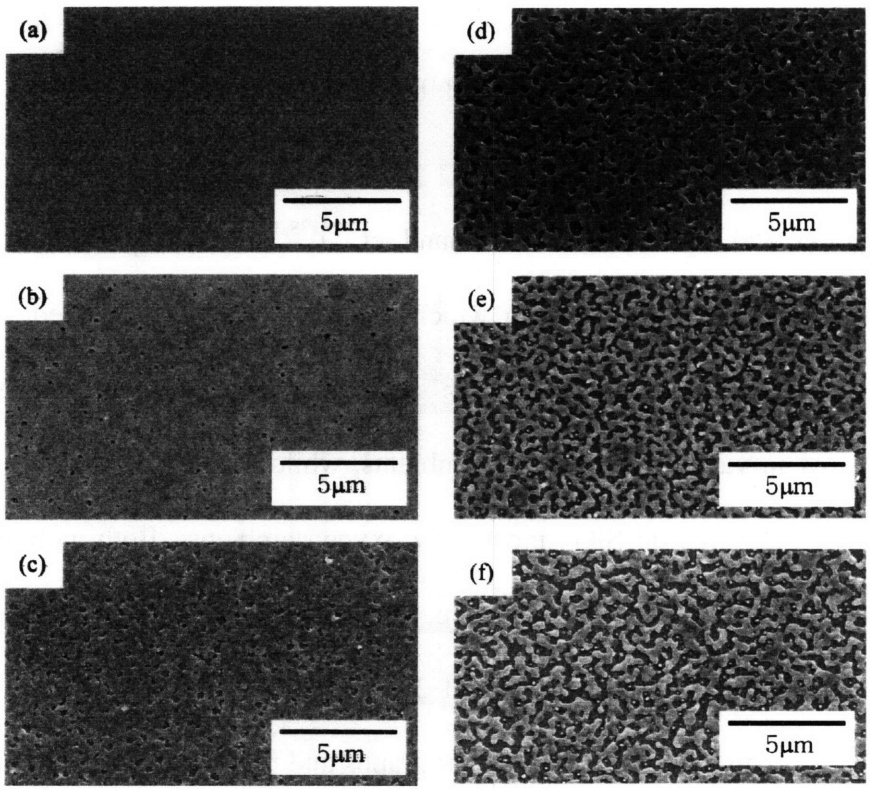

Figure 2.6: SEM images illustrating the dewetting process in a 50nm Cu film on SiO_2 annealed at 300C for various times under a hydrogen ambient at 635C: a.) as deposited, b.) 10min, c.) 20min, d.) 40min, e.) 60min, and f.) 120min. The dewetting mechanism of void growth via edge thickening and retraction and void impingement is evident.[26]

Brandon and Bradshaw,[35] Sharma and Spitz,[40-45] and Presland et al.[38,39,61] are the only authors who have reported quantitative kinetic studies of film dewetting by void growth via uniform edge thickening and retraction.

Brandon and Bradshaw, who developed the model for void growth via uniform edge thickening and retraction described above, studied dewetting in 100-270nm evaporated Au films on mica annealed in air. As shown in Figure 2.7, they observed dewetting via the void edge thickening and retraction mechanism. Using optical microscopy, they measured the radius, r_{void}, of individual film voids after subsequent

anneals and found that plots of $(r_{void-final}^{\frac{5}{2}} - r_{void-initial}^{\frac{5}{2}})$ vs annealing time for individual voids had reasonably good linear fits, agreeing with the 2/5 power law dependence of the void growth radius with time predicted by Brandon and Bradshaw's void growth model.[35]

Sharma and Spitz[40-45] and Presland et al.[38,39,61] each performed quantitative studies of dewetting of Ag films in which they measured the exposed substrate area versus annealing time. Sharma and Spitz studied dewetting in 50-200nm sputtered Ag films on Pyrex in vacuum and oxygen ambients, while Presland et al. studied dewetting of evaporated Ag films on SiO_2 under only oxygen ambients. Both authors observed a void growth by edge thickening, retraction, and impingement dewetting mechanism very similar to that shown in Figures 2.5 and 2.6. Both authors also extracted the exposed substrate area versus time from SEM micrographs and found that plots of exposed area to the 5/4 power versus time for a given Ag thickness, temperature, and ambient yielded excellent linear fits for sufficiently short annealing times that film voids had not yet begun to overlap.[38-45,61] The growth of a collection of identically sized voids via the Brandon and Bradshaw mechanism would be expected to result in an exposed substrate area proportional to the square of the predicted value of r_{void} given in Equation 2.7, yielding a 4/5 power law dependence with time. This is not strictly correct, however, for a set of growing voids having a range of radius values, as was the case in the experiments of Sharma and Spitz and Presland et al. However, the general observation of a 4/5 power law time dependence of the exposed area in their experiments yields further support for the validity of the Brandon and Bradshaw model for dewetting by void growth via edge thickening and retraction.

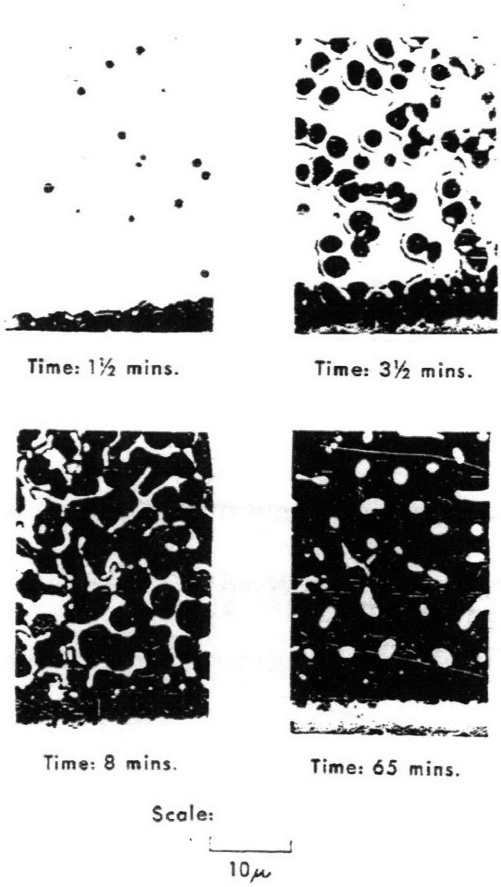

Figure 2.7: Optical micrographs showing the evolution of an evaporated 110nm Ag film on mica annealed in air for various times sequentially. The dewetting of the film by void growth via edge thickening and retraction is evident. Brandon and Bradshaw quantified the void growth rate by tracking the radii of individual voids with time to confirm the time dependency of their void growth model.[35]

B. Dewetting via Void Edge Breakdown and Void Finger Formation and Propagation

Two authors have observed a very different dewetting mechanism from the void growth by void edge thickening, retraction, and impingement mechanism described in the previous section. Kwon et al.[26] and Jiran and Thompson[36,37] both observed a dewetting mechanism in which the edge of growing dewetting film voids break down and continued dewetting occurs by the formation and growth of void fingers that penetrate into the film, leaving behind fingers of film material that subsequently break down into islands, as

shown in Figures 2.8 and 2.9. Interestingly, as shown in Figures 2.6 and 2.8, Kwon et al. observed this void edge breakdown and void finger formation and propagation dewetting mechanism in annealed 50nm Au films on SiO_2, while observing the void growth by uniform edge thickening and impingement mechanism in annealed 50nm Cu films on SiO_2. Comparing the two figures, it is clear that the density of void formation is much higher in the case of Cu. We conclude that the void growth via uniform edge thickening and retraction mechanism and the void edge breakdown and finger formation mechanism are both fundamental to dewetting in thin films and occur in sequence when void edge breakdown and finger formation is observed. For the results of Kwon et al., the voids in their Cu films were simply so close together that they impinged via void growth before they had the opportunity to break down and form void fingers. In the case of the Au films they studied, the void density was sufficiently low to allow for uniform void growth via uniform edge thickening and retraction to the point of edge breakdown and void finger formation and propagation.

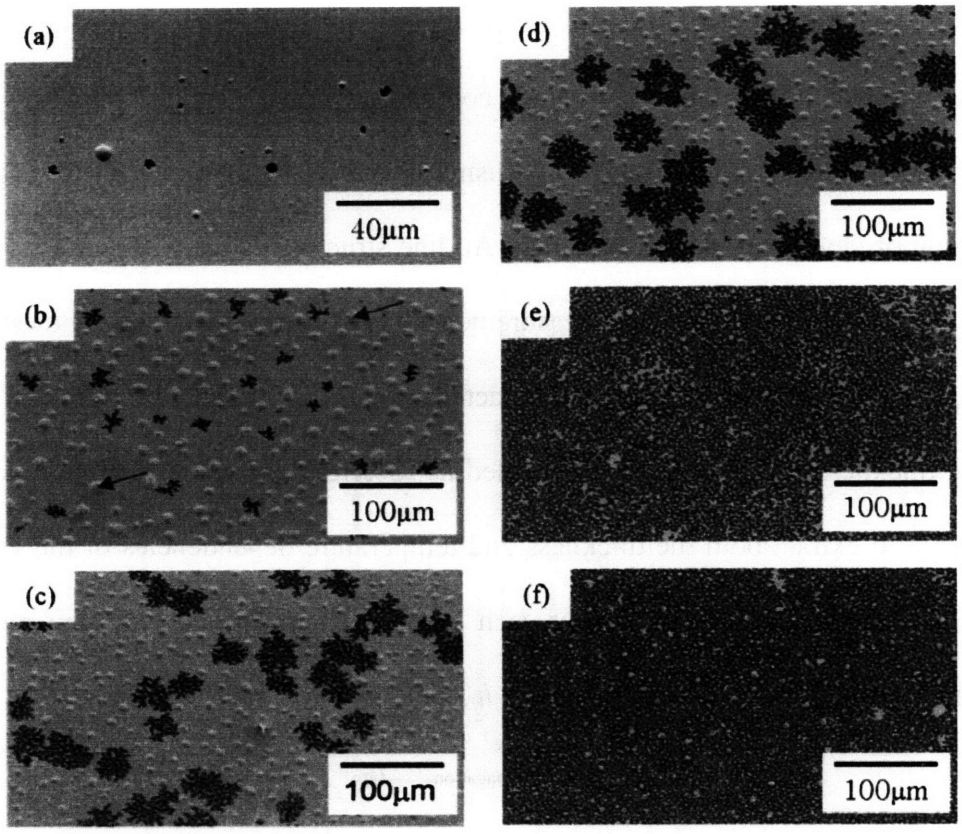

Figure 2.8: SEM images of 50nm Au films on SiO_2 annealed in H_2 at 700C for various times. a.) 5min, b.) 30min, c.) 60min, d.) 90min, e.) 120min, and f.) 150min. The thickened void edge breakdown and void finger formation and propagation mechanism is clearly seen to be active in this case.[26]

Jiran and Thompson also observed the thickened void edge breakdown and void finger formation and propagation dewetting mechanism in Au films on SiO_2, as illustrated in Figure 2.9.[36] However, in addition to observing this dewetting mechanism, they also quantified the kinetics of the void finger growth dewetting mechanism in evaporated Au films on SiO_2 using a very clever technique based upon *in-situ* laser transmission intensity through the dewetting film during annealing. Using a laser wavelength at which SiO_2 is transparent and Au is opaque, they were able to measure the exposed substrate area *in-situ* during annealing by measuring the transmitted laser light intensity. Furthermore, they performed their measurements on patterned Au lines in order

to study the kinetics of void growth alone, as opposed to the convolution of void nucleation and void growth that occurs in continuous films.

Figure 2.9 contains a series of transmission optical micrographs showing the time evolution of dewetting in their patterned Au line structures during annealing. From their *in-situ* transmitted light intensity measurements, they observed a constant dewetting front propagation velocity with time and extracted propagation velocity values for Au films having thicknesses from 40-90nm annealed at 700, 750, and 800C. From this data, they were able to extract both the thickness and temperature dependencies of the void finger propagation process. They found for each annealing temperature that their propagation velocity, $v_{propagation}$, versus film thickness, h_f, yielded good power law fits

$$v_{propagation} \propto h_f^{-n} \tag{2.11}$$

with n values of 3.4, 2.4, and 2.1 for 700C, 750C, and 800C, respectively. The consistency of this result with the n=3 power law dependency predicted by their void finger propagation model, expressed in Equation 2.10, supported the validity of their model.

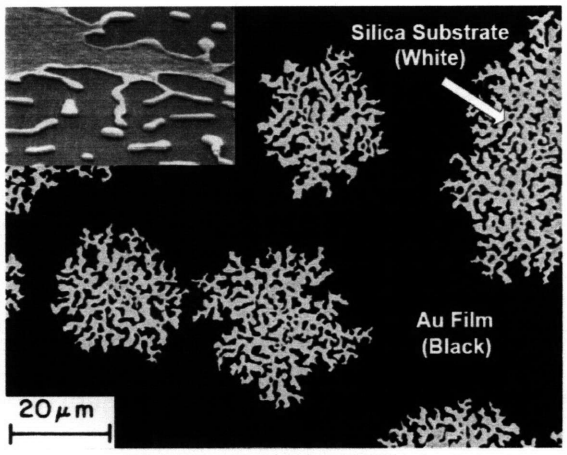

Figure 2.9: Optical transmission micrograph and SEM micrograph (inset) showing dewetting in a Au film on SiO_2 via the thickened void edge breakdown and void finger formation and propagation mechanism, as observed by Jiran and Thompson.[36]

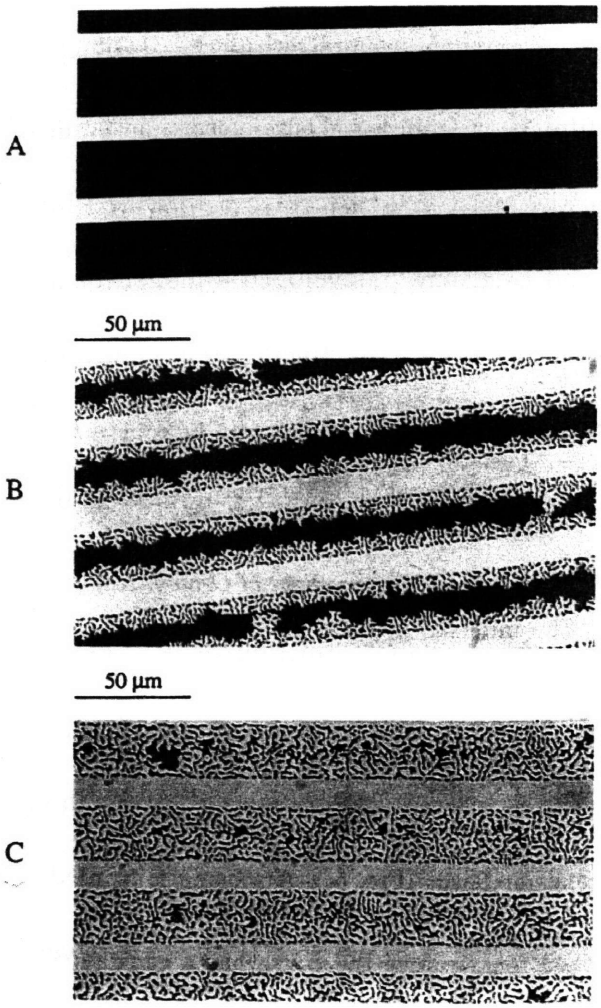

Figure 2.10: Optical transmission micrographs from Jiran and Thompson showing the dewetting evolution of patterned Au lines on SiO_2 during annealing : a.) before annealing, b.) partially dewetted, and c.) fully dewetted. The study of patterned Au lines allowed Jiran and Thompson to specifically study the kinetics of void finger propagation in isolation, as the edges of patterned structures represent pre-existing unstable critical voids.[36]

Summary

In this chapter, we presented a review of the theoretical and experimental literature on dewetting of solid-state thin films. In terms of thermodynamics, we presented Young's analysis of the thermodynamically stable state of a thin film system

based upon the calculation of the equilibrium contact angle, with film systems having finite equilibrium contact angles being thermodynamically unstable to island formation.[29] The work of Mullins[33] and Srolovitz and Safran[34,62] established that in a dewetting thin film system a flat film is indeed metastable and that a substrate-exposing film void greater than a critical size must first be formed before the film can undergo spontaneous dewetting. Brandon and Bradshaw[35] developed a model for dewetting at a circular void via uniform void edge thickening and retraction that predicts a growing void radius that depends on the 3/5 power of time and on the -3/5 power of the film thickness, indicating that void growth by this mechanism should continuously slow and ultimately stop. From the results of numerical simulations of void growth via edge thickening and retraction, Srolovitz and Safran[34] observed the formation of a continuously deepening trough in front of a thickening retracting void edge and proposed that an iterative mechanism in which such troughs reach the substrate to create a new high curvature void edge. They proposed that this mechanism could allow for continued dewetting at a slowing thickening retracting void edge. Jiran and Thompson developed a model by which dewetting proceeds by an initial uniform edge thickening and retracting step, but in which the thickened edge then breaks down by a Rayleigh instability allowing void fingers to form and penetrate at a constant rate into the flat film, resulting in a constant dewetting propagation front velocity and continuous film dewetting. Their model predicts a dewetting propagation velocity proportional to the -3 power of the film thickness.

In terms of experimental work quantifying the kinetics of dewetting, Brandon and Bradshaw, Sharma and Spitz, and Presland et al. have confirmed the 2/5 power law dependence of the void radius on time during the initial edge thickening and retraction

dewetting step by measuring the exposed substrate area versus time, while Jiran and Thompson experimentally confirmed a -3 power law dependence of the dewetting propagation rate during the phase of void finger growth after thickened void edge breakdown. Although the literature has identified these two processes as being incompatible and representing fundamentally different dewetting behaviors, we identify them as simply being two successive steps in the dewetting process, with the void edge thickening and retraction process always preceding void edge breakdown via void finger formation and propagation.

Chapter 3:
Literature Review –
Dewetting in Silicon-on-Insulator Films

There is a significant body of previous literature on the dewetting of single-crystal ultra-thin SOI films which has revealed a number of important experimental dependencies of this phenomenon. (For reference, what is referred to as "dewetting" here is frequently termed "agglomeration" in this literature). However, the current experimental literature has a number of limitations in terms of providing an understanding of the basic kinetics behind SOI dewetting and the development of an accurate mechanistic model. We review the existing literature and highlight these limitations here.

Ono et. al were the first to observe SOI dewetting in (100) and (111)-oriented SOI films. They performed a series 5s resistive anneals in UHV (~10^{-9} torr) on SIMOX SOI samples having a top Si thickness range of 15-200nm and over a temperature range of 950-1200C. For films with thickness < 50nm, upon sufficiently high temperature annealing < 1200C, dewetting film voids with thickened edges were observed to form locally in initially continuous films in both (100) and (111)-oriented top Si layers, as shown in Figure 3.1. In both the (111) and (100)-oriented samples, the voids grew by piling material up at the thickening retracting void edge until growing voids impinged on each other, exhibiting the previously mentioned void growth via edge thickening, retraction, and impingement dewetting mechanism, as shown in Figure 3.2. We believe that this is due to the high density of dewetting initiation observed in these films, which

precluded the observation of edge breakdown and void finger formation and growth. Ono et al. observed that thicker SOI films were more stable against dewetting initiation, requiring higher 5s-annealing-temperatures for dewetting initiation to be observed, with films > 50nm thick found to be stable all the way up to 1200C. They also found that void formation occurred only at defected film locations where SiO_2 precipitates pushed some distance into the SOI film from the underlying SiO_2 layer, as can be seen clearly in Figures 3.1(b) and 3.1(c).

Perhaps the most striking behavior observed in this work is the clear and distinct anisotropic dewetting void shapes formed by dewetting in both the (111) and (100)-oriented SOI films, as shown in the AFM images in Figures 3.1 and 3.2. In the (111)-oriented SOI films, hexagonal voids with 3 fold symmetry (3 opposing long sides, 3 opposing short sides) having sides parallel to two distinct types of in-plane <110> directions were formed. ((111)-oriented Si has two inequivalent in-plane <110> directions). The two types of edges were defined as $<1\bar{1}2>$-type (long sides) and $<\bar{1}\,\bar{1}2>$-type (short sides), defined by their inward in-plane direction. As is discussed in Appendix A, the lowest energy stable facets of silicon normally are the (111), (311), (110), and (100) facets, with (111) or (311) typically found to be have the lowest surface energy.[63-65]

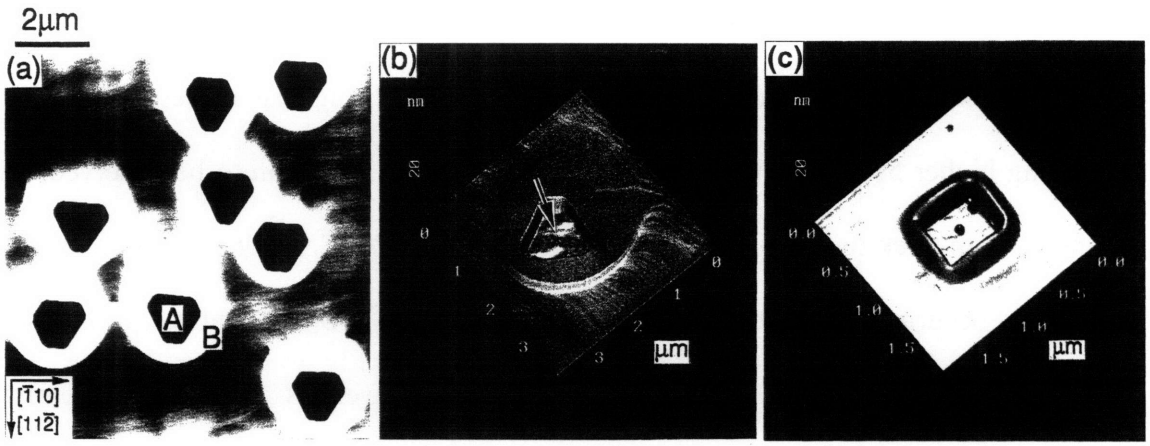

Figure 3.1: AFM images of dewetting in SIMOX SOI samples from the work of Ono et al. a.) and b.) show dewetting void growth via edge thickening and retraction in a (111)-oriented 16nm top Si film annealed at 1100C for 5s, while c.) shows the same behavior in a (100)-oriented 15nm top Si oriented film under the same annealing conditions. The clear anisotropic behavior is a result of the underlying anisotropy of the surface energy of Si.[1]

The dominant longer $<11\bar{2}>$-type inside void edges can facet on both a (110) and (111) plane, while the less prominent $<\bar{1}\,\bar{1}2>$-type edges can facet on two distinct (311) planes and a (100) plane. In the (100)-oriented SOI films, square voids were formed with sides parallel to in-plane <110> directions as well. The sidewalls of these edges could facet on both the (111) and (311) low energy planes. The observed void shapes can thus be understood in terms of their ability to preferentially expose the low energy planes in Si.

Nuryadi et al. were the first to perform a more systematic study of SOI dewetting. They were the first to clearly illuminate that SOI dewetting kinetics and the resultant Si island geometries are completely determined by the SOI top Si layer thickness and were the first to observe the thickened void edge breakdown and void finger formation and propagation dewetting mechanism in SOI. They performed a series of 10s UHV resistive

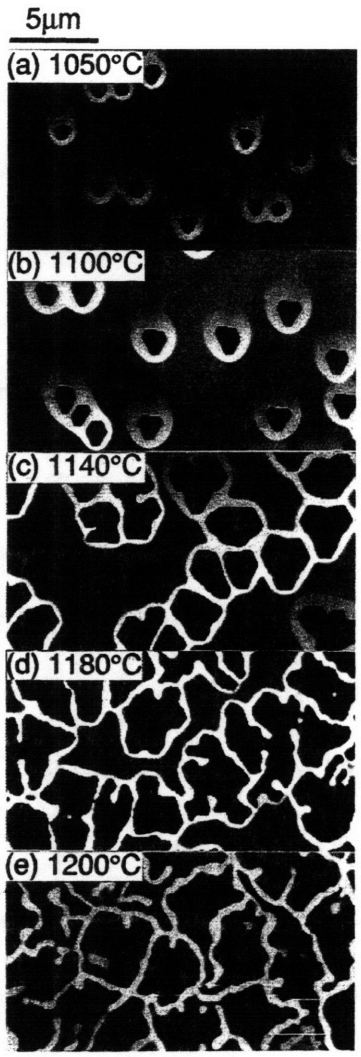

Figure 3.2: AFM images of dewetting in (111)-oriented 16nm top Si thickness SIMOX films after 5s annealing at various temperatures: a.) 1050C, b.) 1100C, c.)1140C, d.) 1180C, and e. 1200C. These images clearly show that the film is dewetting by void edge uniform thickening and retraction and void impingement mechanism.[1]

annealing experiments on (100)-oriented bonded SOI films over the thickness range 1-19nm to determine the SOI dewetting initiation temperature versus thickness for 10s anneals. They found that the 10s-dewetting-initiation-temperature in initially continuous film regions was determined by the SOI top silicon thickness and increased linearly from 825C-1250C with thickness for SOI thicknesses of 5-16nm. Furthermore, they studied dewetting initiation in SOI samples having different underlying SiO_2 layer thicknesses

and found that the SiO_2 thickness had no effect on dewetting behavior. Importantly, Nuryadi et al. performed an H_2SO_4/H_20_2 pre-anneal sample clean, but did not perform a final HF etch on their samples before introduction into the UHV annealing chamber, leaving a thin layer of a chemically grown capping SiO_2 layer on the top Si SOI layer. Thus, the process they observed during annealing represented a convolution of both Si native oxide thermal desorption and SOI dewetting initiation and growth, as opposed to the dewetting process alone.

Similar to what was observed by Ono et al., SOI voids were observed to first form and grow as square voids with thickening sidewalls parallel to in-plane <110> directions, as shown in Figure 3.3(a). Unlike in the work of Ono et al., however, these sidewalls were then observed to breakdown and be penetrated by equally spaced void fingers, which were observed to propagate only in the eight (100) in-plane <310> directions, as shown in Figure 3.3(a) as well. These void fingers formed in a star-like pattern having 4-fold symmetry. The outline of the growing dewetting region maintained an approximately square shape with sides parallel to the in-plane <110> directions, with the dewetting region forming as <310> in-plane-oriented void fingers and Si fingers propagated out into the neighboring flat film regions. These Si fingers were subsequently observed to break down into islands bounded by (311) side and (100) top facets.

The islands formed as a result of the SOI dewetting process were found to have a highly uniform size distribution. It was found that the average island height, lateral size, and spacing were proportional to the initial SOI thickness, as shown in Figure 3.3(b). Nuryadi et al. also confirmed that the Si film volume was conserved during SOI dewetting, clearly indicating that the phenomenon is not driven by an evaporation

process, but by a surface diffusion process. Importantly, Nuryadi et al proposed that SOI dewetting occurs via a stress-driven instability caused by high stresses in the Si film due to the thermal expansion mismatch between Si and SiO_2, akin to the Asaro-Tiller-Grinfel'd instability that has been observed in lattice mismatched heteroepitaxial films.[66-68] This has become the consensus theory in the SOI dewetting literature.

The work of Nuryadi et al. suffered from a few key limitations. One key limitation in this study was the fact that the phenomenon was studied only in initially flat continuous SOI films, so that a convolution of the kinetics of void nucleation and the dewetting kinetics of void growth was observed. Furthermore, annealing studies were performed on SiO_2-covered samples, and thus the annealing experiments also observed a convolution of SiO_2 desorption and SOI dewetting kinetics. Furthermore, only one annealing time was used and no kinetic parameters beyond an observed initiation temperature for one annealing time were extracted as well.

Legrand et al. also reported the results of a UHV resistive annealing dewetting study of (100)-oriented SOI films.[9,10] They studied bonded SOI films having top Si thicknesses ranging from 1-19nm and determined the dewetting initiation temperature in continuous films for a fixed 10min annealing time. Importantly, they were the first to definitively identify the stabilizing effect of a capping SiO_2 layer on an SOI film, proving clearly that the Si film surface must be uncovered for dewetting to proceed. Using Auger emission spectroscopy in tandem with ex-situ AFM analysis, they determined definitively that SOI dewetting did not occur until the capping SiO_2 layer was completely desorbed. With a thin SiO_2 capping layer, they found the 10 min-annealing dewetting initiation temperature to increase monotonically from 560C for a 1nm SOI film up to 875C for a

19nm SOI film. They found that when an HF dip was performed right before sample annealing, providing a SiO_2-free bare Si surface during annealing, that for 5.5nm SOI films, the dewetting initiation temperature decreased from 850C to 800C, proving that SOI annealing experiments performed with an SiO_2 layer present represent a convolution of SiO_2 desorption kinetics along with SOI dewetting kinetics, and thus do not give an accurate description of SOI dewetting kinetics alone. The shortcomings of this study for understanding the kinetics of SOI dewetting were the same as those mentioned with regard to the study of Nuryadi et al., the convolution of SOI void nucleation kinetics with growth kinetics and the convolution of oxide desorption and SOI dewetting kinetics in their results. Furthermore, similar to Nuryadi et al., Legrand et al. identified SOI dewetting as a stress-driven instability.

Ishikawa et al. (with Nuryadi) extended the work of Nuryadi et al. to study the relative stability of patterned SOI top Si layers compared to initially continuous layers.[5,6] Using the same annealing technique as Nuryadi et al., they explored the UHV annealing dewetting stability of 1μm square etched mesas in (100)-oriented 12nm-thick SOI layers, as well as of patterned 1μm wide Si lines in (100)-oriented 3nm and 6nm thick SOI layers, all with etched edges parallel to in-plane <110> directions. In both cases, they found that dewetting initiated first at SOI film mesa edges and propagated into the neighboring flat film regions to dewet the film. Not only was dewetting found to initiate first at the patterned mesa edges in these samples, it was also found to occur at much lower temperatures than observed in nominally flat continuos SOI films. For patterned mesas in 12nm-thick SOI films, the 10s-UHV-annealing dewetting initiation temperature was observed to be 900C, 150C below the 1050C initiation temperature observed in flat

continuous SOI films of the same 12nm thickness.[5] Continuing with their stress-driven SOI dewetting theory, Ishikawa et al. explained the increased instability of patterned SOI film edges to be due to an increased local stress-driven morphological evolution driving force due to stress concentration at film edges.

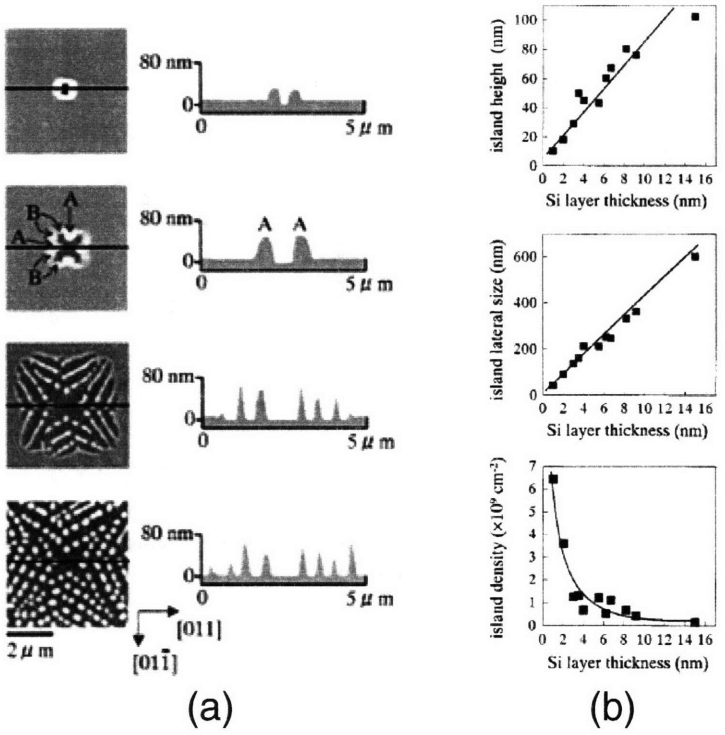

Figure 3.3: Results from the SOI dewetting study of Nuryadi et al. a.) Series of AFM images from a 7nm-thick SOI film annealed at 900C for 10s. Images are from different voids in the sample at various dewetting stages due to different void nucleation times. b.) Plots of the average island geometrical parameters observed by Nuryadi et al. indicating that all of these parameters scale in proportion to the initial Si thickness.[69]

More recently, we argued in the literature against this stress-driven theory and presented the 5-step surface-energy-driven model for SOI dewetting that we present in Chapter 4 of this thesis.[70] Since then, Yang et al.[71] and Sutter et al.[72] have presented experimental results for UHV annealing studies of dewetting in initially continuous (100)-oriented SOI films covered with a native SiO_2 layer before annealing and have

obtained results identical to those seen in Nuryadi et al., with the prominent formation of <310> void fingers, as shown in Figure 3.4(a) from Yang et al. Furthermore, Yang et al. identified that the sides of the Si fingers between propagating <310>-oriented void fingers were faceted on (311) planes as shown in Figure 3.4(b).[71] In these reports, Yang et al. and Sutter et al. subscribed to our surface-energy-driven model, as opposed to the stress-driven model dominant in the rest of the literature.[72]

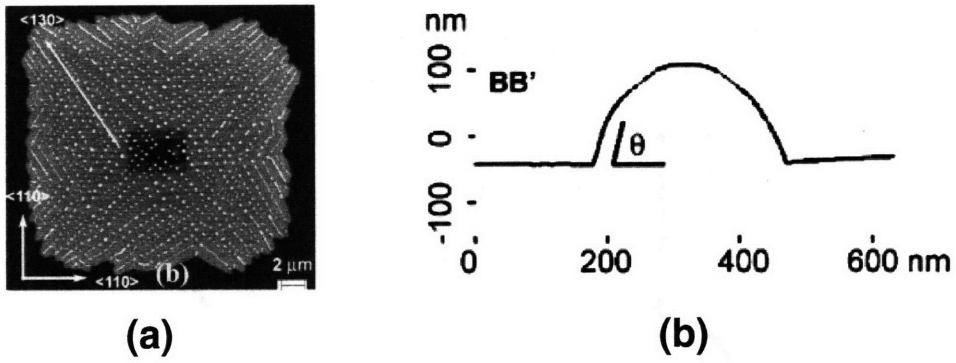

Figure 3.4: AFM image of a 9nm-thick (100)-oriented bonded SOI film UHV annealed at 900C for 5min from Yang et al. a) AFM image of a dewetting film region clearly showing void finger propagation in <310> directions, b.) AFM line-scan perpendicular to a <310>-oriented Si finger indicating a sidewall angle of ~72°, consistent with faceting on the (311) plane.[71]

For reference in the next chapter, in which we argue against the literature consensus theory that SOI dewetting occurs via a film stress-driven mechanism and present what we believe to be a correct theoretical description based upon a surface-energy-driven dewetting model, we summarize here the key experimental observations from the existing literature. Any accurate theoretical description of SOI dewetting must be consistent with and able to explain all of these observations.

SUMMARY OF KEY OBSERVATIONS FROM SOI DEWETTING LITERATURE

1.) In continuous SOI films, dewetting initiates at local, random sites.

2.) In patterned SOI films, dewetting initiates first at patterned film edges.

3.) Patterned SOI film edges are less stable than continuous films to dewetting initiation.

4.) In continuous films, thinner SOI films are less stable against dewetting with stability determined by the Si thickness.

5.) In patterned films, thinner SOI films are less stable against dewetting with stability determined by the Si thickness.

6.) SOI dewetting has been found to occur via void formation, void edge thickening, and the subsequent formation and growth of ordered, equally spaced void fingers forming Si film fingers that break down into ordered rows of Si islands.

7.) The size and spacing of Si islands produced via SOI dewetting has been found to scale in proportion to the SOI thickness.

8.) Dewetting behavior in SOI films has been observed to be completely independent of the thickness of the underlying SiO_2 layer.

9.) The dominant theory in the literature is that SOI dewetting is a stress-driven morphological evolution phenomenon.

Chapter 4:
Surface-Energy-Driven Model of SOI Dewetting

In this chapter, we motivate and present an isotropic surface-energy-driven model for SOI dewetting based upon two key capillary instabilities: 1.) the capillary edge instability and 2.) the generalized Rayleigh instability. We argue for the validity of this surface-energy-driven dewetting theory and against that of the literature consensus theory that SOI dewetting is driven by thermal-expansion-mismatch induced film stress on the basis of 1.) basic thermodynamic considerations, 2.) the consistency of the surface-energy-driven dewetting model with the key experimental observations of SOI dewetting from the literature, and 3.) the inconsistency of the stress-driven theory with experimental observations.[70]

I. Thermodynamics of SOI Dewetting

We begin by demonstrating that any planar top Si SOI layer is morphologically unstable to dewetting from a thermodynamic perspective due to surface energy effects alone. Furthermore, we show that the surface energy reduction associated with dewetting in SOI films greatly exceeds the maximum possible energy reduction associated with stress relaxation, demonstrating that surface energy is the primary driving force behind SOI dewetting.

As reviewed in Chapter 2, in a stress-free SOI film the relative interfacial energies of the system dictate the equilibrium shape of the film. Assuming isotropic surface

energies and a rigid underlying SiO_2 layer, the equilibrium morphology of a thin SOI film will be that of a spherical cap of Si that makes the equilibrium contact angle $\Theta_{c(SOI)}$ with the planar underlying SiO_2 layer dictated by Young's equation, as illustrated in Figure 4.1. This establishes the equilibrium contact angle for SOI under vacuum to be

$$\Theta_{c(SOI)} = \cos^{-1}\left(\frac{\gamma_{SiO_2-vac} - \gamma_{Si-SiO_2}}{\gamma_{Si-vac}}\right), \tag{4.1}$$

where γ_{SiO_2-vac} is the SiO_2-vacuum interfacial energy density, γ_{Si-SiO_2} is the Si-SiO_2 interfacial energy density, and γ_{Si-vac} is the Si-vacuum interfacial energy density.

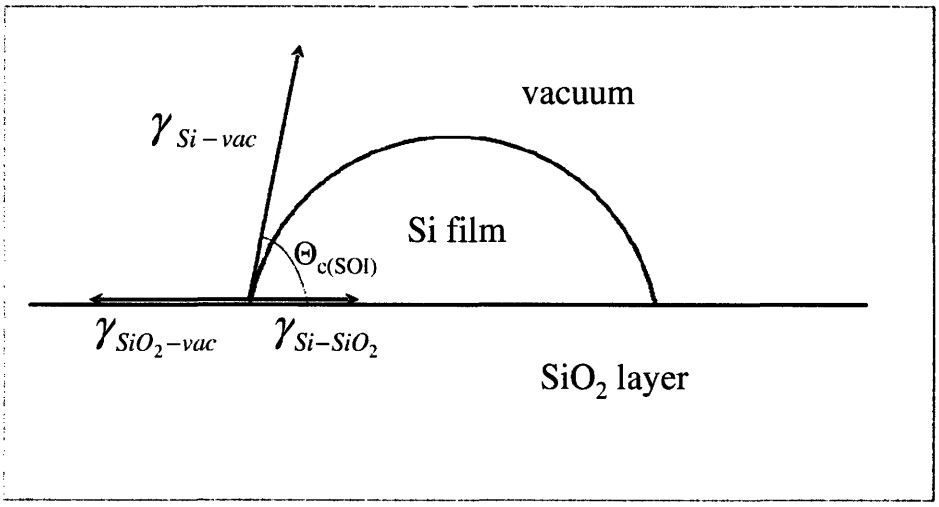

Figure 4.1: Schematic illustration of the equilibrium spherical cap morphology of a SOI thin film assuming isotropic surface energies and a rigid SiO_2 layer. Θ_c~73° for SOI, indicating a strong driving force for a top Si SOI film to dewet, even in the absence of film stress.

For the (100) top Si-oriented SOI film system under vacuum, we use interfacial energy values of γ_{SiO_2-vac} ~0.3 J/m^2,[73] γ_{Si-SiO_2} ~0.75 J/m^2,[74] and γ_{Si-vac} ~1.5 J/m^2.[63] (Since the surface energy density of Si is anisotropic, we have chosen a reasonable value for γ_{Si-vac} that is in the middle of the 1.23-1.72 J/m^2 reported range of experimental and theoretical values for the stable (111), (311), (110), and (100) Si facets.[63-65] Because the

surface energy density of Si is indeed anisotropic and facets exist on its equilibrium shape, a more advanced treatment developed by Winterbottom[75] would be required to calculate the exact equilibrium shape of a crystalline Si film on SiO_2. However, due to the fact that the facet plane surface energy densities in Si differ by only ~5% within a given set of reported values,[63-65] the assumption of isotropic surface energy used here is sufficiently accurate for our current purposes of illustration and comparison of driving forces.) Ignoring surface energy anisotropy, the contact angle for the SOI system under vacuum is calculated from these surface energy density values to be ~73°. This relatively large equilibrium contact angle indicates that the top Si film in SOI does indeed have a large surface-energy-related thermodynamic driving force to dewet.

Furthermore, not only does a surface-energy-related driving force for SOI dewetting exist, this surface energy driving force can be shown to be much larger than the maximum possible driving force associated with stress relaxation that can occur during dewetting. We demonstrate this fact by estimating and comparing the changes in surface energy and strain energy associated with the formation of a single Si island via SOI dewetting.

The model system considered for this calculation is illustrated in Figure 4.2. The surface energy and strain energy changes associated with the formation of a single Si island from a square region of initially flat biaxially stressed SOI film are calculated under the following conservative assumptions (from the perspective of disfavoring surface energy). For simplicity, Si islands are assumed to be hemispherical ($\Theta_{c(SOI)}$=90°). It is also conservatively assumed that Si island formation results in complete stress relaxation in the Si layer. From the results of Nuryadi et al., presented in Figure 3.3(b), it

is also assumed that the island radius scales with the top Si thickness and is proportional to 20 times that thickness.[69] Observed conservation of volume during SOI dewetting, together with this assumed relationship between island radius and top Si thickness, allows all geometrical parameters to be expressed in terms of the top Si thickness h_{Si}.

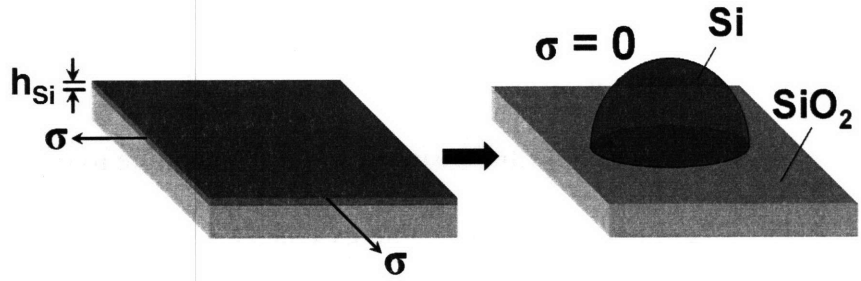

Figure 4.2: Model system considered for the thermodynamic calculation and comparison of the surface energy and strain energy change per Si island formed by SOI dewetting.

Under these assumptions, the changes in surface energy and strain energy, in Joules, associated with the formation of a single Si island via SOI dewetting under vacuum are calculated to be

$$\Delta E_{surface} = -\frac{\pi}{3} h_{Si}^2 \left[13{,}600\gamma_{Si-vac} - 14{,}800\left(\gamma_{SiO_2-vac} - \gamma_{Si-SiO_2}\right)\right] \tag{4.2}$$

$$\Delta E_{strain} = -\frac{\pi}{3} h_{Si}^3 \left[16{,}000\gamma_{Si-vac} \frac{(1-\upsilon_{Si})\sigma_{Si}^2}{E_{Si}} \right], \tag{4.3}$$

where σ_{Si} is the initial biaxial Si film stress, υ_{Si} is the Si Poisson ratio, E_{Si} is the Si elastic modulus, and all other parameters are as previously defined, with the stress and elastic modulus expressed in Pa, the Si thickness in meters, and the surface energy densities in J/m^2.

Figure 4.3 shows how these two energy reduction terms compare as a function of the SOI top Si thickness and the initial biaxial Si film stress, assuming the SOI surface energy density values previously used for the SOI equilibrium contact angle calculation

and values of υ_{Si}=0.28 and E_{Si}=166 GPa from the literature.[68] In the shaded region, the calculated surface energy reduction exceeds the strain energy reduction, with the opposite holding true for the unshaded region. This plot indicates that for the Si thicknesses that have been experimentally observed to undergo dewetting (< 30nm), known from the literature to have biaxial stress values < 100MPa,[76] the calculated surface energy change associated with dewetting far exceeds that associated with stress relaxation. As an illustration, for a 10-nm-thick SOI film, assumed from the literature to have a biaxial film stress of ~65MPa,[76] the ratio of the surface energy change to the strain energy change is calculated to be ~5,000. Comparing Equations 4.2 and 4.3, we immediately see that the ratio of the change in surface energy to the change in strain energy ($\frac{\Delta E_{surface}}{\Delta E_{strain}}$) per island formed scales with $\frac{1}{h_{si}}$, showing clearly why surface energy effects should naturally be dominant in the dewetting of *ultra-thin* SOI films. This simple thermodynamic calculation provides very convincing evidence that SOI dewetting is indeed a surface-energy-driven phenomenon.

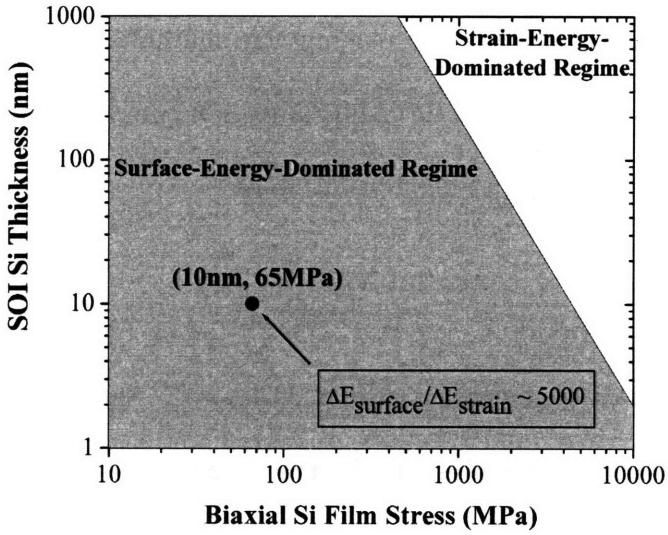

Figure 4.3: Plot comparing the relative magnitudes of the surface energy and strain energy changes associated with the formation of a Si island via dewetting. The plot indicates regimes of SOI thickness and biaxial Si film stress where surface energy reduction (shaded) and strain energy reduction (unshaded) would dominate during SOI dewetting. The SOI films that have been observed to undergo dewetting (h_{Si} < 30nm and σ_{Si} < 100MPa) can be seen to lie well within the surface-energy-dominated regime, strongly indicating that SOI dewetting is a surface-energy-driven phenomenon.

II. Kinetic Model for SOI Dewetting

A. Dewetting Initiation at Pre-Existing Critical Film Voids and Film Defects

As reviewed in Chapter 2, although islanded morphologies may be preferred energetically to a flat Si film in the SOI system, a flat film does indeed represent a metastable state. Surface-energy-driven SOI dewetting must thus initiate through a substrate-exposing film void nucleation and growth process in which a sufficiently large morphological perturbation to expose the underlying SiO_2 layer must first be formed or pre-exist in the film in order for dewetting to proceed spontaneously. As stated in Chapter 2, such a substrate exposing film void must also be greater than a critical size in order for

subsequent void growth and dewetting to be energetically favored. For a truncated conical film void in the top Si film making the equilibrium contact angle with the underlying SiO_2 layer, the critical void radius in an SOI film is calculated from the result of Srolotivz and Safran (found in Equation 2.6) to be[62]

$$r_{crit} = \frac{h_{si}}{\sin \Theta_{c(SOI)}}. \tag{4.4}$$

Inserting our previously calculated value of $\Theta_{c(SOI)}=73°$ into this equation yields an estimate for the critical void radius in SOI that is equal to the top Si layer thickness ($r_{crit}=h_{Si}$). Growth of any void with $r_{void} > r_{crit}$ results in a continuous decrease in the free energy of the system, and thus such supercritical voids can grow spontaneously and result in dewetting. Growth of any film void with $r_{void} < r_{crit}$, on the other hand, results in an increase in free energy, and thus such subcritical voids spontaneously shrink and restore the flat film. This critical void phenomenon is illustrated below in Figure 4.4.

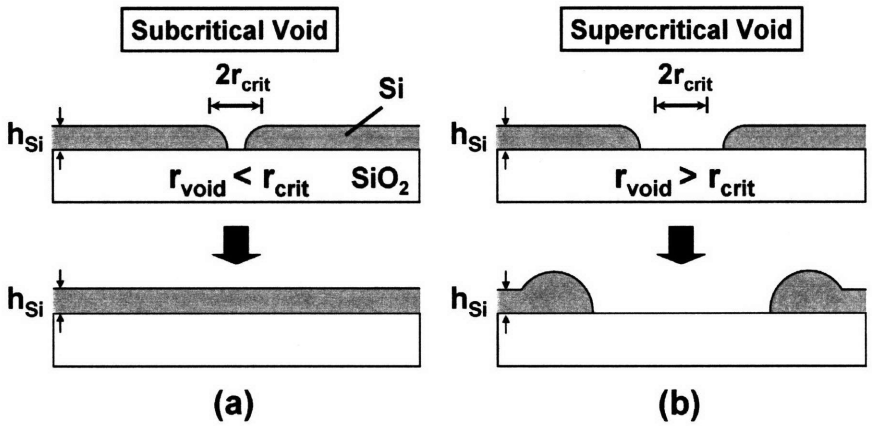

Figure 4.4: Schematic illustration of the critical void phenomenon in SOI dewetting. a) Subcritical voids ($r_{void} < r_{crit}$) spontaneously fill in restoring the flat film. b.) Supercritical voids ($r_{void} < r_{crit}$) once formed spontaneously grow, resulting in the onset of film dewetting.

A straight patterned film edge in a top Si SOI film can be understood to represent the edge of a film void with an infinite effective void radius. Thus, under this model, any

patterned SOI film edge represents the edge of a supercritical void and is thus unstable to dewetting initiation. This explains why SOI film edges have been observed to be more unstable to dewetting initiation than flat continuous SOI film regions. Film edges simply represent the edges of unstable pre-existing supercritical voids in the SOI film.

However, in initially flat continuous film regions, critical film voids must first be formed in order for dewetting to proceed spontaneously. Pre-existing supercritical pinholes, termed "HF defects" in the literature, are known to exist in ultra-thin SOI layers and these pinholes should be as unstable as film edges are to dewetting initiation. However, in state-of-the-art optimized ultra-thin SOI films, the density of these pinholes is typically very low in as-received wafers (< 1 cm^{-2}), and thus they cannot possibly be the cause of the high density of dewetting initiation (> 10^5 cm^{-2})[1,69] that has been observed in initially continuous flat film regions in the existing SOI dewetting literature.

Thus, the dewetting initiation that is observed in initially flat continuous film regions must occur via a film void nucleation process. However, even though the critical void size in any ultra-thin SOI film is extremely small ($r_{crit} = h_{Si} < 30nm$), the homogeneous activation energy required to form even a very small void in a very thin SOI film is prohibitively large, giving a flat defect-free SOI film an amazing degree of metastability against dewetting initiation. This activation energy can be estimated by calculating the amount of energy required to form the sidewall area A_{cyl} of a cylindrical film void with a radius equal to the critical void radius for SOI. For an SOI film with a Si film thickness given by h_{Si}, this estimate gives a homogeneous void nucleation activation barrier of

$$\Delta G_{void} = A_{cyl}\gamma_{Si-vac} = 2\pi r_{crit} h_{Si}\gamma_{Si-vac} = 2\pi h_{Si}^2\gamma_{Si-vac}, \qquad (4.5)$$

where r_{crit} has been taken to be equal to h_{Si} from Equation 4.4. Taking $\gamma_{Si\text{-}vac}$ = 1.5 J/m^2 as before, this approximation indicates that even in a top Si film with a thickness of only 1nm, an activation energy of ~60eV exists to homogeneously nucleate a critical void in an SOI film, and that this value increases with the square of the top Si film thickness. Such high activation barriers are indeed prohibitively large. For this reason, we strongly believe that homogenous critical void nucleation is not a viable dewetting initiation mechanism in initially flat continuous regions in ultra-thin SOI films.

Accordingly, critical void formation in flat continuous SOI film regions must occur via a *heterogeneous* mechanism at defects in the film bulk or interfaces. Of course, any defects that represent supercritical film voids, such as the aforementioned HF defects and film scratches introduced during fabrication or processing, creates a film location that is inherently unstable to void growth and dewetting. In the previously discussed deposited polycrystalline dewetting thin film systems, the obvious heterogeneous void nucleation mechanism is grain boundary grooving at grain boundaries and grain boundary triples points.[37] However, SOI films, being single crystal, do not possess any grain boundaries. Nonetheless, there exist a number of possible defects in SOI films that might act as sites for heterogeneous void nucleation, serving as locations where the nucleation barrier can be sufficiently reduced for void nucleation to be physically observed. Possible heterogeneous nucleation defect sites include crystal-originated particles (COPs), dislocations, stacking faults, oxide precipitates, and surface particles.[77,78] Analagous to the homogeneous case, we expect the heterogeneous void nucleation activation energy to increase quickly with increasing Si thickness, which would explain why thicker SOI films have been observed to be more stable against

dewetting initiation in initially flat continuous film regions. Plausible heterogeneous mechanisms include reduction of the void activation barrier via locally thinner film regions at oxide protrusions, elimination of high energy defects such as dislocations, and high local stress generated at defects. However, the exact defects and physical mechanisms responsible for dewetting in initially flat continuous film regions in ultra-thin SOI films have yet to be definitely determined. We explore this issue in our own experimental SOI dewetting study described in Chapter 6.

The heterogeneous void nucleation mechanism posed here can explain a number of key observations related to SOI dewetting initiation in initially flat continuous film regions, including the locations of dewetting initiation, the lower stability of thinner films against dewetting initiation in flat continuous SOI film regions, as well as the increased instability of film edges to dewetting initiation relative to flat continuous regions. Under this model, the random, local dewetting initiation that has been observed in non-edge SOI film regions can be explained to be the natural result of heterogeneous void nucleation at randomly distributed film defects, while observed initiation at film edges can be understood to be due to the fact that film edges represent the edges of unstable pre-existing supercritical film voids. The observed decreased stability with decreasing Si thickness in SOI films to dewetting initiation in flat continuous film regions can be understood to be the result of the decreased heterogeneous void nucleation activation barrier present in thinner films. The increased instability of edges relative to flat continuous film regions can be understood to be the result of edges representing fundamentally unstable film locations where the void nucleation step has been circumvented.

From the considerations above, SOI dewetting initiation can be understood in terms of a fundamental morphological instability that exists at the edge of any SOI film void having a radius greater than the Si film thickness once it is formed. However, in order to explain the dewetting propagation that has been observed to spread from these unstable film locations, and its observed dependencies, we consider below the kinetic mechanism by which dewetting propagation proceeds.

B. Dewetting Propagation via Capillary Instabilities

Our kinetic model for SOI dewetting propagation at supercritical void edges is based on surface-energy-driven surface-diffusion-induced morphological instabilities, following the fundamental work of Brandon and Bradshaw[35] and Jiran and Thompson.[36] Here, we describe a kinetic model that is able to account for the increased vulnerability of SOI films to dewetting initiation and propagation with decreasing top Si thickness and increasing annealing temperature and that describes the morphology, ordering tendency, and dimensional scaling that have been observed in the islanded SOI structures that result from dewetting.

Assuming isotropic surface energies, as reviewed in Chapter 2, the volumetric surface flux equation (i.e. volume flux along a surface per unit length perpendicular to the flux) for surface-energy-driven surface diffusion is given by

$$J_s = -\frac{D_s \gamma \Omega \nu}{kT} \nabla \kappa(s) \tag{4.6}$$

where D_s is the surface diffusivity, ν is the atomic surface density, Ω is the atomic volume, γ is the surface energy, $\kappa(s)$ is the mean surface curvature along the surface coordinate s, k is the Boltzmann constant, and T is the absolute temperature.

As shown in Equation 4.6, the driving force for atomic surface diffusion along a film surface is determined by the mean surface curvature profile of the film, $\kappa(s)$, with mass being driven to flow from regions of higher mean curvature to lower mean curvature. (To reiterate from Chapter 2, by convention convex surfaces have positive curvature and concave surfaces have negative curvature). The thermally activated surface diffusivity D_S kinetically limits the atomic flux that occurs in response to this curvature related driving force. ($D_S = D_0 \exp(-Q_s/kT)$, where D_0 is the surface diffusion pre-exponential factor and Q_s is the activation energy for surface diffusion) The surface diffusivity's strong positive Arrhenius temperature dependence provides the dominant temperature dependence in surface-energy-driven surface diffusion.

Our model for SOI dewetting propagation is based upon two key morphological instabilities caused by surface-energy-driven surface diffusion: the capillary film edge instability and the generalized Rayleigh instability, which are described below.

CAPILLARY FILM EDGE INSTABILITY

The edge of any supercritical film void in an SOI film is fundamentally unstable to thickening and retraction due to its high local surface curvature. This is the essence of the capillary film edge instability. In this instability, the high positive local surface curvature present at a patterned edge or film void edge drives mass to flow away from the edge toward the neighboring zero curvature flat film region. The kinetics of this edge instability can be shown to increase quickly with decreasing Si film thickness. The following simple geometrical argument illustrates the basic film thickness and temperature dependencies of the capillary film edge instability. From Figure 4.5, it can be

seen that a patterned edge or newly formed supercritical void edge in SOI initially has a surface curvature ($\kappa_{edge} \sim r_{edge}^{-1}$) approximately equal to h_{Si}^{-1} and that the surface distance Δs_{edge} over which the curvature changes from this value to zero approximates a quarter arc of a circle and is given by $\pi h_{Si}/2$. Therefore, at this edge the average local curvature gradient can be approximated by

$$\nabla \kappa(edge) \sim \frac{\Delta \kappa(edge)}{\Delta s(edge)} \sim \frac{1/h_{Si}}{\pi h_{Si}/2} \sim \frac{2}{\pi} \frac{1}{h_{Si}^2} \tag{4.7}$$

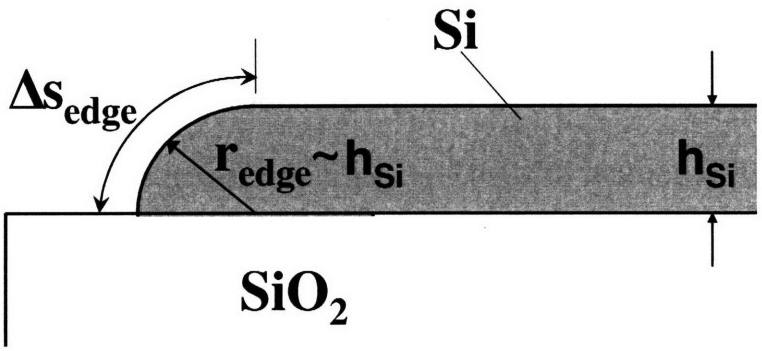

Figure 4.5: Schematic illustration of the capillary film edge instability in SOI. The high edge curvature that exists at a supercritical SOI thin film void edge drives mass to flow away from the edge, making it morphologically unstable to edge thickening and retraction. The edge radius can be seen to be equal to the film thickness h_{Si}. The edge curvature, equal to r_{edge}^{-1}, can be seen to be equal to h_{Si}^{-1} from this figure, indicating that thinner SOI films have higher edge curvature and are thus more vulnerable to the capillary film edge instability.

The local surface diffusion flux at the film edge, J_s, proportional to the edge curvature gradient through Equation 4.6, has this same inverse square dependence on Si film thickness.

The edge retraction rate at a newly formed patterned film edge or film void edge scales with the ratio of the local surface flux to the amount of film material that must be moved for the edge to move a unit distance. This amount of film material is proportional to the film thickness h_{Si}. Thus, under the capillary film edge instability, the initial void

edge retraction velocity at an edge, v_{void}, should have, the following Si thickness and temperature dependencies:

$$v_{void} \propto \frac{D_{s(Si)}}{T}\frac{1}{h_{Si}^3}, \tag{4.8}$$

where $D_{s(Si)}$ is the Si surface diffusivity.

The capillary film edge instability is illustrated by this simple analysis. It can be seen that there exists a capillary edge instability that drives the retraction of any dewetting film void edge and that the initial void growth velocity in this instability increases quickly with decreasing film edge thickness due to an increased edge curvature gradient and decreased amount of film edge material, and with increasing temperature due to the overwhelming positive temperature dependence of the surface diffusivity.

GENERALIZED RAYLEIGH INSTABILITY

In the canonical Rayleigh instability, a high-aspect-ratio cylindrical object continuously lowers its total surface energy by breaking up into a row of identical spherical particles having a highly characteristic and uniform size and separation, as illustrated in Figure 4.6. The characteristic wavelength is proportional to the initial cylinder radius R_{cyl} and is independent of temperature,

$$\lambda_{Rayleigh} \propto R_{cyl}, \tag{4.9}$$

while the characteristic evolution time scale of the Rayleigh instability under surface-diffusion-dominated transport has the following dependencies on temperature and cylinder radius:

$$t_{Rayleigh} \propto \frac{T}{D_s}R_{cyl}^4, \tag{4.10}$$

where all parameters are as previously defined.

From Equations 4.9 and 4.10, it is clearly seen that the wavelength of the canonical Rayleigh instability increases in proportion to the cylinder's initial characteristic cross-sectional dimension and is independent of temperature, while the evolution time scale of the Rayleigh instability increases with the fourth power of the initial characteristic cross-sectional dimension and decreases strongly with increasing temperature through the surface diffusivity. All of these key dependencies hold true for *generalized* Rayleigh instabilities, in which an arbitrarily shaped high-aspect-ratio object breaks up into a row of identical particles having a highly characteristic size and spacing, such as occurs in the generalized Rayleigh breakdown of uniformly thickened dewetting SOI film void edges and Si film fingers on SiO_2, as described in the next section.

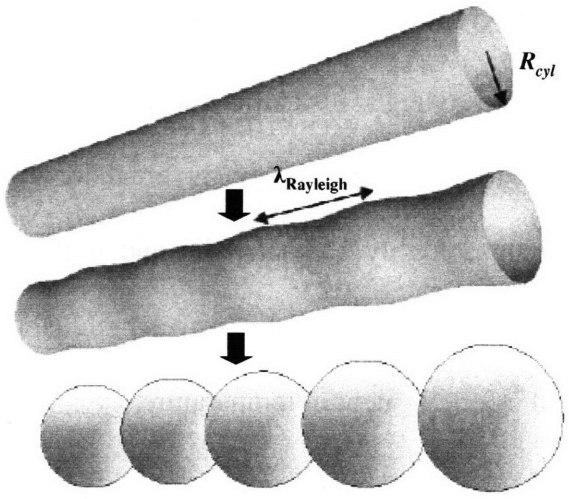

Figure 4.6: Schematic illustration of the canonical Rayleigh instability, in which a cylindrical object with initial radius R_{cyl} continuously lowers its surface energy by breaking up into a row of identical spherical particles having a highly characteristic spacing $\lambda_{Raylcigh}$.[79]

i. Dewetting Propagation Model

Our kinetic model for SOI dewetting propagation consists of the following five distinct steps.

(I) critical void formation,

(II) void edge thickening and retraction,

(III) void edge breakdown,

(IV) void finger formation and propagation, and

(V) island formation.

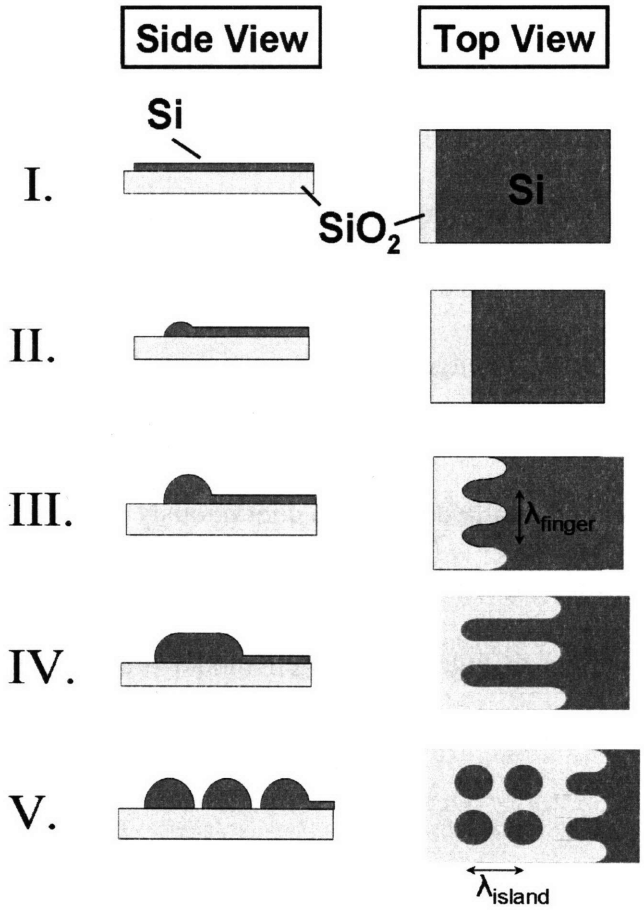

Figure 4.7: Schematic illustration of our 5-step surface-energy-driven model for SOI dewetting.[70]

I.) Critical Void Formation

Step (I) in this model is critical void formation and is illustrated in Figure 4.7(I). As has already been described, a critical void must first be formed in order for surface-energy-driven dewetting to proceed spontaneously. Once again, pre-existing supercritical voids, such as exist at patterned film edges, and nucleated film voids both represent unstable supercritical voids. As stated previously, it is this step that determines the locations where dewetting can proceed.

II.) Void Edge Thickening

In step (II) of our kinetic model for dewetting, void edge thickening, the capillary film edge instability that exists initially at a supercritical void edge causes mass to flow from this edge to the neighboring flat film region and results in a continuous uniform edge thickening with time. As reviewed in Chapter 2, Brandon and Bradshaw developed a model for void growth via void edge thickening and retraction for a circular void, such as would occur for a pre-existing or nucleated film void in an initially flat continuous film region.[35] The model essentially describes a continuously slowing edge instability due to a continuously increasing edge thickness caused by the pile-up of film material at the edge as it retracts, as shown in Fig 4.7(II). Their model predicts an expression for the circular void radius, r_{void}, during void growth via uniform edge thickening and retraction given by

$$r_{void} = \left(\frac{25\pi}{4}\right)^{\frac{1}{5}} \left(\frac{D\gamma\Omega^2\nu}{kT}\right)^{\frac{2}{5}} \frac{t^{\frac{2}{5}}}{h_f^{\frac{3}{5}}}, \tag{4.11}$$

where t is the annealing time and all other parameters are as previously defined.[35]

Since our own experimental work, which we describe in detail in Chapters 5 and 6, has focused on dewetting initiation not at circular voids but at straight patterned film edges, we derive here for the first time an expression for the edge retraction distance, r_{edge}, versus time for a thickening retracting edge at an initially straight patterned film edge, following the same basic approach as Brandon and Bradshaw.[35]

The two key assumptions underpinning this model are that the thickening edge maintains a semicircular cross-sectional profile and that the semicircular edge contains all of the mass that has been moved during the edge thickening and retraction process. The atomic flux per unit length along the thickened edge (this edge goes into the plane of Figure 4.8) from the edge to the neighboring flat film region is given by

$$J_s = -\frac{D_s \nu}{kT} \nabla \mu(edge). \tag{4.12}$$

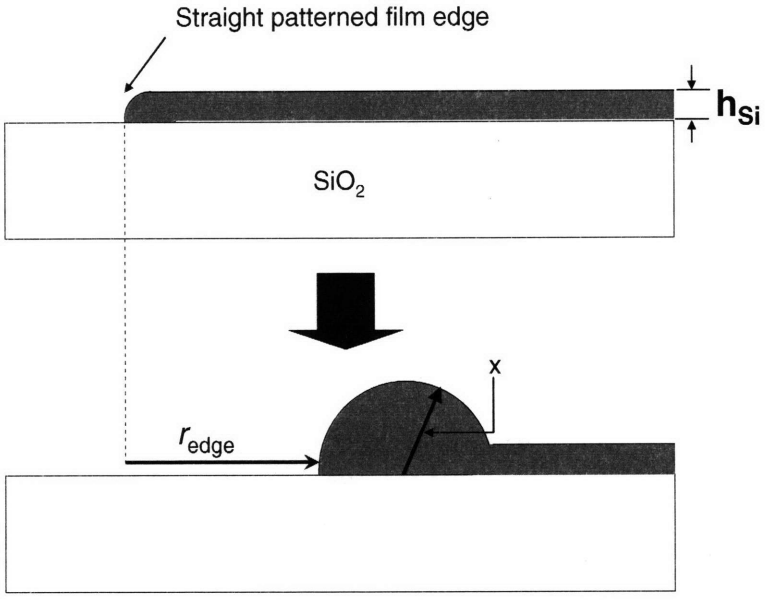

Figure 4.8: Schematic diagram showing the key parameters and geometry for our derivation of an expression for the edge retraction distance, r_{edge}, of a retracting thickening dewetting edge at an initially straight patterned film edge.

As in the case of the capillary film edge instability, the chemical potential gradient at the edge is approximated by

$$\nabla\mu(edge) = \Omega\gamma\nabla\kappa(edge) = \Omega\gamma\frac{\Delta\kappa(edge)}{\Delta s(edge)} = -\Omega\gamma\frac{\frac{1}{x}}{2\pi x} = -\frac{\Omega\gamma}{2\pi x^2} \tag{4.13}$$

where x is the radius of the semi-circular thickened edge, as shown in Figure 4.8. Substituting this expression for the chemical potential gradient into the flux equation in Equation 4.12 yields

$$J_s = \frac{D_s\gamma\Omega\nu}{2\pi kT}\frac{1}{x^2}. \tag{4.14}$$

The total volume transfer from the thickened edge to the neighboring flat region per unit time, $\frac{dV}{dt}$, per unit length along the thickened edge is given by

$$\frac{dV}{dt} = J_s \bullet \Omega \bullet 1 = \frac{D_s\gamma\Omega^2\nu}{2\pi kT}\frac{1}{x^2}. \tag{4.15}$$

By the same assumption, the differential mass dV that flows from the thickened edge to the neighboring flat film region and is integrated into the moving thickening semicircular edge itself is given by

$$dV = \pi x dx \Rightarrow \frac{dV}{dt} = \pi x\frac{dx}{dt}. \tag{4.16}$$

Equating equations 4.15 and 4.16 yields

$$\pi x\frac{dx}{dt} = \frac{D_s\gamma\Omega^2\nu}{2\pi kT}\frac{1}{x^2} \tag{4.17}$$

$$x^3 dx = \frac{D_s\gamma\Omega^2\nu}{2\pi^2 kT}dt \tag{4.18}$$

By the assumption that all of the volume moved by the retracting edge is contained in the semi-circular thickened edge, we have

$$r_{edge}h_{Si} = \frac{\pi x^2}{2} \Rightarrow x^2 = \frac{2}{\pi} r_{edge} h_{Si} \Rightarrow x = \sqrt{\frac{2h_{Si}}{\pi}} \sqrt{r_{edge}} \tag{4.19}$$

$$dx = \frac{\sqrt{\frac{t_{Si}}{2\pi}}}{\sqrt{r_{edge}}} dr_{edge} \tag{4.20}$$

Substituting for x and dx in Equation 4.18

$$\frac{2}{\pi^2} h_{Si}^2 r_{edge} dr_{edge} = \frac{D_s \gamma \Omega^2 \nu}{2\pi^2 kT} dt \Rightarrow r_{edge} dr_{edge} = \frac{D_s \gamma \Omega^2 \nu}{4kT} \frac{1}{h_{Si}^2} dt \tag{4.21}$$

Integrating the expression on the right hand side above and taking an integration constant of zero since r_{edge}=0 at time=0 yields

$$\frac{r_{edge}^2}{2} = \frac{D_s \gamma \Omega^2 \nu}{4kT} \frac{1}{h_{Si}^2} t \tag{4.22}$$

which gives the final result

$$\boxed{r_{edge} = \sqrt{\frac{D_s \gamma \Omega^2 \nu}{2kT} \frac{1}{h_{Si}}} \sqrt{t}} \tag{4.23}$$

Similar to what is predicted by the Brandon and Bradshaw model for the circular void case,[35] this expression predicts that the edge retraction distance during edge thickening of a straight patterned film edge should slow with time and be slower for thicker films. However, it is quite interesting that the power law dependencies of the edge retraction distance are slightly different between the two cases: a 0.5 power law time dependence for the straight edge versus the 0.4 power law time dependence for the circular void, and a -1.0 power law film thickness dependence for the straight edge versus the -0.6 power law for the circular void.

Both the Brandon and Bradshaw model and the straight film edge retraction model presented here indicate that the edge thickening step of dewetting alone does not provide for the continued film evolution that has been observed in SOI dewetting. As void growth/edge thickening and retraction proceeds, film material piles up at the moving edge as shown in Figures 4.7(II) and 4.8, and accordingly the edge thickness increases with time, causing the severity of the capillary film edge instability, and thus the edge retraction velocity, to decrease with time, as illustrated in Equations 4.11 and 4.23. Void growth occurring by this mechanism alone would continuously slow and stop, unless void impingement occurred before the void growth velocity decreased to a negligible value.

III.) Void Edge Breakdown

Continued dewetting occurs via thickened edge breakdown, step (III) in our model, as illustrated in Figure 4.7(III). Jiran and Thompson were the first to propose that continued dewetting occurs via a morphological instability in the stalled, thickened void edge that results from the uniform edge thickening mechanism in step (II), but did not explicitly identify the specific breakdown mechanism.[36] We propose that this breakdown occurs via a generalized Rayleigh instability in the thickened void edge. Recent numerical modeling by Kan and Wong strongly supports this mechanism, as illustrated in Figure 4.9.[80] In this work, it was demonstrated numerically that a thickening retracting dewetting film edge should undergo a generalized Rayleigh instability whose wavelength, λ_{finger} in Figure 4.7(III), is proportional to the initial film thickness and independent of temperature, as expected for a Rayleigh instability, and was found to be equal to

$$\lambda_{finger} = \frac{2\pi}{k_m \Theta_c} h_f \,, \tag{4.24}$$

where k_m is a dimensionless parameter that was numerically solved to be 0.0685 and all other parameters are as previously defined.[80] Inserting this value and the previously calculated value of $\Theta_{c(SOI)}$=73° into the above equation yields a predicted edge breakdown wavelength in SOI given by

$$\lambda_{finger}(SOI) \sim 70 h_{Si} \tag{4.25}$$

Furthermore, for SOI the work of Kan and Wong predicts that the characteristic timescale over which this instability (which includes both steps (II) and (III) in our model) occurs should have the following Si thickness and temperature dependencies.

$$t_{edge-breakdown} \propto \frac{T}{D_{s(Si)}} h_{Si}^4 . \tag{4.26}$$

The predicted strong decrease in the edge breakdown time with decreasing Si thickness and with increasing temperature through the surface diffusivity shown in Equation 4.26 is consistent with the fact that thinner SOI films and higher temperatures have been experimentally observed to result more readily in dewetting initiation at patterned SOI edges.

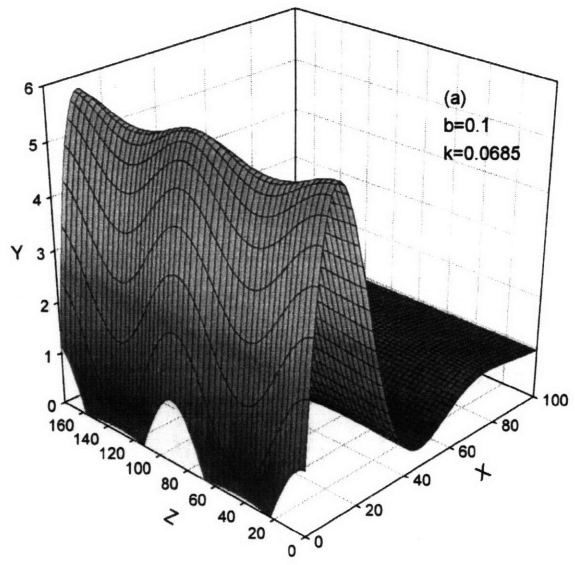

Figure 4.9: Schematic illustration of the breakdown of a thickening retracting dewetting film edge by a generalized Rayleigh instability, as first quantitatively modeled by Kan and Wong.[80]

IV). Void Finger Formation and Growth

Step (IV) in our kinetic dewetting model is void finger formation and growth. In this step, the locally thinner edge regions resulting from the thickened edge Rayleigh instability in step (III) break down and form into void fingers due to their high local edge curvature, as shown in Figure 4.7(IV). This high local edge curvature drives mass to flow rapidly away from these regions, resulting in the penetration and growth of equally spaced void fingers through the broken down edge and into the neighboring flat film. As these void fingers grow, an equally spaced array of parallel Si fingers, having spacing given by λ_{finger}, is formed between them. The critical location that determines void finger growth kinetics is the tip of the growing void finger. As noted first by Jiran and Thompson,[36] these void finger tips are able to continuously maintain a local edge thickness equal to the initial film thickness due to their ability to move mass laterally away to the Si film fingers between them. This allows void fingers to grow at a constant rate that is determined by the capillary film edge instability. Using this model, Jiran and

Thompson derived an expression for the void finger growth velocity, $v_{void\text{-}finger}$, that for SOI gives

$$v_{void-finger} = \frac{2}{\pi} \frac{D_{s(Si)} \gamma_{Si-vac} \Omega_{Si}^2 \nu_{Si}}{kT} \frac{1}{h_{Si}^3}, \tag{4.27}$$

where Ω_{Si} is the atomic volume of Si, ν_{Si} is the atomic surface density of Si, and all other parameters are as previously defined.[36] This expression exhibits the exact same thickness and temperature dependencies as the capillary film edge instability. Under this model, the uniform spacing of void fingers is determined by the edge breakdown process of step (III) to be equal to λ_{finger}, which from the previously stated results of Kan and Wong should be proportional to the Si thickness and is predicted to be ~$70t_{Si}$ for SOI. We compare this result to our experimental measurements of edge breakdown wavelength versus SOI thickness in Chapter 6. According to our model, it is this void finger growth step that determines the rate at which film dewetting propagation occurs once it has initiated. From the inverse cubic dependence of the void finger growth velocity on the Si thickness, it can be seen that thinner films should undergo dewetting propagation at a much higher rate.

V.) Island Formation

In step (V) of our model, island formation, the uniformly spaced Si fingers formed in step (IV) break up into discrete islands via a second generalized Rayleigh instability, as shown in Fig 4.7(V). McCallum et al. numerically analyzed the morphological stability of a semi-cylindrical line of film material making its equilibrium contact angle with an underlying substrate and, as illustrated in Fig 4.10, found that such a line should be subject to a generalized Rayleigh instability in which, for a given thin film materials system, the breakup wavelength is proportional to the initial cross-

sectional dimension of the line and independent of temperature.[81] They calculated the Rayleigh breakdown wavelength in the finger, λ_{island} in Figures 4.7(V) and 4.10, to be given by

$$\lambda_{island} = \frac{1}{k_m}\sqrt{\frac{\Theta_c - \sin\Theta_c \cos\Theta_c}{\pi \sin^2\Theta_c}}W, \tag{4.28}$$

where W is the width of the finger as measured by the distance between the two parallel lines of intersection of the initial cylinder with the substrate, as shown in Figure 4.10, k_m is a numerically solved constant depending only on Θ_c and increasing with increasing Θ_c, and the rest of the parameters are as previously defined. Using the previously calculated SOI contact angle of 73°, the relationship for SOI is predicted to be

$$\lambda_{finger}(SOI) \sim 8.0W \tag{4.29}$$

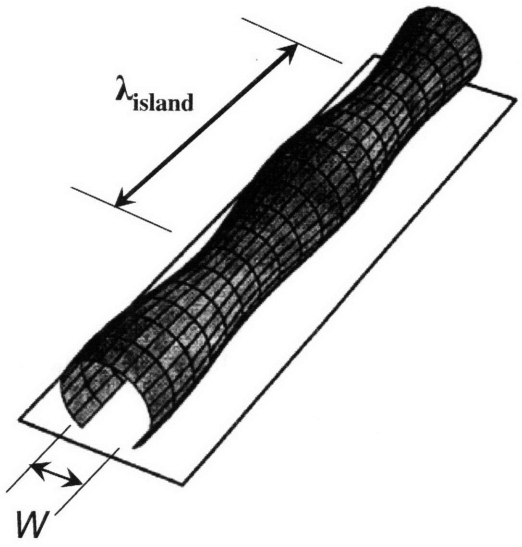

Figure 4.10: Schematic illustration of the generalized Rayleigh instability in a film finger making its equilibrium contact angle with an underlying substrate, as analyzed by McCallum et al.[81]

The kinetics of film finger breakup in step (V) have the same top Si thickness and temperature dependencies as the generalized Rayleigh instability in step (II), indicated in Equation 4.26, and thus the characteristic time for island formation from the Si fingers, t_{island}, is predicted under this model to decrease quickly with decreasing top Si thickness and increasing temperature, just as in step (III).

III. Consistency with Experimental Observations: Surface-Energy-Driven Model vs Strain-Driven Model

A. Consistency of Surface-Energy-Driven Dewetting Model with Experiment

Having described our surface-energy-driven SOI dewetting model in detail, we now explain how this model is able to account for the key experimental observations from the existing SOI dewetting literature. The ability of our model to account for the key experimental observations in SOI dewetting is summarized in Table 4.1 below.[70]

Experimental observation	Surface-energy-driven model explanation
Spatial nature of agglomeration initiation	
Nonedge regions—local, random initiation	Heterogenous void nucleation at film defects.
Patterned films—edge initiation	Edges are preexisting unstable supercritical voids.
Agglomeration stability	
Patterned edges less stable than nonedge regions	Edges are unstable supercritical voids, void nucleation circumvented.
Nonedge regions—thinner SOI films less stable	Lower heterogenous void nucleation barrier: $\Delta G_{void} \propto t_{Si}^2$.
Film edges—thinner SOI films less stable	Propagation kinetics increase with increased T and decreased t_{Si} —generalized Rayleigh instability: $t_{edge\ breakdown} \propto t_{Si}^4/D_{s,Si}$ —capillary edge instability: $v_{finger} \propto D_{s,Si}/t_{Si}^3$
Agglomeration morphology	
Ordered void finger and island formation	Five-step kinetic model explains morphology. Order is due to generalized Rayleigh instabilities.
Agglomerated structure dimensions $\propto t_{Si}$	Generalized Rayleigh instabilities: $\lambda_{finger}, \lambda_{island} \propto t_{Si}$, independent of T.
Agglomeration behavior independent of SiO_2 thickness	SiO_2 thickness plays no role.

Table 4.1: Summary of the ability of the surface-energy-driven dewetting model posed in this work to account for all key experimental observations of SOI dewetting from the literature.[70]

First, the surface-energy-driven dewetting model presented here is able to account for the observed spatial nature of SOI dewetting initiation and growth. The model is able to explain the observed local and random initiation of SOI dewetting in initially flat continuous film regions to be the result of heterogeneous void nucleation at randomly distributed film defects. Under our model, the edge dewetting initiation that has been observed at patterned film edges is explained to simply be due to the fact that these edges represent the edges of pre-existing fundamentally unstable supercritical voids.

Secondly, the model is able to account for the key experimental dependencies of the thermal stability of SOI films against dewetting, including the determining role played by the Si layer thickness. The decreased stability of thinner films against nucleation in initially flat continuous film regions is explained by our model to be the result of the decreased stability of thinner films against critical void nucleation due to a decreased void nucleation barrier present in thinner films.

The decreased stability of film edges to dewetting initiation relative to continuous flat film regions is explained by our model to be the natural result of film edges representing pre-existing unstable critical void edges at which void nucleation has been circumvented. The model is further able to explain why thinner films are less stable against dewetting initiation and propagation once a critical void has been created in an SOI film. The capillary edge instability and the generalized Rayleigh instability that are responsible for dewetting propagation under our model both have evolution rates that increase rapidly with temperature through the thermally activated surface diffusivity and that increase with decreasing Si film thickness according to inverse power laws, as seen

in Equations 4.11, 4.23, 4.26, and 4.27, describing the evolution rates of each of the steps in our kinetic model.

Third, our kinetic dewetting propagation model is able to explain the origin of the morphology observed in SOI dewetting. The surface-energy-instability-driven void edge thickening and breakdown, void finger formation and growth, and island formation mechanism described in our model, illustrated in Figure 4.7, accounts very well for the experimentally observed void finger and island formation morphology observed in SOI dewetting, as shown in Figs 3.3(a) and 3.4(a) from the literature. Our proposed dewetting propagation mechanism explains the ordered Si island arrays that have been observed in SOI dewetting to be a natural result of the ordering tendency inherent in generalized Rayleigh instabilities.

Furthermore, the dewetting propagation mechanism presented here is able to explain why the finger/island length and size scales in dewetted SOI structures are observed to be proportional to the top Si thickness, even when annealed at different temperatures. Under our model, this scaling is a natural result of the temperature independence and proportionality of the Rayleigh instability breakup length scales in steps (III) and (V), λ_{finger} and λ_{island}, respectively, with the top Si thickness.

Finally, the dewetting model presented here is consistent with the experimental observation that SOI dewetting behavior has been observed to be independent of the SOI buried SiO_2 layer thickness. The buried SiO_2 layer thickness does not play any role in the model we have presented here.

B. Inconsistency of Stress-Driven Dewetting Model with Experiment

In this section, we show that the literature consensus theory that SOI dewetting is a stress-driven morphological evolution phenomenon is inconsistent with experimental observations from the literature.

First, the stress-driven theory is not able to account for the observed local spatial nature of SOI dewetting initiation at random, local points in flat continuous films and at film edges in patterned SOI films. The stress-driven theory of film roughening and break-up was pioneered by Asaro and Tiller[66] and Grinfel'd[67] (in fact the roughening mechanism is often called the "Asaro-Tiller-Grinfel'd" instability) and was significantly extended and further developed for mismatched heteroepitaxial films by Gao and Nix.[68] In stress-driven thin film roughening and breakup, a periodic roughness with a characteristic wavelength develops not locally, but simultaneously across the whole film, as shown in Figure 4.11 for a highly strained SiGe film grown on Si.[68] Thus, the stress-driven film breakup mechanism is inconsistent with the local dewetting initiation that has been observed in SOI dewetting.

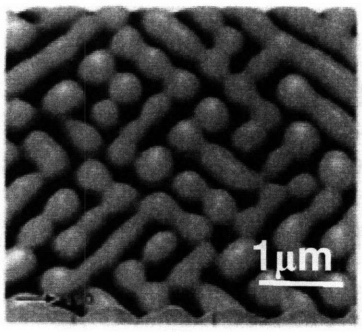

Figure 4.11: AFM micrograph of stress-driven film roughening and breakdown in a 10nm epitaxial $Si_{0.82}Ge_{0.18}$ film on Si after a 1 min anneal at 850C. Note the breakdown occurs across the whole film simultaneously, inconsistent with the initial local breakdown observed in SOI dewetting.[68]

Furthermore, the explanation by proponents of the stress-driven theory of SOI dewetting that patterned film edges are more unstable than initially continuous flat film regions due to stress-concentration at film edges is based upon a false premise. Both theoretical and experimental studies on the subject have shown that film stress is actually relaxed at patterned edges in stressed films.[82-84]

Finally, film stress in the top Si layer introduced due to the thermal expansion mismatch between Si and SiO_2 depends strongly on the thickness of the underlying SiO_2 layer in SOI.[85] The fact that dewetting behavior has been observed to be completely independent of the SiO_2 layer thickness provides further evidence that SOI dewetting is not a stress-driven phenomenon.

Summary

In this chapter we presented a surface-energy-driven model for SOI dewetting based upon critical void formation and void growth via capillary instabilities. We have shown that the surface energy driving force for SOI dewetting far exceeds that due to stress relaxation. We have also shown that our surface-energy-driven dewetting model for SOI is able to account well for all of the key experimental observations of SOI dewetting from the literature, while the stress-driven model is not. Together, we believe that these observations provide convincing evidence that our surface-energy-driven SOI dewetting model is the correct model for this phenomenon.

Chapter 5
SOI Dewetting Study – Experimental Details

In this chapter, we describe the experimental details of a first-of-a-kind fundamental study of the kinetics of dewetting in ultra-thin SOI films. The experimental details of this study were carefully chosen and controlled to enable both a qualitative understanding and a quantitative determination of the key kinetic dependencies of SOI dewetting. In this study, we focused on a quantitative study of the kinetics of 1.) the initial edge retraction and thickening mechanism at dewetting patterned film edges 2.) the Rayleigh breakdown of thickened dewetting film edges, and 3.) the formation and propagation of film void fingers by which continued dewetting occurs.

In order to allow for a careful study of only the kinetics of SOI dewetting and not of a convolution of critical void nucleation and thermal oxide desorption along with the dewetting process, we focused our attention on dewetting in patterned SOI mesa structures, following Jiran and Thompson,[36] and used a pre-anneal sample cleaning procedure that included a final dilute HF dip to provide an SiO_2-free silicon surface immediately prior to annealing. Furthermore, in order to study anisotropic effects in SOI dewetting, we have also for the first time performed a systematic study of the effect of in-plane SOI mesa-edge orientation on dewetting. In addition, we describe and demonstrate a novel SOI film dewetting stabilization concept, dielectric SOI film-edge coverage, for the first time.

Sample Description

In this work, a systematic ultra-thin SOI dewetting study was performed by UHV annealing of (100)-oriented top Si SOI samples of various thicknesses over a range of temperatures and times. The bulk of the SOI samples used in this work came from bonded SOI wafers with lightly B doped (10Ωcm) top Si layers and underlying Si substrates obtained from a leading commercial SOI supplier. Samples were received in the form of 300mm bonded SOI wafers with a buried SiO_2 layer thickness of 145nm and top Si layer thicknesses ranging from 5.0nm to 50.0nm. These samples of various top Si thicknesses were obtained by uniformly thinning down initially 50.0nm thick layers via a layer removal process based on successive consumption of small amounts of the top Si layer via dry thermal oxidation and oxide layer removal via etching in a dilute HF solution.

The sample set used in this study consisted of SOI samples having nominal average top Si thicknesses of 5nm, 10nm, 15nm, 20nm, 35nm, and 50nm. (Note: throughout this study, these samples will be identified by referencing these nominal average thickness values.) The actual top Si layer thicknesses for these samples, representing average thickness values and total thickness value range variations determined from a 300-point spectroscopic ellipsometry measurement across the 300mm substrates, were: 5.0±0.8nm, 10.4±0.9nm, 15.2±0.9nm, 20.1±1.1nm, 35.4±1.2, and 49.8±1.0nm.

To compare dewetting kinetics in bonded and SIMOX films, samples from a 200mm SIMOX SOI substrate obtained from commercial SiMOX SOI wafer supplier were also used in this study. From a 300-point spectroscopic ellipsometry measurement

across the whole 200mm wafer, the average top Si thickness and Si thickness range of this sample was determined to be 20.2nm±2.0nm. However, all annealing experiments performed on this sample were in fact performed on samples from a cleaved 40mm square piece of this wafer having average Si thickness and Si thickness variation given by 20.0±0.6nm.

Sample Preparation

To fabricate samples with patterned Si mesa structures, the SOI wafers were first cleaved into 40mm square pieces, which naturally cleave with edge orientations parallel to the in-plane <110> directions of the underlying (100)-oriented silicon substrate of the SOI wafer. The top Si layers in these samples had identical orientations to the underlying Si substrates. After wafer cleaving, organic contamination and surface particles were removed using a standard 10min 3:1 H_2SO_4/H_2O_2 "piranha" wet clean, followed by 5 minute deonized water rinsing and sample drying with compressed nitrogen. Si top layer SOI mesa structures were then formed from these cleaved samples via photolithography followed by an SF_6-based isotropic plasma Si etch, selective to the underlying SiO_2, using a Surface Technology Systems™ Inductively Coupled Plasma dry etching system. Etch times of 15-60s were used along with a 120W platen power. The photoresist was then removed using two 30min iterations of the aforementioned H_2SO_4/H_2O_2 wet clean, followed by deonized water rinsing and sample drying with compressed nitrogen. Figure 5.1 shows the resultant etched Si mesa structure created by this dry etching process. It can clearly be seen that the etch used was slightly more aggressive than desired, resulting in overetching of the Si mesa laterally underneath the edge initially defined by the

photoresist. The etched edge also shows some degree of roughness as a result of the aggressiveness of the etch. Ideally, perfectly straight etched mesa edges would be preferred for a controlled study of SOI dewetting. However, due to process compatibility constraints, the plasma etch technique described here was the best mesa patterning method available for this study.

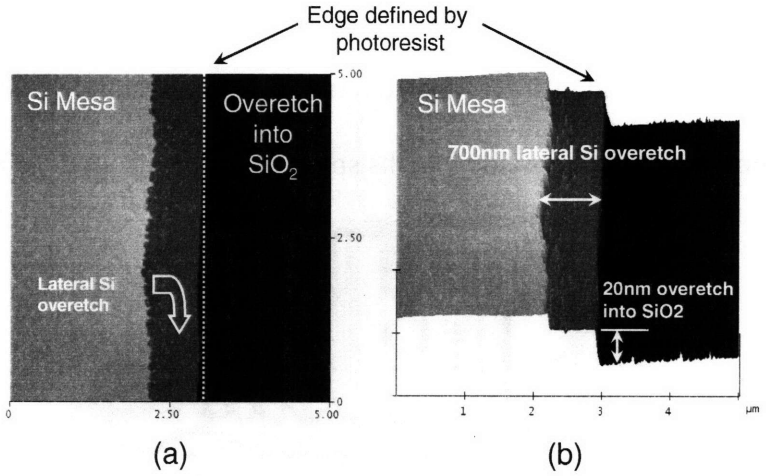

Figure 5.1: AFM images illustrating the structure of the patterned Si mesas after plasma dry etching. The etch can be seen to have laterally etched ~700nm beneath the edge as initially defined by the photoresist and edge roughness is visible. a.) Plan view AFM image of an etched edge in a 10nm-thick bonded SOI film. b.) Bird's eye view AFM image of the same edge, showing the overetch into the underlying SiO_2 layer as well as the lateral overetch of the Si mesa.

The photolithography mask pattern used to make the patterned top Si SOI mesa structures in this work can be seen in Figure 5.2. The mask was designed such that its edges were to be aligned with the <110> in-plane edges of the cleaved SOI pieces. Misorientations of < 1° were readily achieved. The mask contained rectangular mesa patterns with widths ranging from 3-200μm and with edge orientations relative to the horizontal <110> in-plane direction in the mask given by 0, 10, 19.47, 20, 26.57, 30, 35.26, 40, 45, 50, 54.74, 60, 63.43, 64.76, 70, 80, 90 degrees. The 0° and 90° mesas had edges parallel to the in-plane <110> directions of the (100)-oriented top Si layer, the 45°

mesa edges parallel to the in-plane <100> directions, and the 26.57° and 63.43° mesas edges parallel to the in-plane <310> directions. The other angle orientations that are multiples of 10° were used to explore the general behavior at non-special edge orientations, while the other non-integer angle mesas represented special in-plane directions for (110)-oriented top Si SOI layers, which did not become available for this study. The mask also contained square mesas with edges parallel to the in-plane <110> directions of (100)-oriented SOI and circular mesas containing all in-plane edge orientations, both having radius/side lengths spanning the range of 2-1000μm.

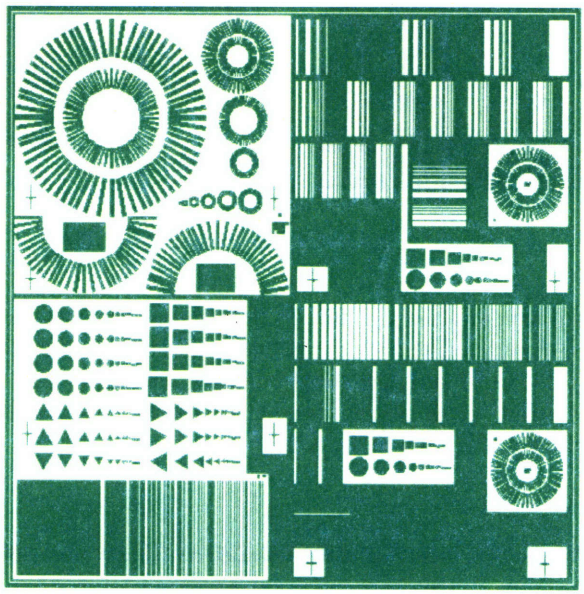

Figure 5.2: Photolithography mask pattern used to fabricate the top Si SOI mesa structures used in this dewetting study. The edges outlining the pattern above were aligned with the <110>-oriented cleaved edges of SOI samples. Shaded regions represent where Si remained after the etch, white regions represent where the Si was etched away.

Annealing Studies of Dewetting

The UHV annealing furnace used for the dewetting studies in this work was a load-locked hot-walled UHV-CVD reactor with a base pressure of $5x10^{-8}$ torr and background partial pressures of O_2 and H_20 of $< 5x10^{-9}$ torr. The hot zone of this UHV-CVD reactor consisted of a high purity quartz tube surrounded by a three-zone resistive

tube furnace. The chamber was pumped by a Turbo pump backed by a mechanical pump and a roots blower pump. The load lock was pumped by a turbo pump and a mechanical pump.

For annealing studies, the patterned 40mm square cleaved samples were further cleaved down into 10x10mm samples representing a single quadrant of the pattern shown in Figure 5.2 and were subjected to the following standard pre-anneal cleaning procedure. Compressed nitrogen was first used to physically remove any small particles left on the surface after cleaving. A 5min 3:1 H_2SO_4/H_2O_2 "piranha" wet clean was then performed to remove organic contamination and any remaining particles left by the cleaving process. The sample was then rinsed for 2 min in deionized water. The thin native SiO_2 layer present on the top Si SOI layer was then removed using a 30s 20:1 H_2O:49%HF dip, leaving the Si surface regions hydrogen terminated, native oxide free, and hydrophobic. Any small drops of the HF solution that were present on the sample surface after the HF dip were removed using compressed nitrogen. (Note: In order to maintain a hydrogen terminated Si surface and to avoid the formation of a SiO_2 layer, the samples were not rinsed in deionized water after the HF dip.)

Immediately after the HF dip, samples were placed flat top Si side up onto a quartz carrier which was introduced into the UHV furnace loadlock within 1 minute of the HF dip. Within 7 minutes of the HF dip, the loadlock reached a pressure of $1.5x10^{-6}$ torr and the sample was introduced into the UHV furnace chamber using a vacuum-sealed magnetically-coupled quartz rod such that the sample was in the middle zone of the three zone furnace. In all experiments, all three furnace zones were held at the desired annealing temperature between 750-800C at all times. The maximum pressure achieved

in the UHV furnace chamber during sample transfer was $2.0x10^{-7}$ torr. After sample transfer, the chamber pressure fell below $1.0x10^{-7}$ torr within 1 minute and below $5.0x10^{-8}$ torr within 3 minutes. Upon sample introduction, the middle furnace zone temperature always decreased to ~10C below the desired setpoint temperature as the quartz boat and sample were heated. The finite temperature-ramp-rate of the quartz boat and sample after introduction to the middle zone of the three zone furnace was accounted for by taking the anneal start time to occur when the middle furnace zone temperature climbed to within 5C of the furnace setpoint. The time between sample introduction and this "anneal start time" was always in the range of 3-5 minutes. In our annealing experiments, the middle furnace zone temperature always overshot the desired set point temperature by 5C, returning back to the set point temperature 13 minutes after the "anneal start time". At the end of the desired annealing time, the quartz boat and sample were removed from the furnace to the load lock using the vacuum-sealed magnetically-coupled quartz rod and placed into the $5x10^{-9}$ torr ambient of the room temperature load lock to cool. It should be noted that due to the finite ramp rate and temperature overshoot over the first 13 minutes of annealing, only annealing times greater than 15 minutes were considered in this study.

After annealing, samples were characterized using optical microscopy with a Zeiss Ultraphot optical microscope capable of 1000x magnification fitted with a digital camera, scanning electron microscopy with a 6320 JEOL 6320FV field emission high resolution scanning electron microscope, and atomic force microscopy with a Digital Instruments 3000 atomic force microscope.

SOI Defect Study

In order to evaluate the defect content of the ultra-thin single crystal SOI films studied in this work, we also performed a defect study on bonded SOI samples with 5nm, 10nm, 15nm, 20nm, 35nm thicknesses and the SiMOX SOI sample with 20nm thickness using defect-revealing wet etching techniques. The top Si layer pinhole density was determined using a 1 min 49% HF defect etch. In this etch, the HF solution penetrates any pinholes in the top Si film and etches circular holes in the underlying SiO_2 layer which are easily visible and countable via optical microscopy. The dislocation/stacking fault density in the top Si SOI layers were determined using a modified Secco etch.[86] Due to the extremely thin layers used in this study, a dilute Secco etch had to be used to minimize the Si etch rate in undefected film regions to allow for defect etch contrast. The dilute solution used consisted of 0.15M $K_2Cr_2O_7$:49% HF: DI H_2O (1:2:6). The Secco etch pit density was then measured using optical microscopy.

Dielectric SOI Edge Coverage Stabilization Structure

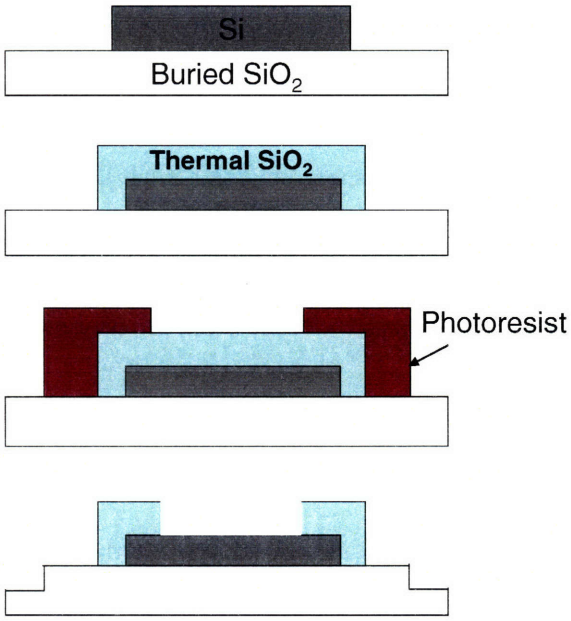

Figure 5.3: Schematic illustration of the process and structure used to demonstrate dielectric layer edge-coverage stabilization of Si SOI mesas against dewetting.

In order to demonstrate the stabilization of patterned SOI structures against dewetting using a dielectric edge-coverage stabilization technique, a 40mm square 50.0nm thick bonded SOI sample with the plasma-etched patterned Si SOI mesa structure illustrated in Figure 5.1 was exposed to dry thermal oxidation under 760torr of O_2 at 1000C for 100min. This resulted in the growth of 75nm of SiO_2, consuming the initial 50.0nm Si layer to the point that it was 14.8nm thick after oxidation, as measured by spectroscopy ellipsometry. Photolithography was then used to cover the edges of the square and circular oxidized Si mesas with photoresist stripes having edge overlap distances of 2, 5, and 10μm. The uncovered SiO_2 regions were then etched using a 2 min 7:1 BOE HF etch. Figure 5.3 illustrates this process and the final dielectric layer SOI mesa-edge-coverage structure.

Chapter 6
SOI Dewetting Study – Experimental Results and Discussion

In this chapter, we present the results of a UHV annealing study of dewetting in ultra-thin SOI films and interpret the results in terms of our isotropic 5-step capillary dewetting model presented in Chapter 4. We find that dewetting kinetics in this anisotropic dewetting system obey the scaling laws predicted by our isotropic model. However, the highly anisotropic geometries observed in SOI dewetting require detailed consideration of the anisotropic Si surface energy. In this chapter, we also extend our isotropic dewetting model to account for these anisotropic effects as well.

We begin by describing key general observations from our SOI dewetting study and then present and discuss our results in the context of the surface-energy-driven dewetting model presented in Chapter 4, focusing in turn on dewetting initiation in initially continuous flat film regions, edge thickening and retraction at straight patterned film edges, thickened edge breakdown, and dewetting propagation via void finger formation and propagation.

I. Key General Observations of SOI Dewetting

Consistent with the surface-energy-driven dewetting model presented in Chapter 4, in our SOI dewetting study we have clearly observed dewetting initiation at patterned film edges and have observed film edges to go through each of the distinct dewetting

phases discussed in the model: 1.) film edge retraction via continuous uniform edge thickening, 2.) thickened edge breakdown, and 3.) dewetting front propagation via void finger formation and propagation.

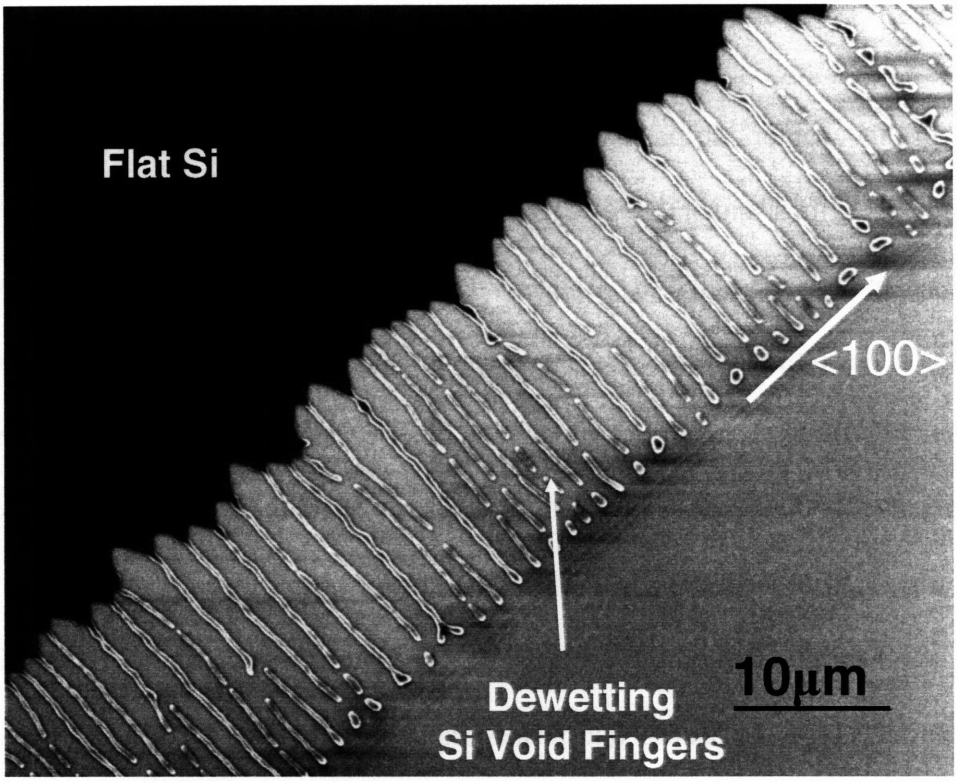

Figure 6.1: SEM image showing the uniform edge breakdown and void finger front propagation that is observed in films ≤ 20nm thick for in-plane mesa-edge orientations at or near <100>. This image is from a <100>-oriented mesa edge in a 20nm-thick SOI film UHV annealed at 750C for 4150min.

The rate and geometry with which the edge breakdown process proceeds has been observed to be critically dependent upon the SOI film thickness and the in-plane SOI mesa edge orientation.

A. Effect of Film Thickness on General SOI Dewetting Observations

As illustrated in Figure 6.1, in films with top Si thickness ≤ 20nm, mesa edges at or near <100> in-plane edge orientations are found to break down most rapidly and

uniformly and exhibit dewetting by the formation and growth of an equally-spaced parallel array of void fingers oriented preferentially in in-plane <100> directions. Since edge breakdown occurs uniformly in these mesa edges, the dewetting propagation distance of void fingers in these mesas is highly uniform and thus defines a uniform dewetting propagation front. This dewetting behavior, in which the film mesa edge breaks down uniformly and simultaneously along the length of the whole edge, allows readily for the extraction of meaningful kinetic parameters from <100>-edge-oriented mesas in SOI films with Si thickness $\leq$ 20nm, such as the edge breakdown wavelength and the dewetting propagation distance, as described below.

However, in annealed SOI films with top Si thickness $\geq$ 35nm, even mesas with edge orientations at or near the <100> in-plane orientation, the orientation observed to most readily undergo uniform edge breakdown, exhibit very different behavior in which the thickening retracting mesa edge breaks down locally as opposed to uniformly. In these thicker films, upon sufficient annealing, edge breakdown occurs only at discrete mesa-edge locations and void finger formation and growth occurs only at these locations, with void fingers radiating from these local edge breakdown sources into the surrounding flat thin film region, as shown in Figures 6.2 and 6.3. This local and erratic mesa-edge breakdown behavior in thicker SOI samples makes the extraction of meaningful kinetic parameters difficult or impossible, as it does not allow for meaningful measurements or comparisons of edge breakdown wavelengths or dewetting propagation distances from sample to sample.

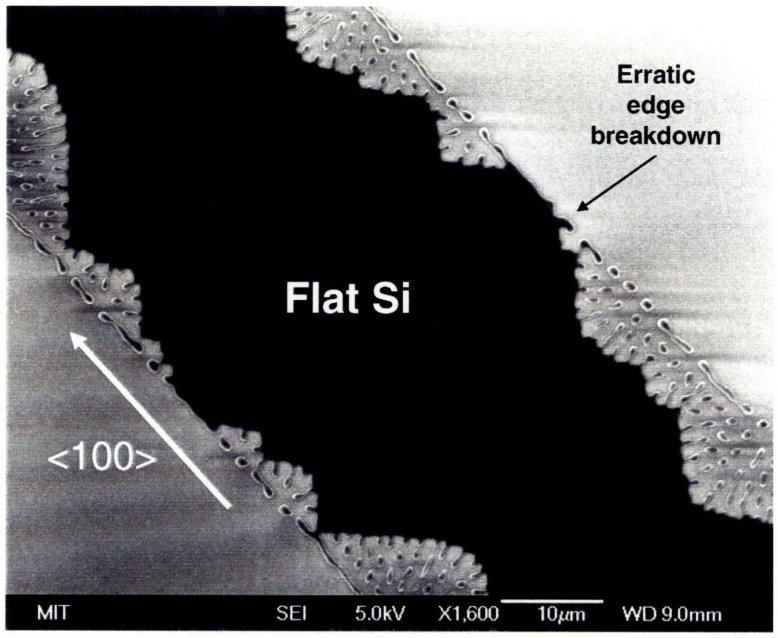

Figure 6.2: SEM image of the local and erratic edge breakdown observed in UHV annealed SOI films with thickness ≥ 35nm. This image is of a <100> in-plane-oriented mesa in a 35nm SOI film annealed at 800C for 2634min.

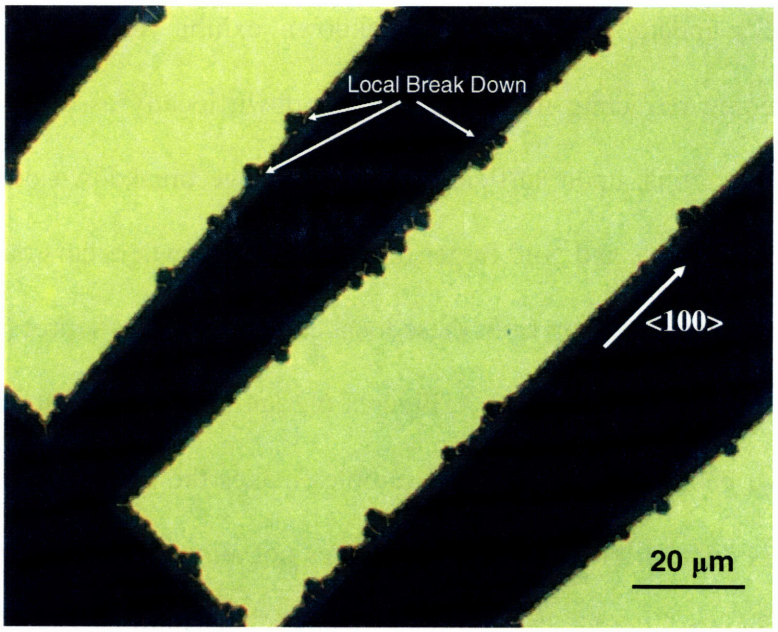

Figure 6.3: Optical micrograph of the local and erratic edge breakdown observed in UHV annealed SOI mesas in films with thickness ≥ 35nm, showing an earlier stage of breakdown than in Figure 6.2. The middle mesa in the image is a <100> in-plane-oriented mesa in a 35nm SOI film annealed at 750C for 4500min. Similar behavior is seen in the neighboring mesas with edge orientations off of <100> by 5° on either side.

We believe that this important qualitative difference between the edge breakdown behavior of thinner (≤ 20nm) and thicker (≥ 35nm) films is due to two distinct effects: 1.) the much greater stability of thicker films to uniform Rayleigh edge breakdown due to the h_{Si}^4 dependence of the thickened edge Rayleigh instability breakdown time (as seen from Equation 4.26) and 2.) the significant edge roughness introduced by the aggressive Si plasma etch used in this study (illustrated in Figure 5.1). The dependence of the thickened edge Rayleigh instability breakdown time on the fourth power of the Si thickness causes the uniform Rayleigh breakdown time for a 35nm film to be predicted to be approximately a factor of 10 greater than that for a 20nm film at any given temperature. We propose that this much longer predicted uniform Rayleigh breakdown time in films ≥ 35nm causes edge breakdown in these thicker films to initiate first at heterogeneous edge sites, such as locations with particular severe edge roughness, before uniform Rayleigh edge breakdown is able to proceed.

We also believe that the observed clear local edge breakdown and local formation and radiation of void fingers from these edge breakdown locations is further enhanced by the fact that the ratio of the void finger propagation rate (Equation 4.27) to the edge break down rate (Equation 4.26), scales with the Si film thickness.

$$\frac{v_{void-finger}}{t_{edge-breakdown}^{-1}} \propto h_{Si} \tag{6.1}$$

This relationship causes the ratio of the void propagation rate to the edge breakdown rate to be larger in thicker films than in thinner films, causing voids fingers to readily grow from local heterogeneous edge breakdown locations in thicker films. In thinner films, the relatively slower void finger propagation rate relative to the edge breakdown rate should result in less prominent punch-through of void fingers at any edge regions where local

edge breakdown might occur, making the formation of a uniform void finger propagation front more favored.

B. Effect of In-Plane Mesa Orientation on General SOI Dewetting Observations

In addition to the dramatic effect the film thickness has been observed to have on the basic nature of dewetting edge breakdown and void finger formation and growth in SOI mesas, we have also observed an analogous effect in mesas as a function of in-plane mesa-edge orientation, as shown in Figure 6.4. In SOI films ≤ 20nm thick, mesas with edges oriented at or near <100> in-plane orientations are consistently found to break down uniformly and simultaneously along their whole length, as shown in Figures 6.1, 6.4(a), and 6.4(b). However, mesas with edges oriented at or near <110> in-plane orientations are observed to be much more stable against breakdown and void finger formation, with edge breakdown observed to occur locally and erratically with time, if at all, with void fingers forming at and radiating from these edge breakdown locations, as illustrated in Figures 6.4(c), 6.4(d), and 6.5. Similar to what has been observed in SOI films ≥ 35nm, we believe that the local heterogeneous edge breakdown observed in mesas with edge orientations near <110> in-plane orientations in films ≤ 20nm thick is caused by an enhanced stability against uniform Rayleigh edge breakdown, in this case due to the formation of stable (111) and (311) facets at the thickening retracting mesa edge as discussed below, and the presence of severe local edge roughness due to the aggressive plasma Si etch used in this work.

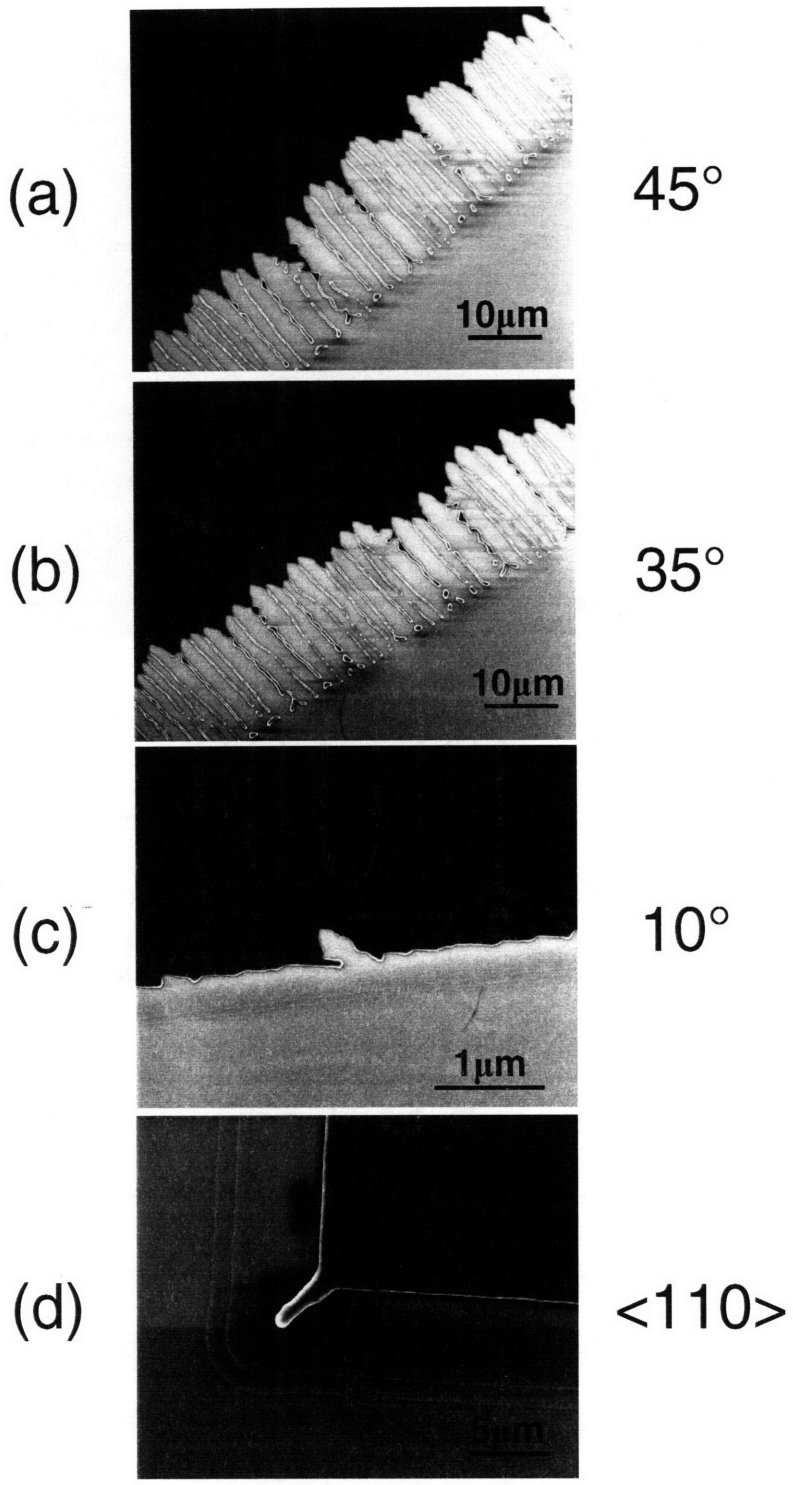

Figure 6.4: SEM images of UHV annealed SOI mesas having various edge orientations. The uniform and rapid breakdown of edges at and near <100> in-plane orientations and the enhanced stability of mesa edges at or near <110> in-plane orientations are evident. a.) <100> edge-oriented mesa; b.) mesa oriented near <100>, 35° from <110>; c.) mesa oriented 10° from <110>, local breakdown and void finger formation is seen; and d.) <110>-oriented mesa – complete stability against break down is observed. 20nm-thick SOI sample annealed at 750C for 4150min.

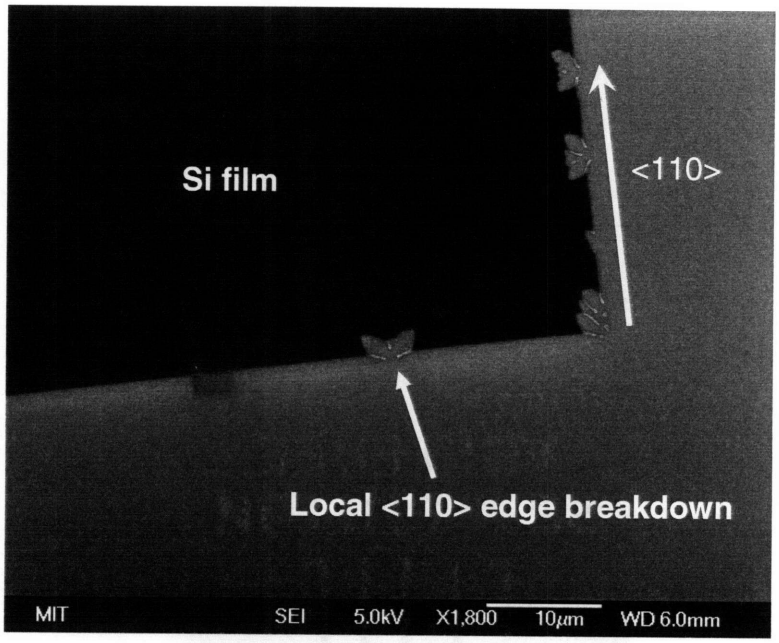

Figure 6.5: SEM image of a <110> edge-oriented SOI mesa showing local edge breakdown, presumably caused by a locally severe point of edge roughness. 10nm-thick SOI sample annealed at 800C for 45min

Figure 6.6 highlights the difference in dewetting behavior observed for various in-plane mesa-edge orientations. Due to this anisotropic dewetting behavior, in a single annealed sample, mesa edges with different edge-orientations can be found to be undergoing each of the three distinct phases of dewetting. Figure 6.6(a) shows a <110>-oriented mesa edge in the edge thickening and retraction phase, Figure 6.6(b) shows a mesa oriented 10° off <110> undergoing uniform Rayleigh edge break down, and Figure 6.6(c) shows a <100>-oriented mesa edge well into the void finger propagation stage.

This anisotropic dewetting behavior can be understood in terms of the anisotropic surface energy of Si, as discussed in Appendix A. During uniform edge thickening and retraction, <110>-oriented mesa edges can readily facet on the low energy (111) and (311) planes while maintaining a straight edge and thus are very stable against breakdown. (100)-oriented mesa edges can easily facet laterally on (111) planes during edge break down and thus breakdown occurs readily in these edges.

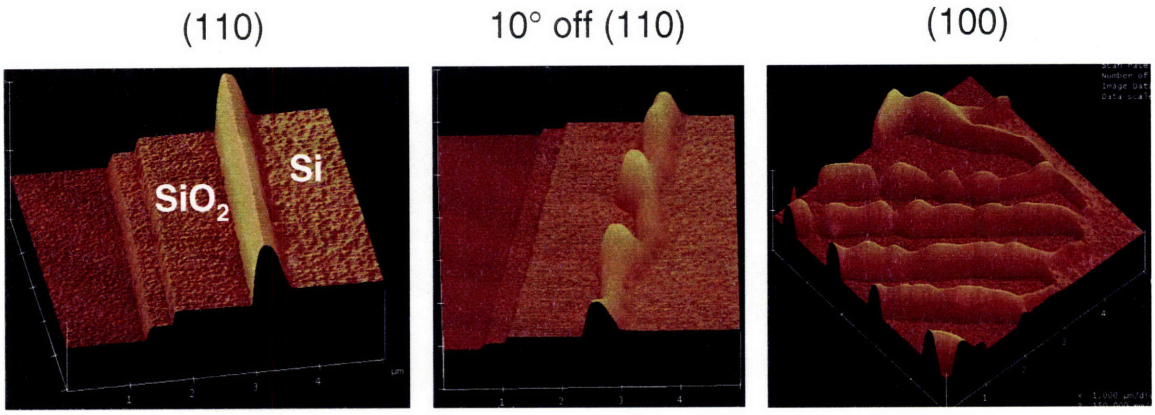

Figure 6.6: AFM images illustrating the diversity of dewetting behavior observed for different mesa-edge orientations in a single UHV annealed SOI sample. a.) <110>-oriented edge undergoing uniform edge thickening and retraction, b.) 10° off <110>-oriented mesa undergoing uniform edge breakdown, and c.) <100>-oriented mesa undergoing continuous void finger propagation after edge breakdown. 20nm-thick SOI film annealed at 750C for 4150min.

Figures 6.7 and 6.8 highlight another important observation of anisotropic behavior in our dewetting experiments that void fingers clearly form and propagate preferentially in <100> in-plane directions. Figure 6.7 shows that the preferential void finger propagation in <100> directions is independent of the initial SOI mesa edge orientation. Measurements of the orientations of greater than 200 void fingers in each UHV annealed sample in this study have shown that the average void finger direction in all mesas falls within 0.5° of <100>, confirming quantitatively what is evident visually from Figures 6.1, 6.7, and 6.8.

Figure 6.7 also illustrates that with the exception of <110>-oriented edges, void fingers grow in a single <100> direction, the <100> direction that is closest to being perpendicular to the edge. Figure 6.8 illustrates this effect at the corner of a <100>-oriented mesa.

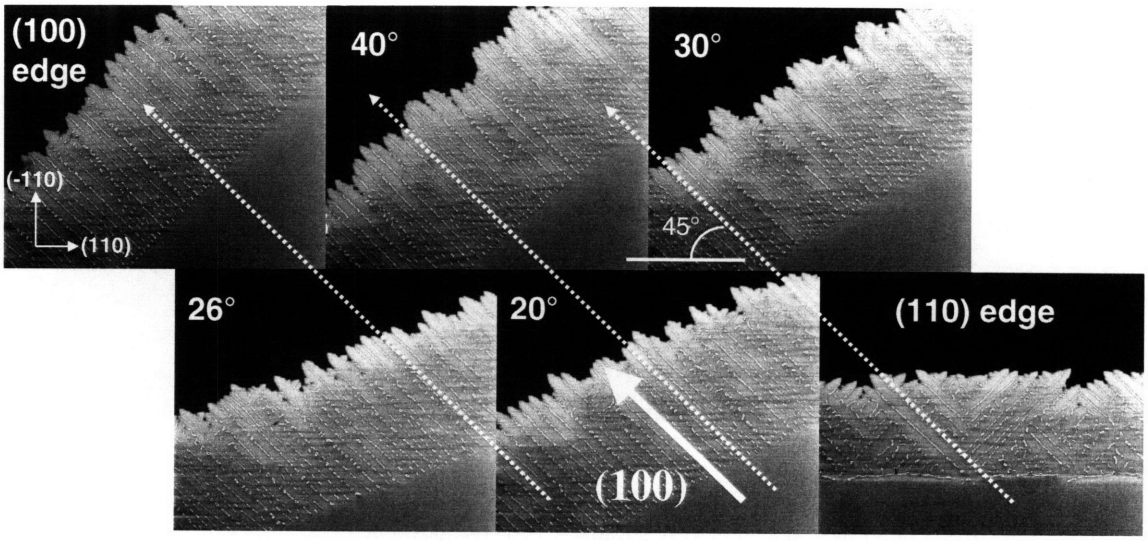

Figure 6.7: SEM images from a 10nm-thick SOI film annealed at 750C for 1325min illustrating the formation and growth of void fingers preferentially in the <100> in-plane direction, regardless of mesa edge orientation.

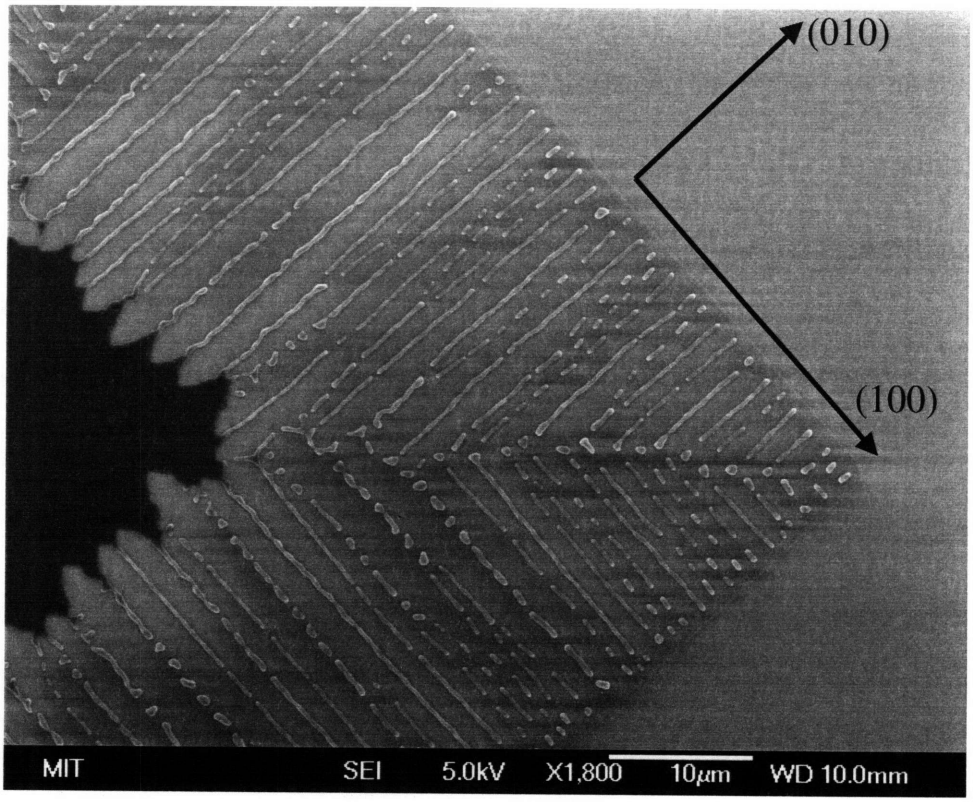

Figure 6.8: SEM image illustrating formation of void fingers in the <100> in-plane directions that are closest to perpendicular to the initial mesa edge orientation. 15nm-thick SOI film annealed at 750C for 3375min.

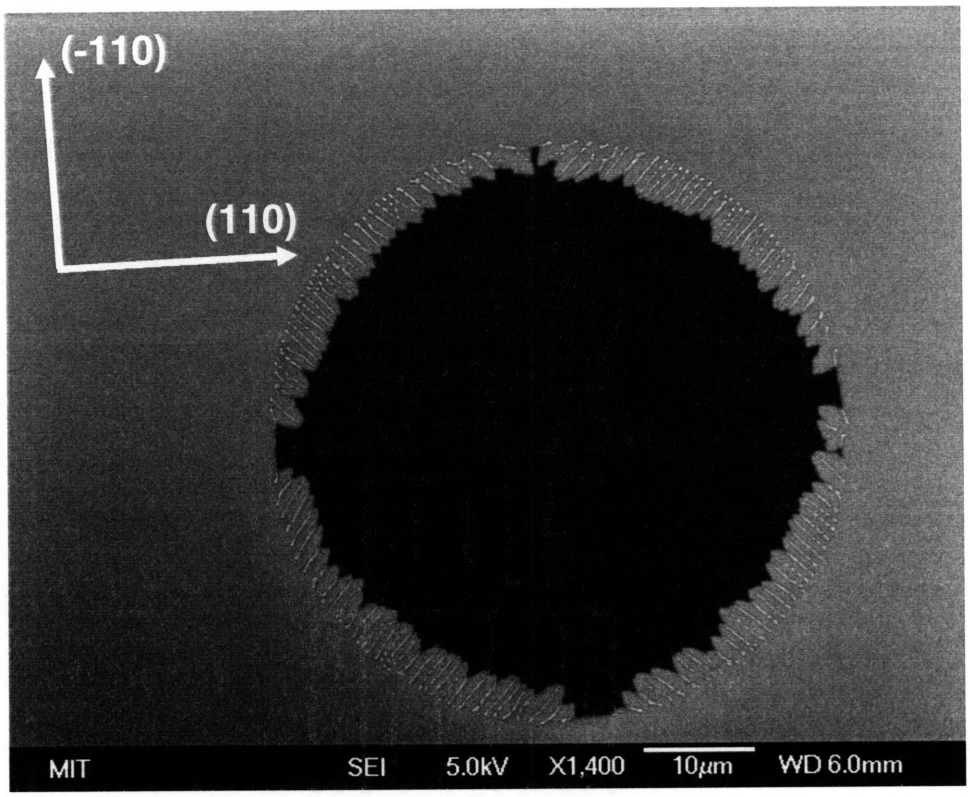

Figure 6.9: SEM image of dewetting at the edges of a circular SOI mesa illustrating the enhanced stability of <110>-oriented edges against breakdown and the preferential formation and growth of void fingers in <100> directions regardless of initial edge orientation. 10nm-thick SOI film annealed at 800C for 45min.

Observation of dewetting in a circular SOI mesa allows for the simultaneous observation of dewetting behavior at all in-plane edge orientations. The enhanced stability of <110>-oriented edges against breakdown and the preferential formation and growth of void fingers in <100> directions after edge breakdown, regardless of the initial edge orientation, are evident in the SEM image of dewetting in a circular mesa shown in Figure 6.9.

II. SOI Dewetting Results and Interpretation in Terms of Surface-Energy-Driven Dewetting Mechanism

We now present and discuss our experimental results in terms of the sequential phases of dewetting described in the surface-energy-driven model presented in Chapter 4.

A. Dewetting Initiation in Initially Continuous Flat SOI Film Regions

In order to understand the relationship between the defect content of ultra-thin SOI films and dewetting initiation in initially flat continuous SOI film regions, we performed a full defect study of our ultra-thin SOI sample set along with our UHV SOI annealing study.

The defect contents of bonded and SiMOX films were observed to be quite similar. HF defect (pre-existing film void) densities were determined to be very low in all films studied: 0.17-1.0 cm^{-2} and 0.16-0.84 cm^{-2} for the bonded films and SiMOX film, respectively.

A Secco defect study was also performed on these SOI samples. Due to the extremely thin SOI layers studied here (5-35nm), a modified dilute Secco etch was used to minimize the etch rate of the undefected Si regions to allow for defect etch contrast, as discussed in Chapter 5. Etch tests were performed on 15nm, 20nm, and 35nm bonded samples and the 20nm SIMOX sample studied in this work. Secco defect-to-film etch selectivity was insufficient to observe defects in the 15nm films, but repeatable results were obtained for the 20nm and 35nm films. Defect counts were found to be consistent within a factor of 2 for both different thicknesses and HF etch times, a saturation in the

defect count with etch time indicating that all defects present were revealed. Secco defect densities were found to be 900-4000 cm^{-2} and 700-1000 cm^{-2} for the 20nm and 35nm bonded samples and the 20nm SiMOX sample, respectively.

In our dewetting studies of 5-35nm SOI films annealed at 750-800C for 15-4500min, we did observe dewetting initiation to occur in initially flat continuous SOI film regions. However, in all cases, we observed dewetting initiation to always occur with a density of < 300 cm^{-2}. Furthermore, as shown in Figure 6.10, in all cases where dewetting initiation sites in initially flat continuous film regions were examined via SEM, process-induced surface particles were found to be the heterogeneous cause of dewetting initiation.

The observation of densities of dewetting initiation in initially flat continuous SOI film regions well below the measured stacking fault/dislocation densities measured in our SOI films using the Secco etch technique strongly indicates that stacking faults and dislocations do not serve as void nucleation sites in flat continuous SOI film regions. Furthermore, the observation of clearly extrinsically introduced surface particles at all dewetting initiation sites observed in flat continuous SOI film regions, provides strong evidence that flat continuous regions in SOI films are inherently highly metastable against dewetting and that intrinsic defects present in SOI films, such as stacking faults and dislocations, do not provide heterogeneous pathways for critical void nucleation in SOI films.

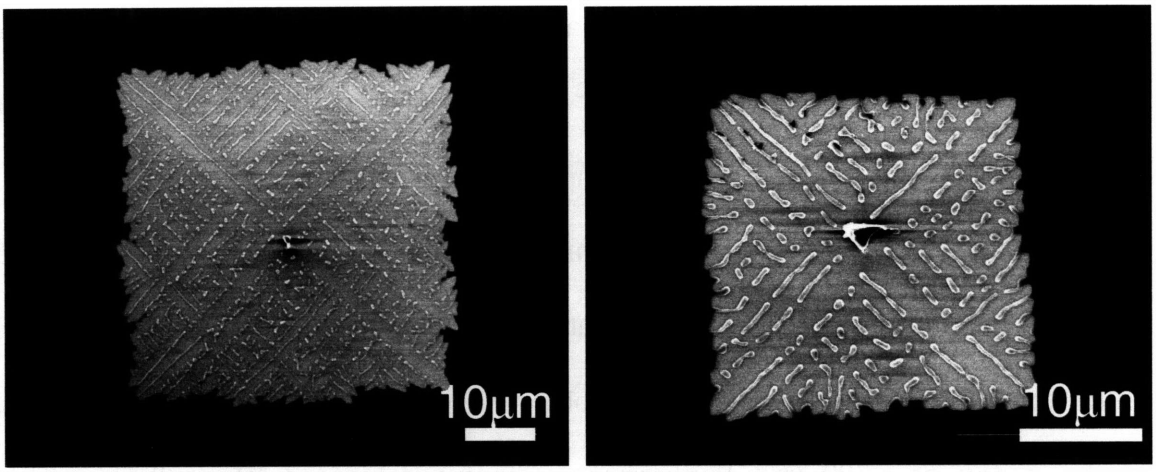

Figure 6.10: SEM images of observed dewetting initiation locations in initially flat continuous SOI film regions after UHV annealing. In all cases where dewetting initiation sites in flat SOI film regions were inspected with SEM, extrinsically introduced surface particles were responsible for initiation. Left: 10nm-thick SOI film annealed at 750C for 1325min, Right: 20nm-thick SOI film annealed at 750C for 2821min.

B. Kinetics of Edge Thickening and Retraction

Figure 6.11 shows a <110>-oriented edge that has undergone uniform edge thickening and retraction during UHV annealing. As shown in Figure 6.12, thickening retracting <110>-oriented edges have been found to be bounded by stable (111) and (311) Si facets, as explained in Appendix A. The ability of <110>-edges to form these stable edge facets explains the uniquely high stability of these edges against edge breakdown. This enhanced stability of <110> in-plane-oriented mesas against breakdown has allowed us to perform a quantitative study of the kinetics of the edge thickening and retraction dewetting process for the first time in SOI. In fact, we are not aware of any existing literature reporting on the kinetics of uniform film edge thickening and retraction from patterned dewetting thin film edges anywhere in the existing dewetting literature. As shown in Figure 6.13, the edge retraction distance was easily extracted from SEM images of uniformly thickening retracting <110>-oriented mesa edges.

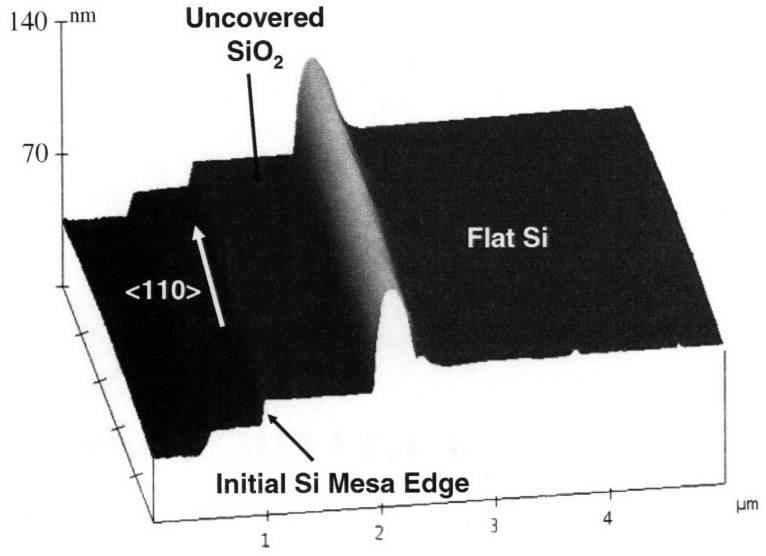

Figure 6.11: Birds-eye view AFM image of a <110>-oriented SOI mesa undergoing uniform edge thickening and retraction. 15nm SOI sample UHV annealed at 800C for 180min.

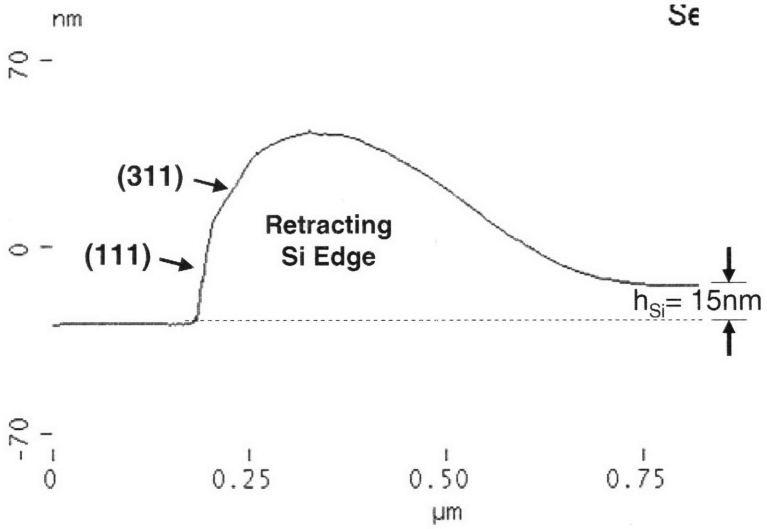

Figure 6.12: AFM cross-sectional profile perpendicular to the <110>-oriented thickening retracting edge shown in Figure 6.11. The presence of stable (111) and (311) Si facets in the edge is evident from the profile, explaining the enhanced stability of <110>-oriented SOI edges against Rayleigh breakdown.

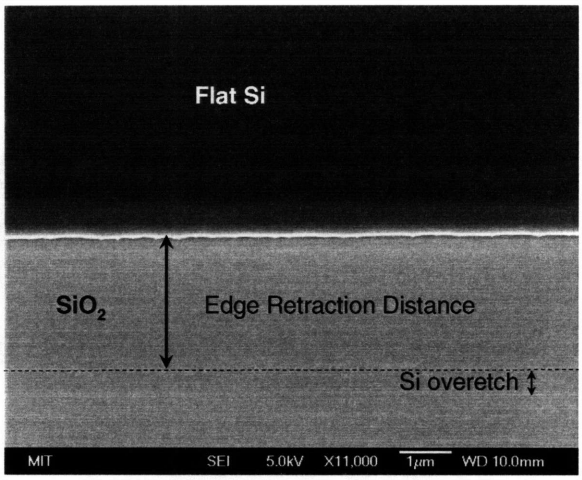

Figure 6.13: Plan-view SEM image showing a top down view of a thickening retracting dewetting <110>-oriented film edge and the measured edge retraction distance from the initial edge position (dotted line) and the final edge position after annealing. (Note the Si layer overetch.) <110>-oriented mesa edge in 15nm SOI sample UHV annealed at 800C for 180min.

For each annealed sample in which uniform edge thickening and retraction was observed at <110>-oriented mesa edges, at least 15 edge retraction distance values from 5 different mesa-edge locations were measured and averaged. The average edge retraction distances are plotted versus time for 750C and 800C annealing temperatures in Figures 6.14 and 6.15, respectively.

From the expression we derived for the edge retraction distance at a straight film edge in Chapter 4 (Equation 4.23), we expect the edge distance to increase with the square root of time ($t^{0.5}$), as opposed to the $t^{0.4}$ dependence predicted for a circular void by Brandon and Bradshaw.

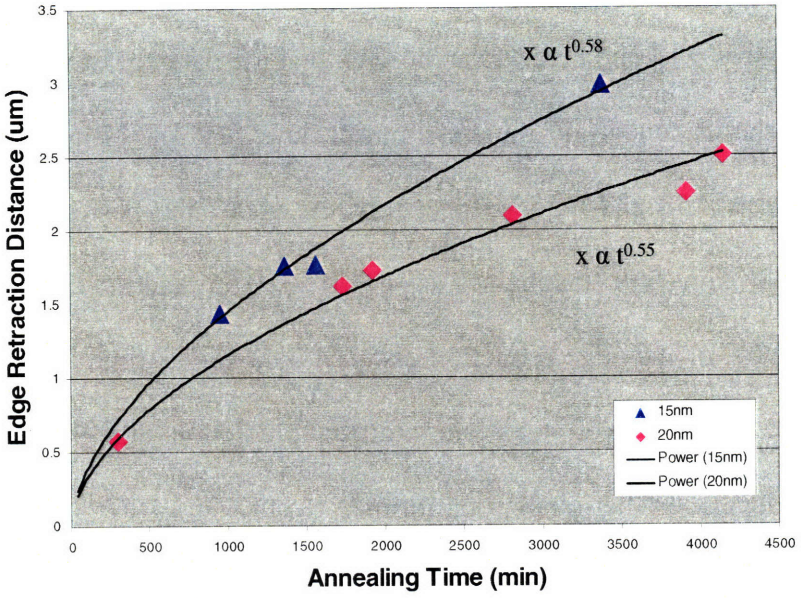

Figure 6.14: Plot of the edge retraction distance at <110>-oriented mesa edges versus annealing time for various SOI samples annealed at 750C. The data are well fit by a power law with n=0.58 and 0.55 for 15nm and 20nm SOI films, respectively.

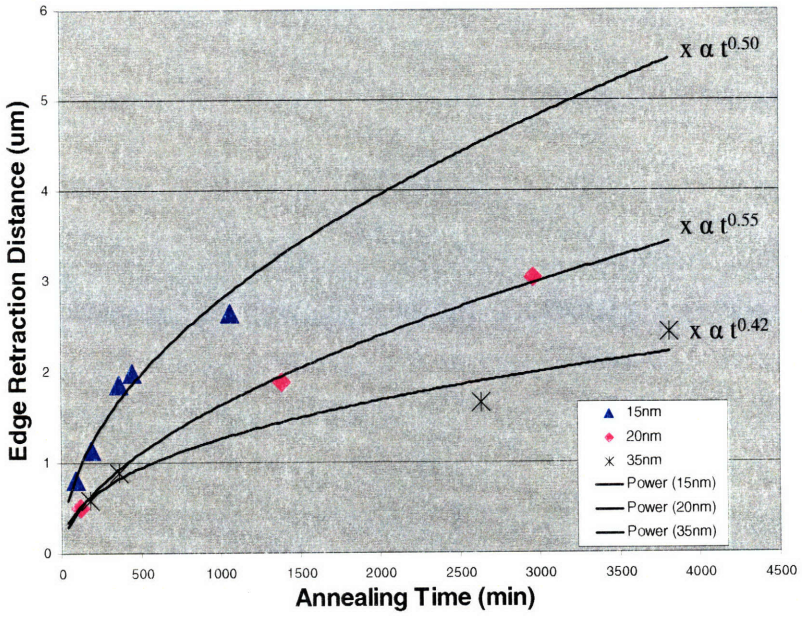

Figure 6.15: Plot of the edge retraction distance at <110>-oriented mesa edges versus time for various SOI samples annealed at 800C. The data are well fit by a power law with n=0.50, 0.55, and 0.42 for 15nm, 20nm, and 35nm SOI films, respectively.

From Figures 6.14 and 6.15, it can be seen that the data are fit well by power law fits. At 750C, the exponent of the best power law fits for 15nm and 20nm SOI thicknesses are n = 0.58 and 0.55, respectively. At 800C, the best power law fits for 15nm, 20nm, and 35nm SOI thicknesses are n = 0.50, 0.55, and 0.42, respectively. The good power law fits of the edge retraction distance data versus time and the range of n values of 0.42-0.58 agree well with our model's prediction that the edge retraction distance should depend on the square root of time.

In order to further evaluate the validity of our model for the edge thickening and retraction kinetics of dewetting at a straight SOI film edge, we have plotted the edge retraction distance-film thickness product against time on a log-log plot for all of our edge retraction distance data in Figure 6.16. In Chapter 4, we derived the following relation for the edge retraction distance

$$r_{edge} = \sqrt{\frac{D_s \gamma \Omega^2 \nu}{2kT}} \frac{1}{h_{Si}} \sqrt{t} \,. \tag{6.2}$$

which yields the following relationship for the edge retraction distance-film thickness product

$$r_{edge} h_{Si} = \sqrt{\frac{D_s \gamma \Omega^2 \nu}{2kT}} \sqrt{t} \tag{6.3}$$

As shown in Figure 6.16, a log-log plot of the edge retraction distance-film thickness product versus time has a good linear fit and gives n = 0.49 and 0.55 for 800C and 750C, respectively. The observed good linear fit and extraction of n values very close to the 0.5 value predicted by our model lend strong support to the validity of the dewetting edge retraction model we developed in Chapter 4. It is of note that although top Si SOI films

have anisotropic surface energies and exhibit clear anisotropic behavior, the edge thickening and retraction process observed at <110>-oriented mesas in these films still obeys the scaling laws predicted by our isotropic dewetting model.

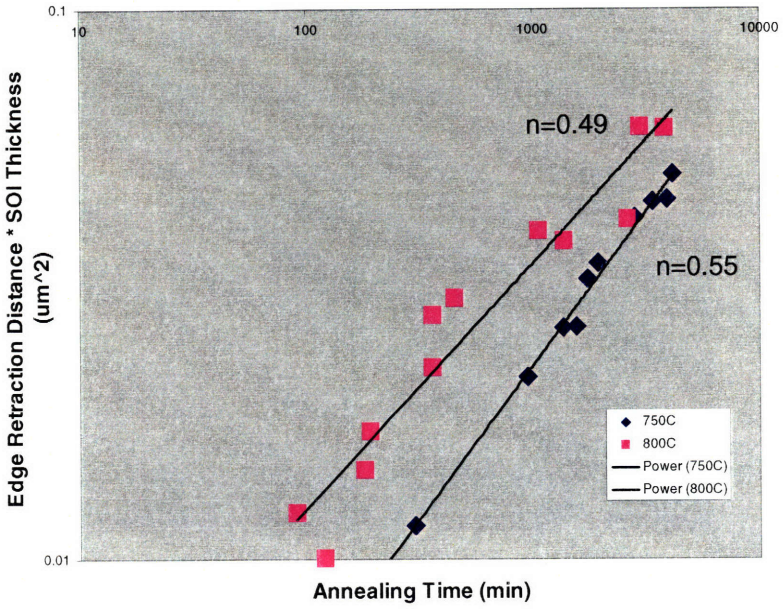

Figure 6.16: Log-log plot of the edge retraction distance-SOI thickness product versus annealing time. The reasonably good linear fit and n values close to 0.5 lend strong support to the validity of our model for dewetting edge retraction at a straight thin film edge.

C. Thickened Dewetting Edge Breakdown

Under our surface-energy-driven dewetting model, it is the edge breakdown process that initiates void finger formation and propagation and determines the spacing of void fingers. Our edge breakdown model, based on a generalized Rayleigh instability in the uniformly thickened retracting dewetting film edge, predicts that the edge should breakdown with a highly characteristic and uniform wavelength that is proportional to the film thickness, as shown in Equations 4.24 and 4.25.

We have clearly observed the thickened edge breakdown process in the early stages of dewetting at SOI film edges in our study, as shown in Figure 6.17. In order to study the edge breakdown process, we measured the average spacing between edge

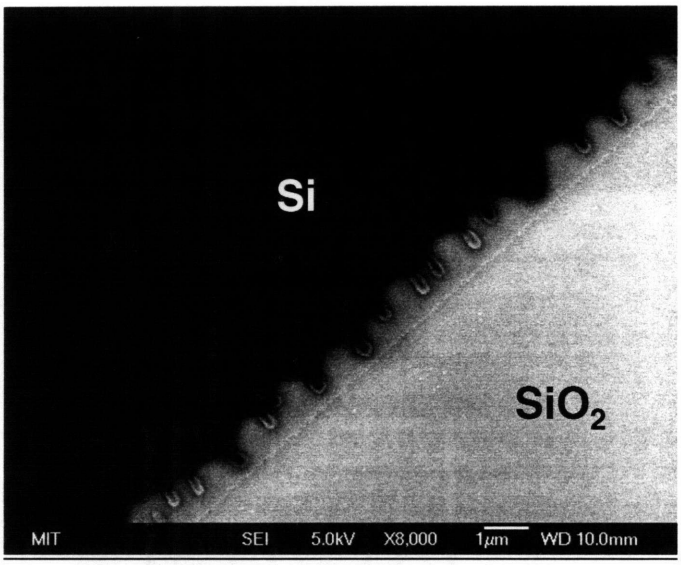

Figure 6.17: SEM image of a <100>-oriented edge that has just undergone edge breakdown in a 10nm-thick SOI film UHV annealed at 750C for 100min.

islands at the edges of <100>-oriented SOI mesas in all of our samples. The average edge island spacing results are plotted in Figure 6.18 versus SOI thickness. Although there is scatter in the data, we do observe a general trend of a monotonic increase in the edge island spacing with increasing SOI film thickness. Furthermore, we find that the prediction for edge breakdown wavelength for SOI, assuming isotropic energies and a contact angle of 73°, from the model of Kan and Wong upon which we base our theory for thickened dewetting edge breakdown, has reasonably good agreement with the experimental data for edge breakdown in <100>-oriented SOI mesas, as shown in Figure 6.18. We believe that the scatter in the data is likely due to random initial edge roughness pre-perturbations introduced by the relatively aggressive plasma Si etch that was used in this study.

The observed breakdown of thickened dewetting edges with a highly characteristic wavelength and the observation of the average edge breakdown wavelength in <100>-oriented mesa edges to be roughly proportional to the SOI film thickness indicates that our isotropic model for thickened edge breakdown provides an accurate description of the basic mechanism underlying edge breakdown in SOI films. However, as discussed below, the significant increases in thickened edge stability against breakdown and breakdown wavelength as the mesa-edge orientation moves away from <100> toward <110> requires the explicit consideration of anisotropic surface energy effects in SOI.

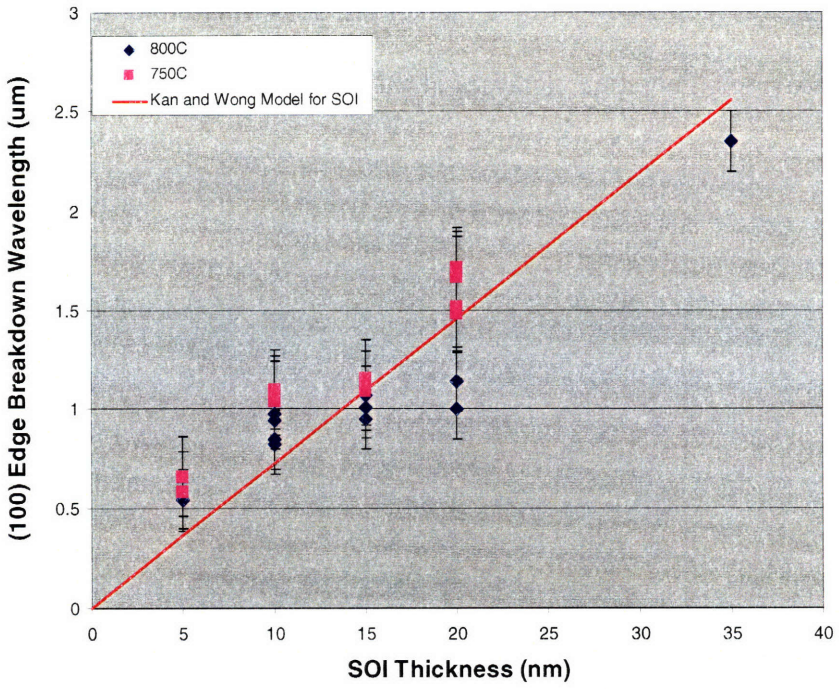

Figure 6.18: Plot of average edge breakdown wavelength in (100)-oriented mesa edges versus SOI thickness, with the line representing the relationship between edge breakdown wavelength and film thickness for SOI predicted by the edge breakdown model of Kan and Wong.

Extension of Edge Breakdown Model to Account for Surface Energy Anisotropy

As stated above, the edge breakdown wavelength has also been found to be dependent on the SOI mesa edge orientation, reflecting the underlying anisotropy in the surface energy of the top Si SOI film. As shown in Figure 6.19, the average edge breakdown wavelength is shortest in SOI mesas with <100>-oriented edges and monotonically increases as edge orientations approach the stable <110>-oriented edge, for which uniform edge breakdown is not observed and thus uniform edge breakdown wavelength extraction not impossible.

Although we do not have an explicit model to which we can fit this data, we can understand this behavior in terms of the effect of silicon's surface energy anisotropy on the Rayleigh instability breakdown of a thickening dewetting edge. Cahn[87] and Stolken and Glaeser[88] provided theoretical analyses of the effect of surface energy anisotropy on

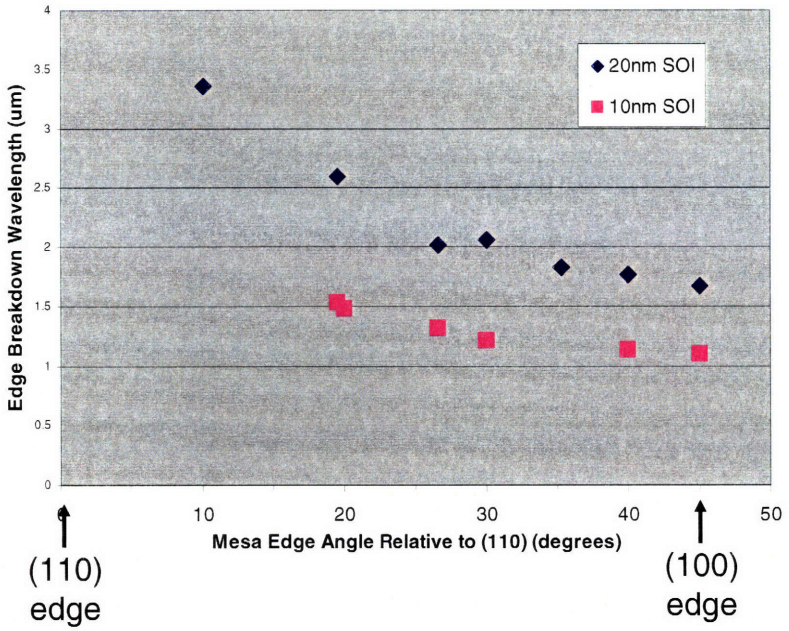

Figure 6.19: Plot of average measured edge breakdown wavelength versus SOI mesa edge orientation relative to the <110> orientation. <100>-oriented edges appear to have the minimum break down wavelength, with a monotonic increase in the break down wavelength as the edge orientation approaches the stable <110> orientation.

Rayleigh instability breakdown of a solid cylinder by surface-diffusion. Assuming that surface energy anisotropy only existed for plane orientations tilted along the axis of a cylinder, Cahn derived an expression for the Rayleigh instability wavelength given by[87]

$$\lambda_{anisotropic} = \lambda_{isotropic}\left[1+\frac{1}{\gamma_s}\left(\frac{\partial^2\gamma_s}{\partial\varphi^2}\right)\right]^{\frac{1}{2}}, \tag{6.4}$$

where $\lambda_{isotropic}$ is the wavelength predicted for the case of surface energy isotropy, γ_s is the surface energy at the initial cylinder surface orientation, φ is the angle from normal to the cylinder surface toward the cylinder axis, and $\frac{\partial^2\gamma_s}{\partial\varphi^2}$ is related to the curvature of the anisotropic surface energy plot at initial cylinder surface orientation for the material in question. Stable facet orientations represent minima in the surface energy versus orientation plot for a material. Thus, stable facets can typically have large positive values of $\frac{\partial^2\gamma_s}{\partial\varphi^2}$. Furthermore, Glaeser and Stolken determined that for this situation, the ratio of the characteristic evolution times for the anisotropic case to the isotropic case is given by[88]

$$\frac{t_{anisotropic}}{t_{isotropic}} = \left[1+\frac{1}{\gamma_s}\frac{\partial^2\gamma_s}{\partial\varphi^2}\right]. \tag{6.5}$$

Equations 6.4 and 6.5 help explain why thickened edges at <110>-oriented mesa edges in SOI are so resistant to breakdown by the thickened edge Rayleigh instability. The low energy Si (111) and (311) facets that are formed at straight <110>-oriented thickening retracting edges result in a large value of $\frac{\partial^2\gamma_s}{\partial\varphi^2}$ for this orientation and thus a long breakdown wavelength and evolution time are predicted. As patterned edge

orientations get further away from the stable <110> orientation, this factor gets smaller or even negative, resulting in much quicker thickened edge Rayleigh breakdown and shorter edge break down wavelengths, as observed in Figure 6.19.

It is of note that a monotonic increase of the edge breakdown wavelength is observed in going from <100> edge-orientations to <110> edge-orientations. As discussed in Appendix A, straight edge-orientations in <310> directions, which lie between <100> and <110>, can facet on the (311) planes that make large angle with the (100) plane and thus would be expected to exhibit relatively high stability and longer wavelengths relative to neighboring edge orientations if (311) planes are highly stable in SOI. The <310>-oriented mesa edges included in this study, however, did not exhibit any special stability. This would seem to indicate that the stability of the (111) plane dictates anisotropic behavior in our SOI dewetting experiments, as opposed to (311) planes, although (311) planes are indeed observed to be present at the most stable <110>-oriented mesa edges. This behavior is not entirely clear at present and will be a subject of future study.

Thus, we can see that the basic geometry and edge breakdown wavelength scaling with the SOI film thickness observed in thickened edge breakdown in our work indicates that SOI dewetting edge breakdown is generally well-described by our simple isotropic thickened edge Rayleigh breakdown model. However, the significant increase in the edge breakdown time and edge breakdown wavelength observed as mesa-edge orientation is varied from the most unstable <100> orientation to the most stable <110>-orientation in our (100)-oriented SOI films, can only be understood in terms of the anisotropic surface

energy of Si and can be interpreted in terms of the enhanced stability of thickened mesa edges that are bounded by stable Si facets against edge breakdown.

D. Kinetics of Dewetting Propagation via Void Finger Growth

Due to the highly uniform dewetting propagation fronts observed in <100>-oriented patterned edges in SOI, we focus our study of the kinetics of dewetting propagation via void finger propagatioin on <100> edge-oriented mesas. For each annealed sample, the average dewetting front propagation distance in <100>-oriented mesas was determined by extracting from SEM images the perpendicular distance from the initial etched edge to the void finger tip for > 200 void fingers per sample. Figure 6.20 illustrates the evolution of the dewetting front propagation distance with increased annealing time for a 20nm-thick bonded SOI film annealed at 750C for various times.

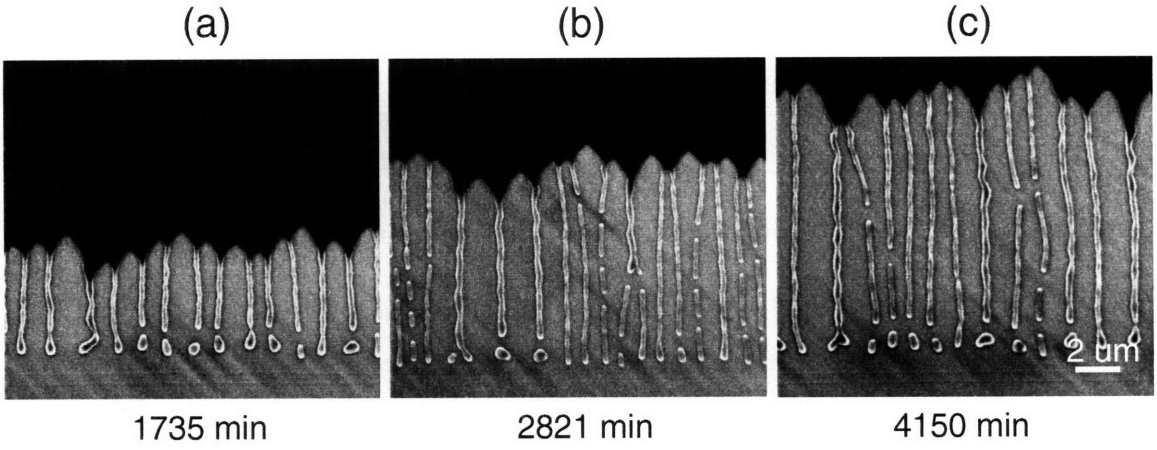

Figure 6.20: SEM micrographs illustrating the motion of the SOI dewetting propagation front with continued annealing in 20nm-thick SOI samples UHV annealed at 750C. The average dewetting front propagation distance was extracted from SEM micrographs, enabling the extraction of the dewetting front propagation velocity.

The extracted average void finger propagation distances for each sample, with error bars representing the standard deviation in the measurements, are plotted in Figures 6.21 and 6.22 for 800C and 750C annealing temperatures, respectively. The good linear fit with time of each SOI thickness/temperature edge propagation distance data set indicates that dewetting propagation occurs at a constant rate in time. Therefore, a constant propagation velocity value for each SOI thickness/temperature data set can be extracted from the slope of these linear fits, as shown in Figures 6.21 and 6.22.

To determine the thickness dependence of the dewetting front propagation velocity, we plot the dewetting front propagation velocity versus SOI thickness on a log-log plot in Figure 6.23. The good linear fit of this data indicates an inverse power law dependence of the dewetting propagation velocity, v_{dewet}, on SOI thickness

$$v_{dewet} \propto h_{Si}^{-n} \tag{6.6}$$

with n=3.0-3.2.

This result is in close agreement with the inverse power law thickness dependence with n=3 predicted by the isotropic Jiran and Thompson void finger propagation model discussed in Chapter 4. The close agreement of the propagation velocity thickness scaling observed in SOI dewetting indicates that the isotropic Jiran-Thompson model provides an accurate description of void finger propagation in dewetting. Perhaps more interestingly, the isotropic Jiran-Thompson model is able to predict the thickness dependence of dewetting in a thin film system with anisotropic surface energies for the first time, indicating the universality of this predicted scaling behavior.

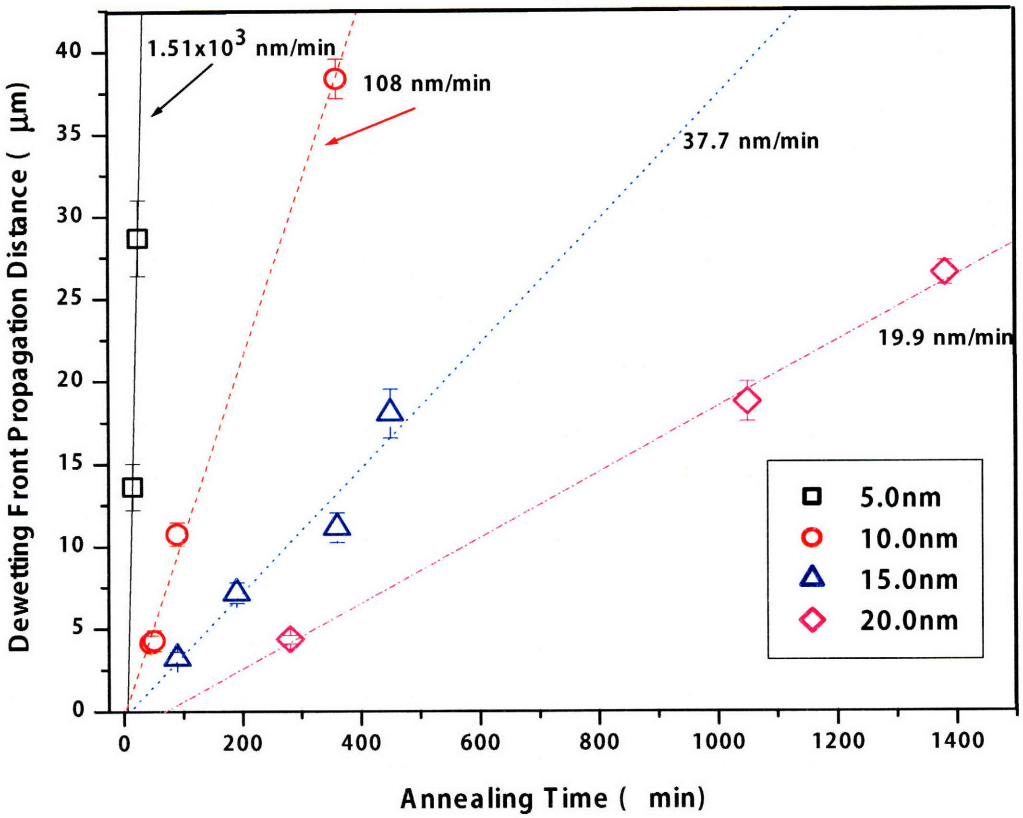

Figure 6.19: Plot of the average dewetting front propagation distance versus annealing time at <100>-oriented patterned film edges UHV annealed at 800C.

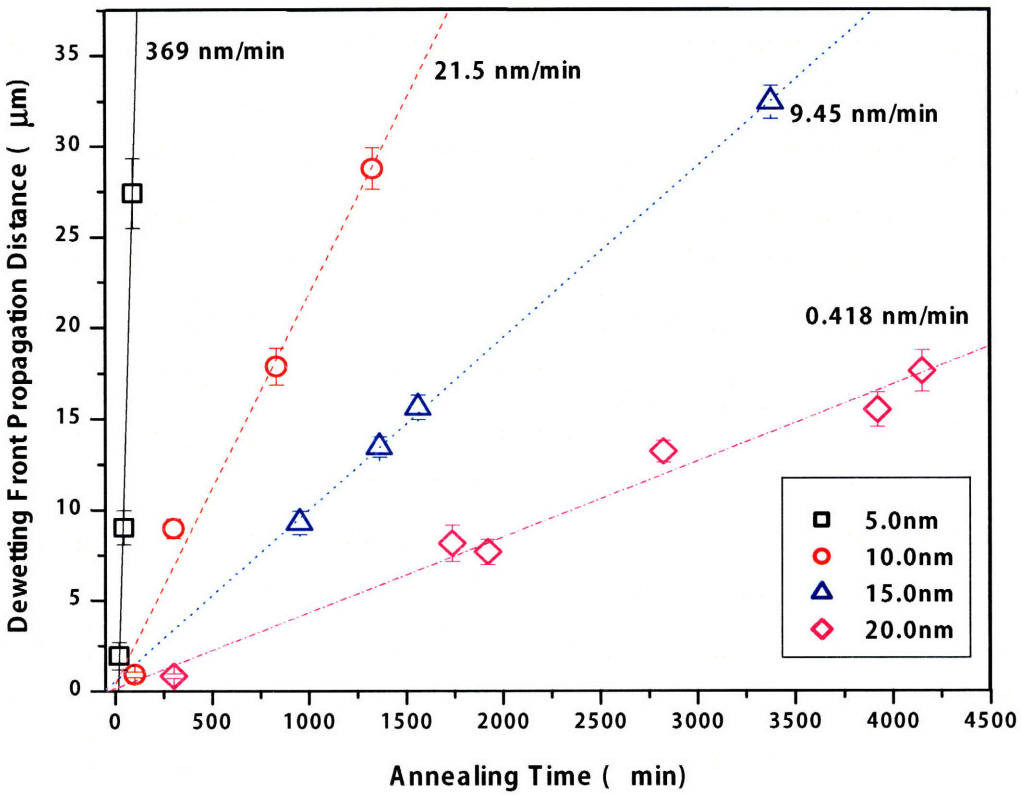

Figure 6.20: Plot of the average dewetting front propagation distance versus annealing time for <100> oriented patterned film edges UHV annealed at 750C.

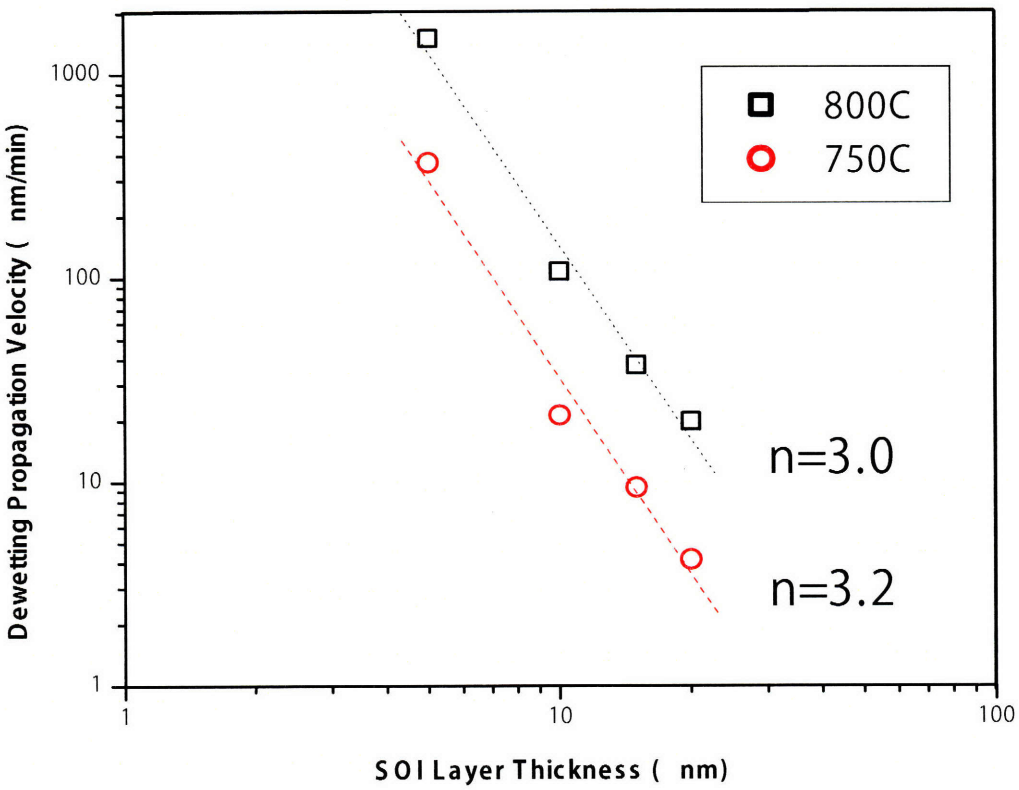

Figure 6.23: Plot of dewetting front propagation velocity versus SOI layer thickness indicating good inverse power law fits of the propagation velocity with SOI thickness with n=3.0 at 800C and n=3.2 at 750C.

In Figure 6.24, we plot the propagation velocity in an Arrhenius plot to estimate the activation energy of the velocity. From Figure 6.24, we extract activation energy values of 2.7eV, 3.1eV, 2.6eV, and 3.0eV for 5, 10, 15, and 20nm films, respectively. From these values, we estimate an activation energy for Si surface diffusion of 2.9±0.3eV in the 750-800C temperature range.

As discussed in detail below, the propagating SOI void finger tip edges in this study have been observed to facet on (111) and (311) planes. Thus, Si surface atoms diffusing away from the void tip toward the neighboring flat film region must diffuse along the (111) Si plane, transfer to the (311) plane, diffuse along the (311) plane,

transfer to the (100) plane, and subsequently diffuse along the (100) plane. The activation energy of the rate limiting step amongst these will determine the activation energy of the void finger propagation rate. However, of all of these surface transport processes, only surface diffusion on (100) and (111) Si surfaces has been studied in the literature in any detail.

Surface diffusion typically occurs via the diffusion of surface defects, such as adatoms or surface vacancies. The activation energy for morphological evolution via the surface diffusion of these defects Q_s is the sum of the defect formation energy Q_f and the defect migration energy barrier Q_m. Theoretical and experimental reports in the literature on (100) Si surfaces indicate an adatom formation energy of ~1.3eV[89] and an adatom migration energy of ~0.7-1.0eV[90-93], indicating a range of Q_s for surface diffusion on the (100) Si surface of ~2.0-2.3eV. Keeffe et al. studied the decay of the amplitude of an etched step grating in a (100) Si surface during UHV annealing and extracted an activation energy for (100) Si surface diffusion of 2.3±0.1eV, in reasonable agreement with the range stated above.[94] Theoretical and experimental studies of (111) Si surfaces have provide adatom Q_f values in the range of ~2.1-2.6eV[89,95,96] and Q_m values of 1.1-1.6eV,[95,97-100] yielding a Q_s range of 3.2-4.2eV. The higher adatom formation energy on (111) Si surfaces can be understood in terms of the lower number of dangling bonds present at the low energy closely packed (111) surface, which results in a surface adatom having a larger number of dangling bonds and thus a higher formation energy. No information is available for the other possible kinetic limiting steps for SOI dewetting void finger propagation listed above.

The large difference between the observed activation energy of 2.9±0.3eV and the range of values for surface diffusion on the (100) Si surface of ~2.0-2.3eV from the literature indicates that (100) surface diffusion is not likely the limiting kinetic step in void finger propagation in dewetting SOI films. The measured value is much more consistent with the range of activation energy values for surface diffusion on the (111) Si surface from the literature given by 3.2-4.2eV, indicating the possibility that void propagation is limited by surface diffusion on (111) facets. However, due to the lack of availability of data on the expected activation energies for the other potential rate limiting steps in void finger propagation in SOI films listed above, we are not able to conclusively determine the physical origin of the activation energy we have measured for this phenomenon. Further study will be required to resolve this question.

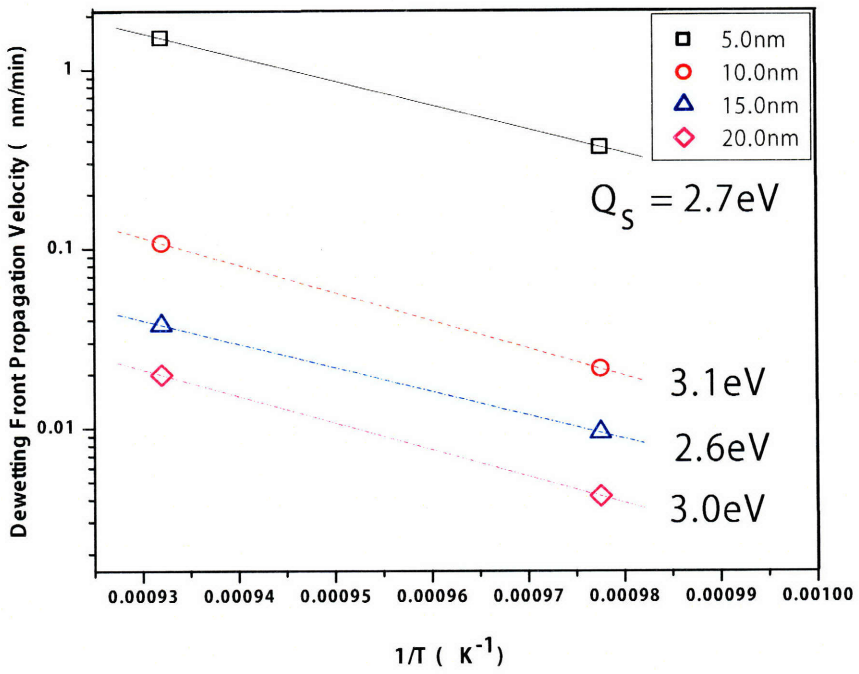

Figure 6.24: Arrhenius plot of the dewetting front propagation velocity. Activation energy values of 2.7eV, 3.1eV, 2.6eV, and 3.0eV are observed for thicknesses of 5nm, 10nm, 15nm, and 20nm, respectively.

Extension of Void Finger Propagation Model to Account for Surface Energy Anisotropy

Here, we describe the clear anisotropic behavior observed in the void finger formation and propagation process in SOI dewetting, in which void fingers are observed to propagate exclusively in <100> in-plane directions, and propose a novel model for anisotropic void finger propagation.

Close inspection of the void tip geometry has allowed us to identify the presence of slightly edge-thickened <110>-oriented straight film edge segments at void tips formed during void tip propagation, regardless of the initial mesa-edge orientation, as shown in 6.25 and 6.26. This faceted tip geometry and a steady-state edge thickening geometry are observed with time at all void tips. Similar to what we have observed for uniformly thickening and retracting film edges at <110>-oriented mesa edges, the <110>-oriented edge segments at void tips are found to be bounded by stable (111) and (311) facets.

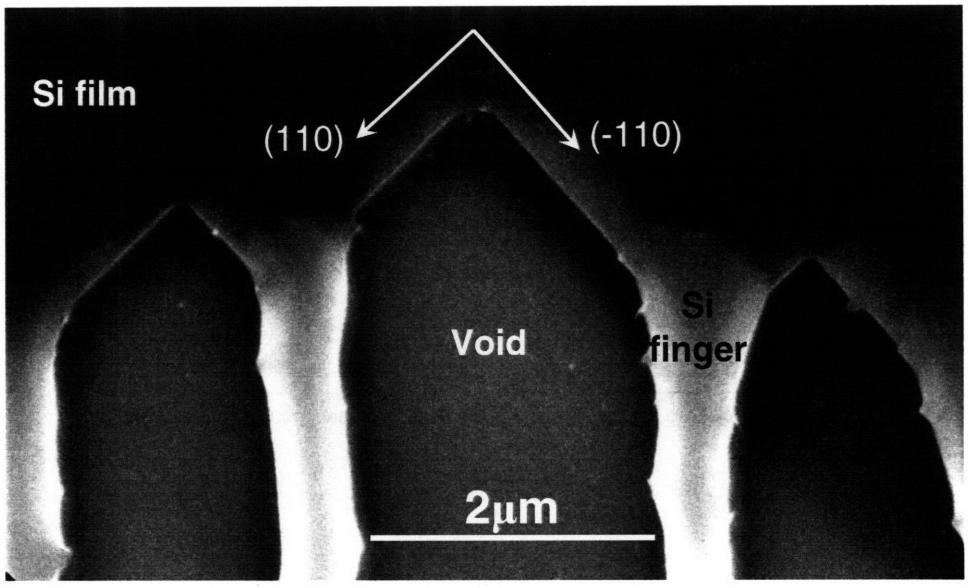

Figure 6.25: SEM image of the dewetting propagation front from a <100>-oriented patterned SOI edge in 20nm-thick SOI annealed at 750C for 4150min. The void tips exhibit clear formation of <110>-oriented edge segments, stable against breakdown due to their ability to form stable (111) and (311) facets.

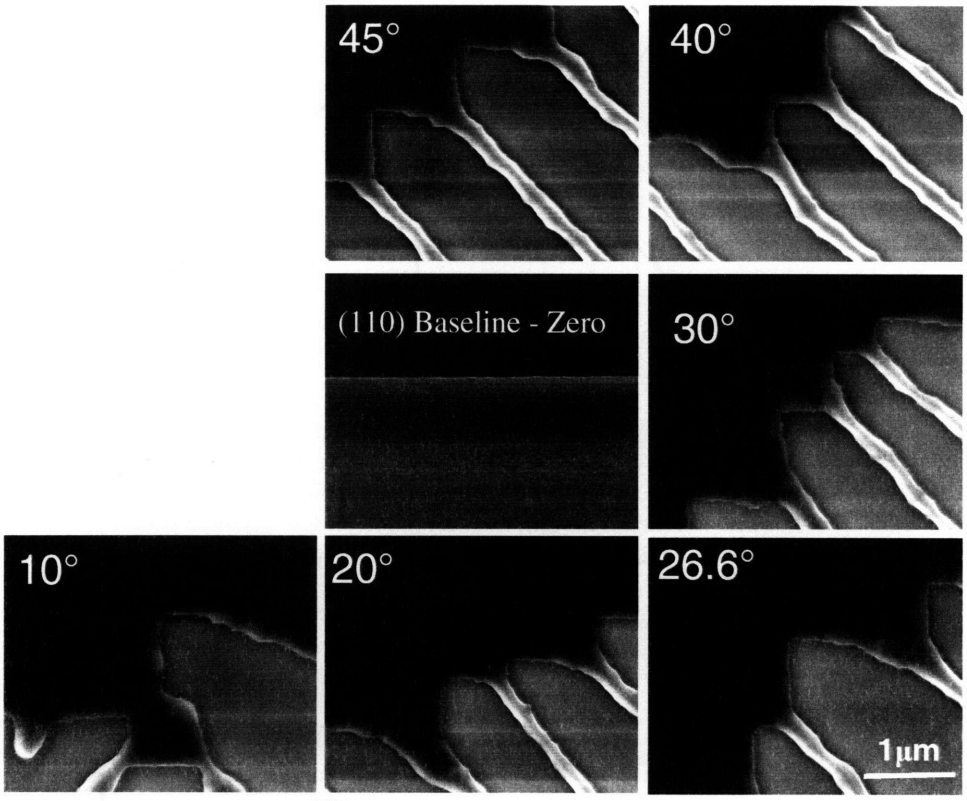

Figure 6.26: Series of SEM images of propagating void fronts in a single sample originating from patterned SOI mesas having different edge orientations. It can clearly be seen that regardless of the original mesa edge orientation, void tips form facets that intersect the substrate in the <110> in-plane directions. This allows for the formation of low energy (111) and (311) facets at the void tip.

We propose here an anisotropic extension of the isotropic Jiran-Thompson model for void finger propagation that explains how the anisotropic surface energy of a dewetting thin film material results in the propagation of void fingers preferentially in particular crystallographic directions.

We propose that the anisotropic dewetting behavior observed in void finger propagation in single-crystal anisotropic films is dictated by the detailed anisotropic

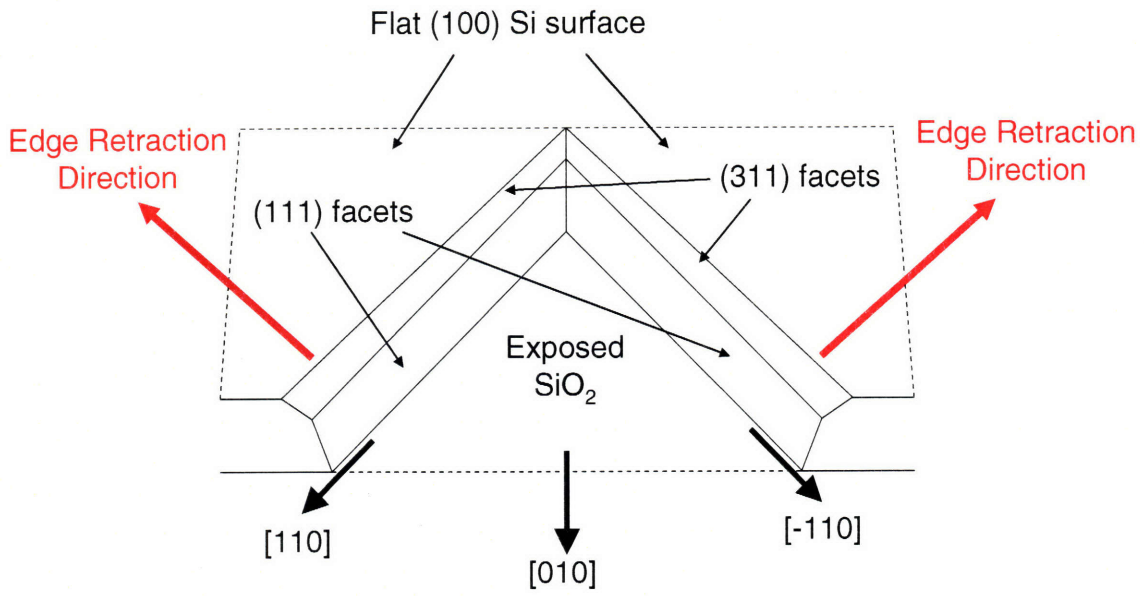

Figure 6.27: Schematic birds-eye view of a faceted void tip in SOI, looking from the void finger side toward the void finger growth direction. Straight <110>-oriented film edge segments are formed due to their ability to expose the stable (111) and (311) Si planes. The retraction of these faceted void tip edges perpendicular to themselves (shown in red), as observed in <110>-oriented patterned mesa edges during the edge thickening and retraction dewetting stage, results in a net motion of the void tip in the in plane <100> direction.

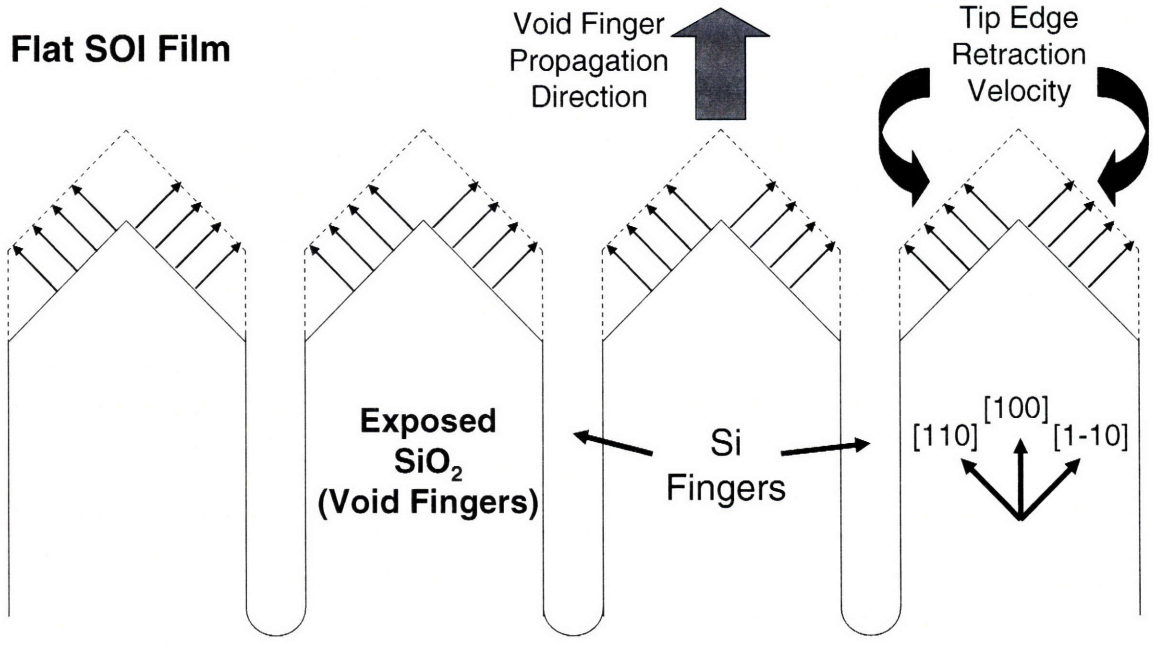

Figure 6.28: Schematic top-down view illustration of our proposed anisotropic void finger propagation mechanism. The black arrows indicate the motion of <110>-edge-oriented void tip edge segments perpendicular to their edge direction via uniform edge retraction. The dotted lines indicate the new void tip front position after this motion, indicating how uniform retraction of these edge segments results in net void propagation in the <100> direction and the formation of <100>-oriented void fingers due to the impingement of moving edge segments in neighboring void fingers upon each other.

morphological evolution mechanism that occurs at void finger tips. Under our model, the detailed steady-state morphology developed at void finger tips is determined by the most energetically stable in-plane film edge orientations available in a given anisotropic thin film system. These preferred in-plane stable edge orientations formed at void tips should be identical to the in-plane mesa edge orientations found to most stable against edge breakdown, indicating a unity of the anisotropic behavior of film edge breakdown and void finger propagation.

In our SOI dewetting study, this preferred in-plane stable edge orientation has been found to be the <110> in-plane edge orientation, which facets readily on the stable Si (111) and (311) planes. This film edge orientation has been observed to be both the most stable against breakdown at straight patterned mesa edges, as well as to be present at propagating void finger tips, as shown in Figures 6.25 and 6.26. Figure 6.27 shows a schematic illustration indicating the morphology and faceting observed in SOI voids tips.

As illustrated in Figures 6.27 and 6.28, we propose that void finger tip propagation occurs via the uniform retraction of the <110> edge-oriented tip edge segments perpendicular to themselves in the <110> direction via a process akin to the uniform edge thickening and retraction that has been observed at <110>-oriented mesa edges and described in Chapter 4. However, as shown in Figure 6.27, retracting edges at void tips are able to maintain a steady state profile and edge thickness due to the creation of new edge regions at the void tip and sinking of edge material to the Si fingers that are formed between void fingers as void tip edge segments in neighboring void fingers impinge upon each another. This ability to maintain a steady-state edge profile, as opposed to the continuously thickening edge profile observed for edge thickening and

retraction at a <110>-oriented mesa edge, allows <110>-oriented void tip edges to maintain a constant retraction velocity. As shown in Figure 6.28, under this model the retraction of the <110>-oriented void finger tip edges perpendicular to themselves at a given void finger tip results in a net growth of the void finger in the <100> in-plane direction. Similarly, the impingement of <110>-oriented void finger tip edges in adjacent void fingers upon one another during edge retraction in <110> directions results in the formation of <100>-oriented Si fingers between propagating void finger tips.

This void finger tip-focused model for anisotropic void finger propagation in single-crystal dewetting films with anisotropic surface energy represents a significant departure from previously posed models. Past authors have focused on the importance of the formation of the most stable Si facets at *the sidewalls of the Si fingers* that are formed between propagating void fingers, ignoring the role played by faceting at the propagating void finger tip.[4,71] Our careful study of the anisotropic void finger tip geometry, combined with our systematic study of the effect of in-plane SOI mesa-edge orientation on edge breakdown, has lead us to conclude that it is faceting on low energy planes *at the propagating void tip* that determines the geometries that are physically observed in anisotropic dewetting.

Summary

Through a systematic study of dewetting in (100)-oriented SOI films as a function of SOI film thickness and in-plane mesa-edge orientation, we have provided a number of key new insights into the nature of SOI dewetting in particular, and dewetting in single-crystal anisotropic thin films in general. Our study indicates that the qualitative dewetting

behavior and the kinetic scaling dependencies observed in dewetting in the anisotropic SOI dewetting system are consistent with what is predicted by our isotropic 5-step surface-energy-driven dewetting model. The edge thickening and retraction distance at <110>-oriented mesa edges was found to scale with the square root of time and the inverse power of the top Si film thickness, the edge breakdown wavelength in <100>-oriented mesa edges was found to be proportional to the top Si film thickness, and the void finger propagation velocity was found to be constant in time and proportional to the inverse cubic power of the Si film thickness, all as predicted by our isotropic surface-energy-driven dewetting model.

However, we have also observed that the detailed dewetting behavior in SOI films is highly dependent upon the underlying anisotropic surface energy of Si, with the preferred exposure of the most stable (111) and (311) Si planes determining anisotropic SOI dewetting behavior. We have found that in (100)-oriented SOI layers, the stability of these planes results in the formation of stable <110>-oriented film edges which allow for the exposure of these stable planes and that the retraction of these edges, whether at the thickening retracting straight film edges of <110>-oriented edges or at the <110>-oriented retracting edges observed to be present at propagating void finger tips, dictates the anisotropic geometries observed in SOI dewetting.

III. Comparison of Dewetting Kinetics in Bonded and SIMOX SOI

We also present here for the first time a conclusive comparison of the kinetics of SOI dewetting in bonded and SIMOX SOI films having identical film thicknesses. Bonded and SOI samples of identical 20nm SOI thickness were annealed together at 750C for 1780min and 2820min. As can be seen from the side-by-side SEM images in Figures 6.29 and 6.30, we have observed that bonded and SIMOX films exhibit nearly identical dewetting kinetics, with evolution rates determined only by the SOI thickness and annealing conditions.

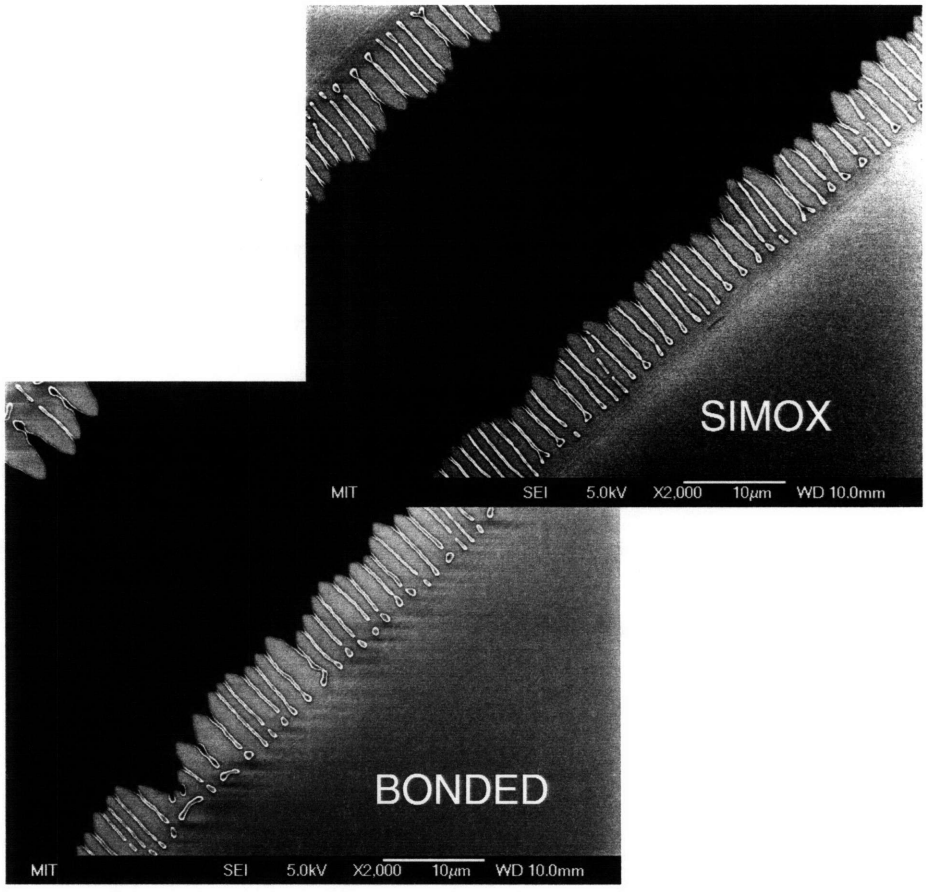

Figure 6.29: SEM images comparing dewetting behavior at <100> edge-oriented mesas in 20nm-thick bonded and SIMOX SOI films annealed under identical conditions of 750C, 1780min. The nearly identical dewetting front propagation distances indicate that dewetting behavior in the two films is identical for the same SOI thickness and annealing conditions.

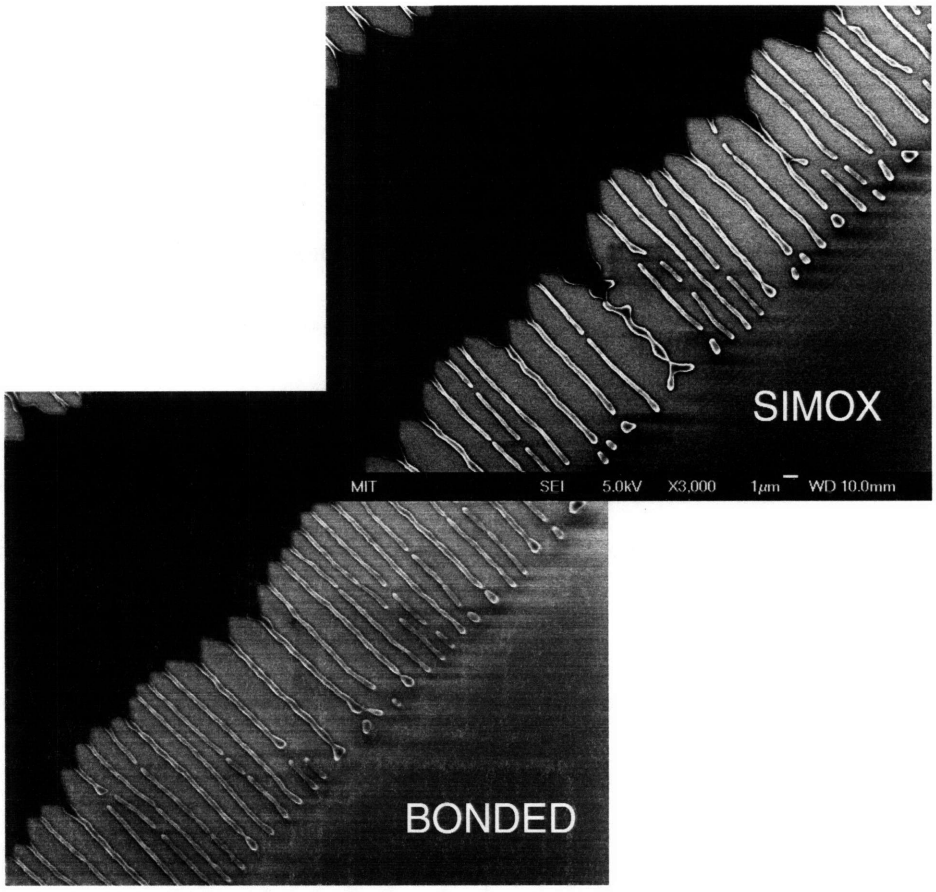

Figure 6.30: SEM images comparing dewetting behavior at <100> edge-oriented mesas in 20nm-thick bonded and SIMOX SOI films annealed under identical conditions of 750C, 2820min. The nearly identical dewetting front propagation distances indicate that dewetting behavior in the two films is identical for the same SOI thickness and annealing conditions.

IV. Stabilizing SOI Structures Against Dewetting via Mesa-Edge Coverage

We now turn our attention to a novel method we have developed for stabilizing patterned SOI structures against dewetting, as will be required to enable the deployment of fully-depleted transistors by the IC industry.

Figure 6.31 demonstrates the effectiveness of the dielectric edge coverage stabilization method invented in this thesis work. This 14.8nm-thick SOI mesa with partial edge coverage was UHV annealed at 800C for 90min, a condition known to result

in dewetting in uncovered 15nm-thick SOI mesa structures. Due to a fortuitous mask misalignment during the BOE SiO_2 etching process to expose the middle of the SOI mesa, the SOI mesa shown in Figure 6.31 had some of its edge regions covered with a stabilizing capping SiO_2 film, while other edge regions were not covered. The covered edges can clearly be seen to have been stable against dewetting, while the uncovered regions were not, wonderfully demonstrating the effectiveness of the dielectric edge-coverage SOI stabilization method. The method is ideal for the critical raised source/drain Si selective epitaxy step, as it allows for the exposure of the Si surface to the ambient for epitaxial growth.

A second important concept we propose for stabilizing SOI films against dewetting is use of patterned structures with edges parallel to in plane <110> directions in (100)-oriented SOI films. As reported in detail above, due to the easily accessible low energy (111) and (311) facets for edges parallel to <110> directions, these edges exhibit extremely high stability against edge breakdown. However, inevitably other edge orientations will be exposed at corners in such patterned structures. If the use of edge coverage stabilization around the complete edge of patterned structures is not desirable, it may be sufficient to just have edge coverage at the corners of patterned mesa structures with edges parallel to the stable <110> mesa directions.

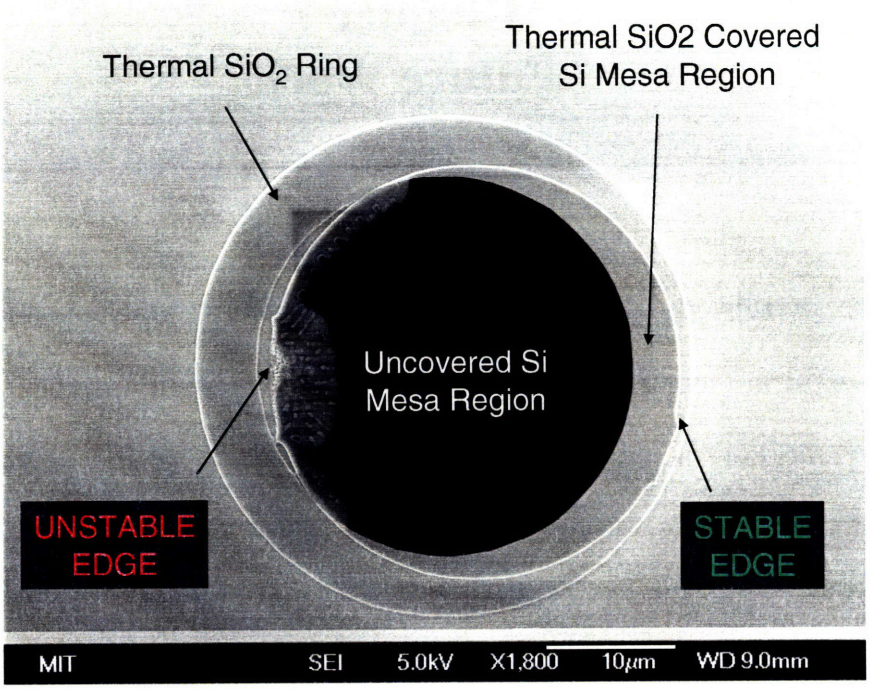

Figure 6.31: SEM micrograph demonstrating the effectiveness of the dielectric edge-coverage stabilization technique. The misaligned thermal oxide ring SOI mesa edge-coverage structure shows that SOI mesa edge regions without the edge coverage layer are unstable to dewetting, while covered regions are stable.

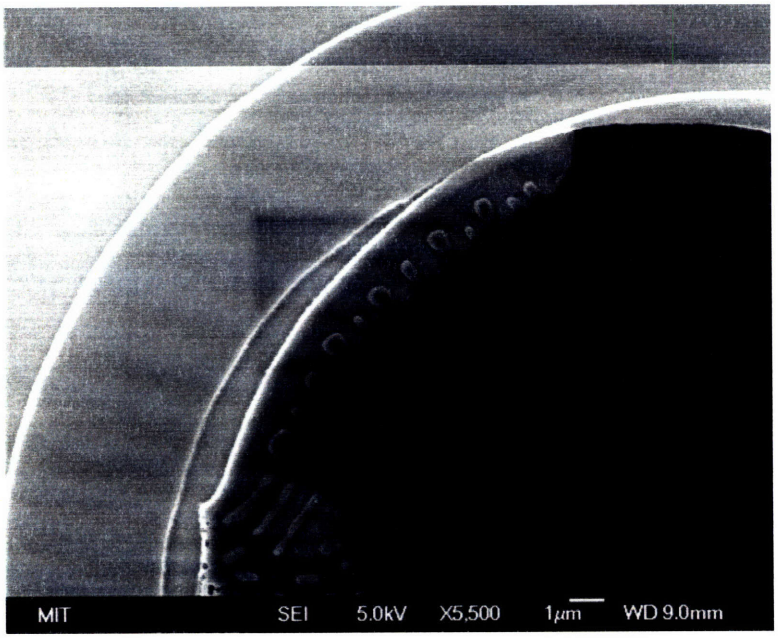

Figure 6.32: Zoomed in view of the dielectric edge stabilization result shown in Figure 6.26.

Chapter 7
Future Work

The groundwork laid in the fundamental study of (100)-oriented ultra-thin SOI films presented in this thesis points to a number of interesting opportunities for future research, particularly in the areas of anisotropic dewetting science and directed self-assembly of Si nanostructures via anisotropic dewetting.

Opportunities abound to push our understanding of dewetting science forward following up on the results of this thesis work. Due to the highly controlled nature of single-crystal thin films-on-insulator, they appear to offer ideal materials systems for fundamental studies of dewetting.

Perhaps the greatest research opportunity available as an outgrowth of the work presented in this thesis is the opportunity to study anisotropic dewetting further to ideally lead to the development of a general theory directly relating the geometry and kinetics of anisotropic dewetting in any single-crystal thin film layer to its Wulff shape. A systematic study of anisotropic dewetting in patterned mesa structures with various in-plane orientations in (110), (111), (110), and (311)-oriented SOI layers performed in a single UHV system with a consistent cleaning and annealing procedure would reveal the fundamental elements of anisotropic dewetting in the model SOI system and likely enable the development of a more complete theory of anisotropic dewetting. Furthermore, ultra-thin single-crystal Ge-on-insulator layers have recently become available for study. A systematic annealing study of dewetting in Ge-on-insulator would enable the beginning

of the development of an understanding of anisotropic dewetting in Group IV materials in general.

Another interesting potential future area of SOI dewetting research relates to the effect of surfactants on dewetting kinetics. There is evidence in the literature that hydrogen has a strong surfactant effect on Si surfaces, greatly modifying facet surface energies and the surface diffusion coefficient.[101,102] Furthermore, as discussed in Appendix B, Ge appears to have some very interesting surfactant effects on SOI dewetting kinetics as well. A fundamental study of the kinetics of SOI dewetting under various hydrogen pressures and Ge coverages would allow for the extraction of SOI dewetting kinetic dewetting parameters to carefully study the effects of these surfactants on SOI dewetting.

A particularly exciting idea for future work in SOI dewetting is in the area of templated self-assembly of Si nanostructures. The observed order present in the Si island and finger structures formed by anisotropic dewetting in our annealing study of SOI films, especially in <100>-edge oriented mesas, was striking. However, significant scatter in the edge breakdown wavelength of dewetting was observed, we believe, due to random roughness introduced at the film edge by the somewhat aggressive plasma Si mesa etch used in this study. Our results highlight the importance of the initial mesa-edge geometry in determining the average value and the scatter in the values of the edge breakdown wavelength during dewetting. We propose a dewetting study in which a sinusoidal edge bias is used to template the edge breakdown wavelength in dewetting. By using edge bias profiles having different wavelengths, we believe that the Rayleigh breakdown wavelength of dewetting breakdown at a mesa edge can be controlled. As, according to

our model, controlling the wavelength should lead to control over the whole dewetting geometry, this concept could provide a technique for making ordered Si nanostructures of precise, controlled geometries. Furthermore, by biasing the edge breakdown with a single wavelength, the scatter in the edge breakdown wavelength would be expected to be significantly decreased as well.

Chapter 8
Summary and Conclusions

This thesis has focused on illuminating the basic physical mechanisms of anisotropic dewetting in ultra-thin SOI films. In this work, we developed a 5-step surface-energy-driven dewetting model for SOI dewetting based upon the capillary film edge instability and the generalized Rayleigh instability. The five steps in this model are: 1.) supercritical film void formation, 2.) uniform film edge thickening and retraction, 3.) thickened film edge breakdown, 4.) film void finger formation and propagation, and 5.) film finger breakdown. Furthermore, we made an original contribution to the theory of dewetting in thin solid films by modeling and developing an expression for the edge retraction distance at an initially straight patterned film edge for the first time, predicting a square root dependence on time and an inverse dependence on film thickness. Furthermore, we demonstrated that our surface-energy-driven model was able to well explain all of the key experimental observations in the existing SOI literature. Using basic thermodynamic arguments and physical reasoning, we refuted the consensus theory in the existing literature that SOI dewetting is driven by a stress-driven morphological instability.

We also presented the results of a careful dewetting study in (100)-oriented ultra-thin SOI layers with thicknesses in the range of 5-35nm, designed to quantitatively measure dewetting kinetics in SOI and to reveal as much new information about anisotropic dewetting in SOI films as possible. Through the use of a final HF dip in our UHV anneal pre-clean, we were able to observe the kinetics of SOI dewetting without

their being convoluted with the kinetics of SiO_2 desorption, as had been the case in all previous SOI dewetting studies. Through the study of dewetting in patterned SOI mesas, we were able to study the kinetics of SOI dewetting in a controlled way, as opposed to the existing work in which dewetting of initially flat continuous films was studied, representing a convolution of uncontrolled void nucleation and dewetting growth kinetics.

In our study, we observed highly anisotropic dewetting behavior that was very sensitive to patterned mesa edge orientation. <100> in-plane-oriented SOI mesas were found to be the least stable against edge breakdown, while <110> in-plane-oriented mesas were found to be highly stable against edge breakdown and void finger formation and growth. Due to the enhanced stability of <110> in-plane-oriented SOI mesa edges, we were able for the first time to quantitatively measure the kinetics of the initial uniform edge thickening and retraction phase of thin film dewetting and found that the edge retraction distance depended on the square root of time and the inverse of the film thickness, as predicted by our edge thickening and retraction model. Due to the uniform and reliable edge breakdown observed in <100> in-plane-oriented SOI mesas, by measuring the dewetting front propagation distance after edge breakdown in these mesas for various experimental conditions, we were able to accurately measure dewetting (void finger) front propagation velocities and found that the propagation velocity depends on the negative third power of the film thickness, agreeing with the film void propagation theory of Jiran and Thompson used in our proposed dewetting model. Furthermore, we extracted an activation energy for the dewetting front propagation rate of 2.9±0.3eV, agreeing reasonably well with the activation energy for surface diffusion on the (111) Si surface plane, but not definitively identifying this as the rate limiting kinetic process in

dewetting front propagation. Furthermore, we also observed that dewetting void fingers formed preferentially in <100> in-plane directions and found that stable <110>-oriented edge segments were formed at propagating void tips. We propose for the first time that the preferred anisotropic void finger propagation directions in anisotropic dewetting are not determined by the lowest energy available to the sidewalls of the film fingers that are left behind by void finger growth, but rather by the lowest energy configuration available at the growing void tip. We also propose for the first time that void finger formation is the result of the intersection of retracting void tip edge segments that undergo continuous retraction perpendicular to themselves and that observed void finger orientations in anisotropic dewetting are completely determined by this process.

We also demonstrated definitively for the first time that dewetting kinetics in bonded and SOI films are identical, depending only on the SOI layer thickness. We also invented and demonstrated the effectiveness of the dielectric edge-coverage technique for stabilizing patterned SOI structures against dewetting, a technique that we hope will be valuable to the IC industry as it attempts to deploy its next generation of transistors using the ultra-thin SOI materials platform.

Appendix A
Anisotropic Surface Energies in SOI Films

In this section, we briefly review the anisotropic surface energy properties of silicon in order to motivate and explain the anisotropic extensions of our isotropic dewetting model described in Chapter 6.

From both the experimental and theoretical literature, the stable facets of Si have been determined to be (111), (311), (110), and (100).[63-65] All of this literature puts these facet energies in the 1-2 J/m^2 range. Jaccodine used Si crack propagation experiments to perform the only experimental measurement of an absolute surface energy in Si: 1.23 J/m^2 for the (111) plane.[103] However, the literature is inconsistent in its evaluation of which of these facets are most stable. All available experimental studies of Si surface facet energies, outside of that performed by Jaccodine, were performed by the observation of presumably equilibrium Si particle or void shapes and the use of the Wulff construction. At 600C, Follstaedt studied equilibrium-shaped voids in Si and found the (111) facets to have lowest energy, followed by (110) and (100), with 7% and 9% higher energy, respectively.[64] Interestingly, he did not observe stable (311) facets. Eaglesham et al. studied equilibrium-shaped Si voids annealed at 700C and found (111) facet to have lowest energy, followed by (100), (311), and (110), with 10, 12, and 16% higher energies respectively.[63] In contrast to these two studies, Bermond et al. studied the equilibrium shape of 1050C-annealed Si pillars to determine that the (100) facet is the lowest in energy, followed by (311), (110), and (111), with 1, 2, and 3% higher energies respectively.[65]

The literature on the anisotropic surface energies in Si is inconclusive and inconsistent in terms of predicting the relative stability of Si surface facets. However, our experimental results in SOI dewetting, along with the results of other authors, indicate that the (111) and (311) planes dominate SOI dewetting behavior, indicating that (111) and (311) planes are the most stable planes for the UHV annealing conditions and 750-1200C temperature range used in our SOI dewetting work and that from the literature. Therefore, we focus here on illuminating the key geometrical aspects of (111) and (311) with respect to dewetting in (100)-oriented SOI films.

Figure A.1 shows the normal vectors of all of the (111) and (311) Si planes for one octant of three-space. (Due to the four-fold crystalline symmetry of Si about the [001] axis and the inverse symmetry of the Si crystal, this octant fully describes all (111) and (311) planes in Si). Let us consider the [001] in Figure A.1 to represent the surface normal direction of a (100)-oriented SOI film. We can see from this figure that there is one type of (111) plane and two distinct types of (311) planes for a (100)-oriented SOI film, with the normal vector of the (113) plane shown in Figure A.1 making a larger angle with the (001) film surface plane and the normal vectors of the (311) and (131) planes making a shallower angle with the (001) film surface plane. Figure A.2 shows the traces (or intersections) of these facet planes with the (001) film surface plane. The (111) and (311) planes are seen to intersect the (001) film surface plane in the <110> direction, while the (311) and (131) planes are seen to intersect the (001) film surface plane in the $<\bar{1}30>$ and $<310>$ directions, respectively. These intersection directions dictate the SOI mesa-edge orientations that can facet on stable {111} and {311}-type planes while maintaining straight edges. Thus, due to the crystalline symmetry of Si, in (100)-oriented

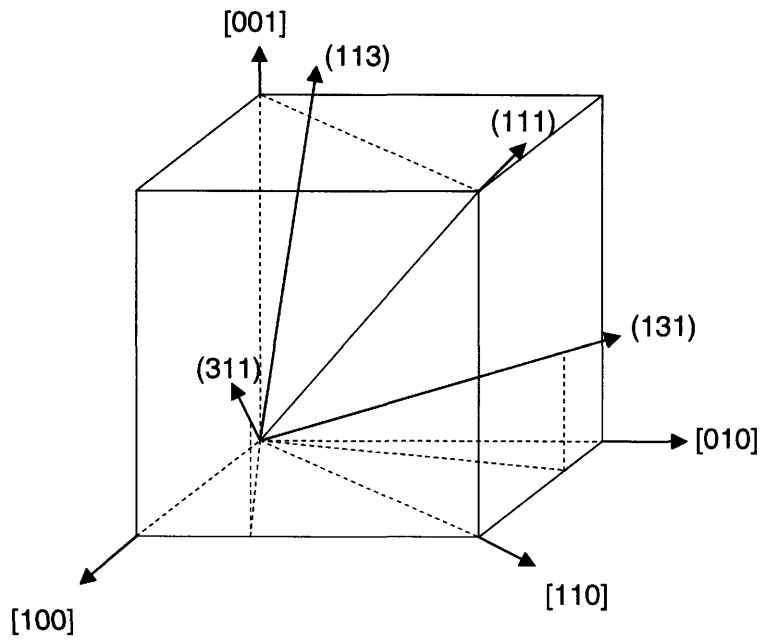

Figure A.1: Schematic illustration showing the normal vectors of {111} and {311} planes in Si. The [001] direction represents the surface normal of the (100)-oriented SOI films studied in this work.

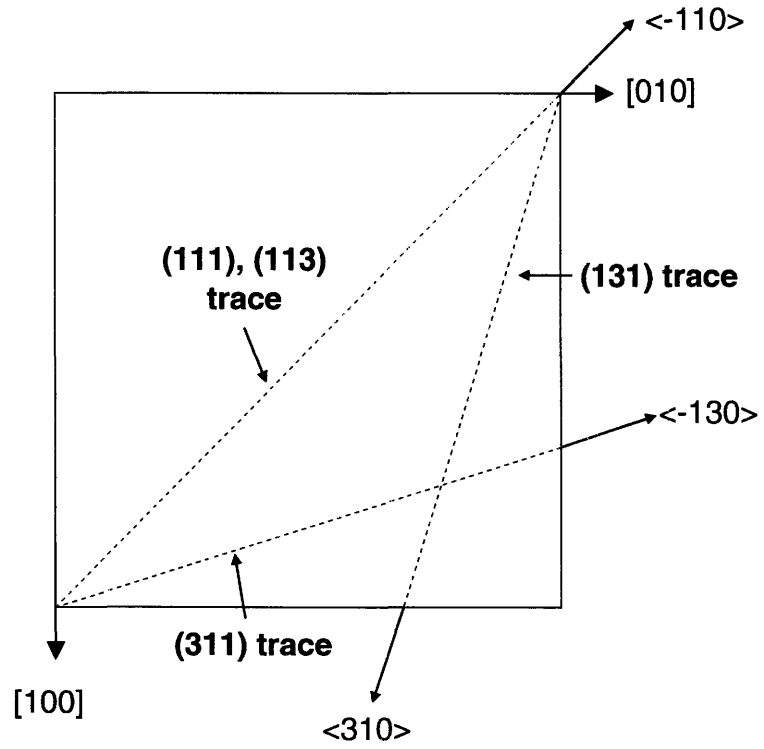

Figure A.2: Schematic illustration showing the traces (lines of intersection) of {111} and {311} planes in Si with the surface of (100)-oriented SOI films. The (111) and (113) facets intersect the surface in the same $<\bar{1}10>$ direction, while the (311) and (131) facets intersect the surface in the $<\bar{1}30>$ and $<310>$ directions, respectively.

SOI films there are 4 in-plane <110> straight mesa-edge orientations that allow for the exposure of (111) and (113)-type facets, while there are 8 in-plane <310>-type straight mesa-edge orientations that allow for the exposure of (311)/(131)-type facets.

Assuming that {111} and {311} facets are the most stable in Si for the UHV annealing conditions used in our SOI dewetting study and those performed in the literature, we have thus identified the <110> and <310>-type film-edge orientations in (100)-oriented SOI films to be special orientations that can allow for the exposure of these stable Si facets while maintaining straight film edges.

Appendix B
Effect of Ge Coverage on Dewetting in SOI Films

In this appendix, we report on the effect the presence of a thin deposited layer of Ge on the SOI surface has on the SOI dewetting process. We have found that the deposition of a Ge layer on an SOI film during UHV annealing results in 1.) a new dewetting initiation mechanism in flat continuous SOI film regions that occurs at Ge islands formed on the SOI layer and 2.) a significant enhancement of SOI dewetting kinetics.

We report our observations on the effect of Ge coverage on SOI dewetting here in an appendix due to the fact that these results were obtained via uncontrolled, inadvertent Ge deposition during UHV annealing and were performed on SOI samples not possessing the range of in-plane patterned mesa-edge orientations used in the careful SOI dewetting study described in the body of this thesis. However, due to the interesting effects this inadvertent Ge deposition had on dewetting in ultra-thin SOI films, we report our observations of the effect of the presence of Ge on SOI dewetting here for the benefit of other researchers.

Inadvertent Ge deposition occurred in the first SOI dewetting experiments performed in this work due to the presence of Ge on the walls of the quartz tube in the hot-walled UHV-CVD system used in this work, due to the previous use of the system for the growth of Ge layers on Si wafers using GeH_4 as a source gas. During our first UHV annealing experiments, this Ge on the quartz tube walls served as an unintentional evaporation source for Ge, resulting in Ge deposition on the annealed SOI samples.

(Note: Prior to the performance of the UHV annealing study reported in the body of this thesis, this Ge contamination issue was remediated by coating the walls of the UHV-CVD furnace with > 10μm of Si to serve as a cap on the Ge layer. Energy dispersive spectroscopy (EDS) and x-ray photoelectron spectroscopy (XPS) measurements of the surfaces of SOI samples UHV annealed after this Si quartz tube wall coating procedure confirmed that no Ge contamination was present in samples annealed after this procedure was performed.)

Furthermore, dewetting initiation was only studied at <110> in-plane-oriented film edges in the SOI samples studied with the presence of Ge on the UHV-CVD furnace walls, as we had not yet introduced the use of various in-plane oriented Si mesa edges at this point in our study. Thus, only etched and cleaved <110>-oriented SOI edges were studied under Ge deposition conditions.

The uncontrolled nature of these UHV SOI annealing experiments with Ge deposition precluded the performance of a detailed kinetic study of the effect of Ge on SOI dewetting kinetics. However, we describe the key qualitative observations we have made on the effect of Ge deposition on SOI dewetting below.

Effect of Ge Deposition on SOI Dewetting Initiation in Flat Continuous Film Regions

Deposition of Ge during UHV annealing has been found to result in a new mechanism for SOI dewetting initiation in initially flat continuous SOI film regions in which initiation occurs at deposited Ge islands. Deposition of Ge on Si surfaces at sufficiently high temperatures is well known to result in monolayer Ge coverage of the Si

surface and Ge island formation via the Volmer-Weber thin film growth mode.[104] As shown in Figure B.1, deposition of Ge from the furnace tube walls during UHV annealing results in the formation of a high density of Ge islands on the SOI surface. Deposition of Ge during annealing has also been observed to result in local dewetting initiation and growth in initially flat continuous SOI film regions, as shown in Figure B.1. The SEM micrographs in Figure B.2 show more clearly the film morphology at these dewetting initiation sites. The islands on the SOI surface and islands present in the middle of the circular SOI dewetting region, shown in Figure B.2(a), were confirmed to be Ge islands via energy dispersive spectroscopy (EDS) and x-ray photoelectron spectroscopy (XPS) measurements. Figure B.2 clearly shows that dewetting initiation in initially flat continuous SOI film regions occurs at film locations where particularly large Ge islands are present. Careful examination of the Ge surface islands in Figure B.2(a) shows a thin dark ring surrounding each island, representing a local trench formed in the SOI film around the base of the Ge islands. We speculate that high local stress values in the SOI film region immediately adjacent to the Ge island edges, caused by the high lattice-mismatch between Ge and Si, result in the formation and growth of these trenches, ultimately resulting in the uncovering of the underlying SiO_2 layer and creating a supercritical film void that is unstable to growth by surface-energy-driven dewetting. Figure B.2(b) shows the very initial growth stage immediately after critical void formation by this mechanism at a Ge island on the SOI film surface.

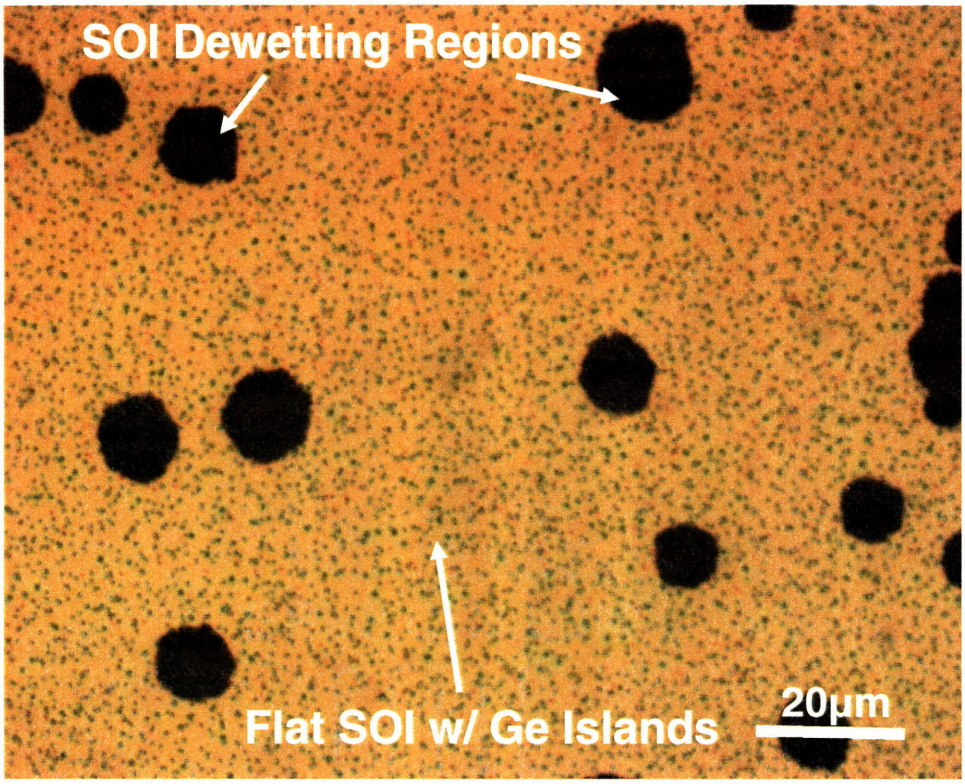

Figure B.1: Optical micrograph of an SOI sample UHV annealed under Ge deposition conditions, showing Ge islands formed on the SOI surface and a high density of SOI dewetting initiation sites in initially flat continuous SOI regions. 50nm SOI film UHV annealed at 800C for 216min.

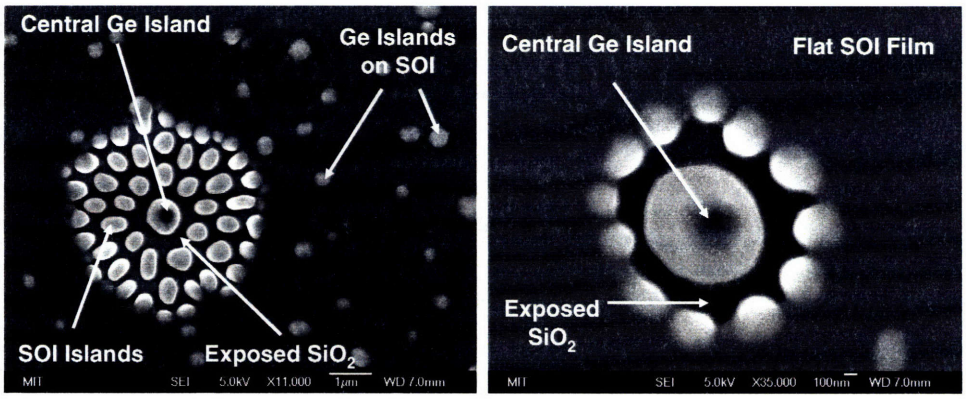

Figure B.2: SEM micrographs showing initiation of SOI dewetting at Ge islands in initially flat continuous SOI regions. 50nm SOI film UHV annealed at 800C for 120min.

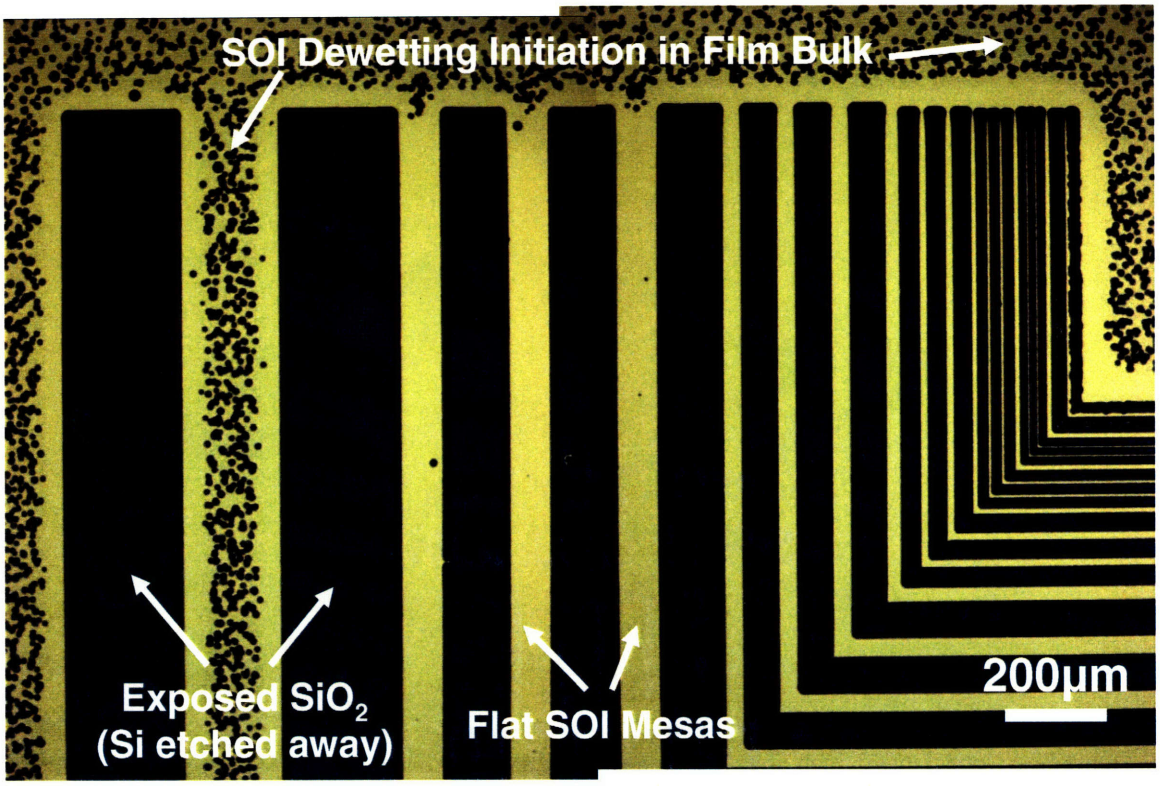

Figure B.3: Composite optical micrograph illustrating the nature of SOI dewetting initiation and growth in <110>-oriented patterned SOI mesa structures during UHV annealing under Ge deposition conditions. The blue regions are regions where the top Si layer has been etched away, the yellow regions represent undewetted SOI film regions, and the dark lines bordering these two regions and the small dark circles represent dewetting SOI regions. A region where dewetting initiation in initially flat non-edge SOI film regions is excluded can clearly be seen to exist at each patterned SOI mesa edge, resulting non-edge related SOI dewetting initiation being completely suppressed in SOI mesas with widths ≤ 100μm. 35nm SOI film UHV annealed at 850C for 62min.

Here, we describe another very interesting observation related to the Ge island-induced dewetting initiation mechanism in flat continuous non-edge SOI film regions. At any cleaved or patterned SOI mesa edge, this Ge island-induced dewetting initiation mechanism is found to be completely suppressed for flat continuous film regions within a specified distance from an edge, as shown in Figure B.3, creating a border of "dewetting initiation exclusion" next to all patterned mesa edges. As seen in Figure B.3, this dewetting initiation edge exclusion effect has the result that SOI dewetting in non-edge

film regions is completely suppressed in patterned SOI mesas having widths below a critical value. In Figure B.3, complete suppression is observed for SOI mesas with widths ≤ 50μm.

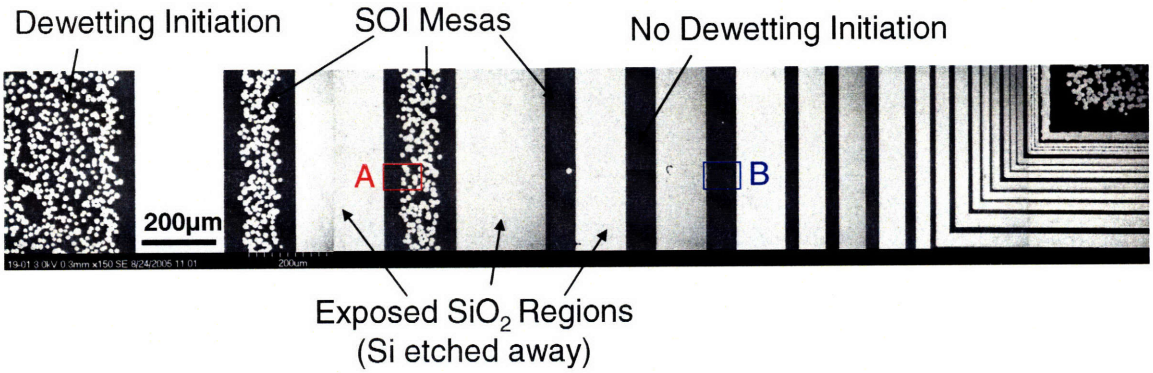

Figure B.4: Composite SEM micrograph showing the same dewetting initiation exclusion in flat continuous film regions next to mesa film edges as in Figure B.3. The red box marked A is the location where the close-up SEM micrograph in Figure B.5 was taken and the blue box marked B is the location where the SEM micrograph in Figure B.6 was taken. 35nm SOI film UHV annealed at 850C for 30min.

Figure B.4 is a composite SEM micrograph illustrating this same edge exclusion effect. Figure B.5 shows a zoomed in view of the portion of the 200μm wide SOI mesa shown in the red box in Figure B.4 marked with the letter A, while Figure B.6 shows a zoomed in view of the 50μm wide SOI mesa shown in the blue box marked with the letter B in Figure B.4.

From Figure B.5, taken at the edge of a 200μm wide SOI mesa, it can be seen that Ge island formation has been suppressed over a distance of ~30μm from the patterned edge, along with non-edge dewetting initiation suppression. In Figure B.6, showing a 50μm wide SOI mesa, Ge island formation and attendant dewetting initiation in non-edge film regions are observed to be completely suppressed. We believe that this complete suppression can be understood to be the result of the overlap of the two ~30μm wide Ge island formation exclusion regions from each mesa side.

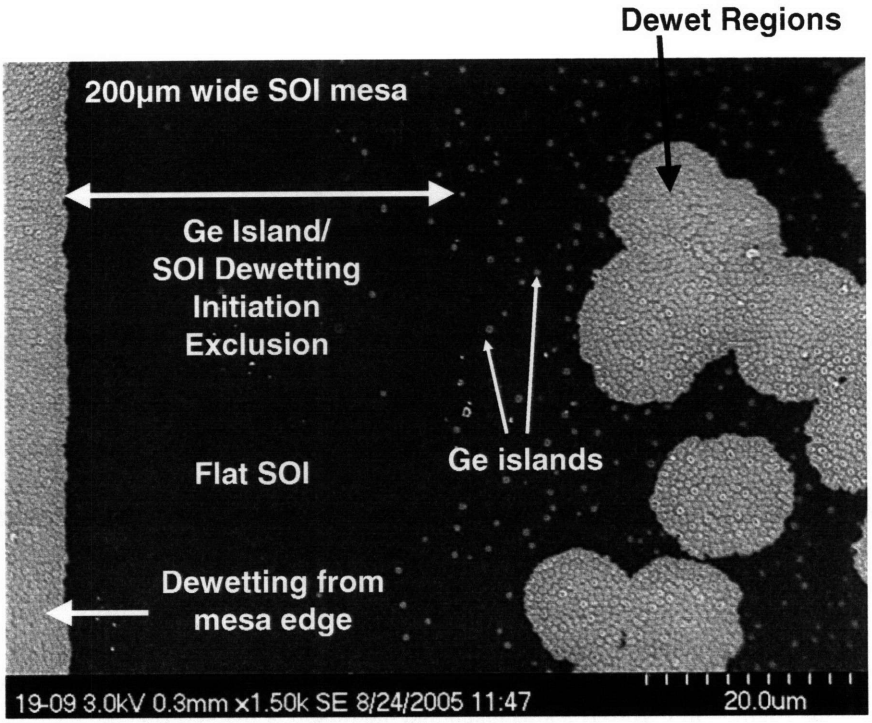

Figure B.5: SEM micrograph of the portion of the 200µm wide SOI mesa identified by the red box marked A in Figure B.4. A region of Ge island formation and dewetting initiation exclusion is observed to extend ~30µm from the SOI mesa edge.

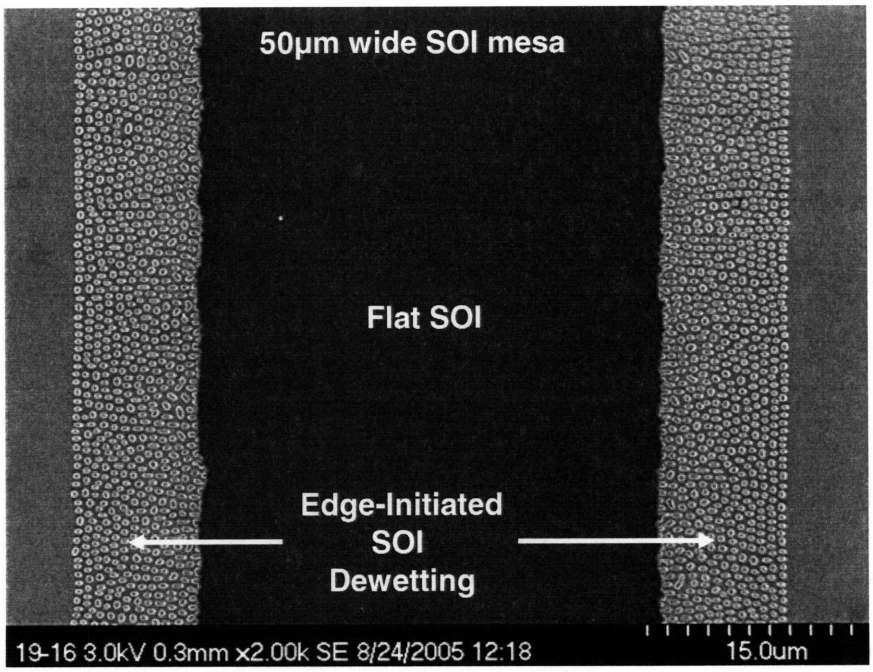

Figure B.6: SEM micrograph of the region on the 50µm wide SOI mesa identified by the blue box marked B in Figure B4. Ge island formation and attendant dewetting initiation on non-edge film regions is observed to be completely suppressed.

Due to our inability to perform a controlled study of this edge exclusion effect, we can only speculate as to its origin. One plausible theory is that somehow SOI mesa edges getter Ge atoms from the SOI surface, thus removing Ge atoms present within a surface diffusion distance of SOI mesa edges and preventing the nucleation and growth of Ge islands. However, the exact origin of this fascinating effect is currently unknown and will be a subject of future study.

Effect of Ge Deposition on SOI Dewetting Kinetics

The presence of Ge on the SOI film surface has also been found to significantly enhance SOI dewetting kinetics. Although we did not perform SOI UHV annealing experiments under identical conditions with and without Ge to directly determine the effect of Ge on SOI dewetting kinetics, Figure B.7 provides a clear illustration of the large enhancement in SOI dewetting kinetics that results from the presence of a Ge layer on the SOI film surface. Figure B.7(a) shows the dewetting evolution at an etched <110>-oriented Ge-free SOI mesa edge in a 35nm-thick film UHV annealed at 800C for 1310min, while Figure B.7(b) shows the evolution at a cleaved <110>-oriented Ge-covered SOI sample edge in a 50nm-thick film UHV annealed at the same temperature for 125min. The Ge-covered sample can be seen to have undergone significantly more dewetting evolution than the Ge-free sample, even though the Ge-covered SOI film is significantly thicker and has been annealed for approximately an order of magnitude less time, indicating a significant enhancement of SOI dewetting due to Ge coverage. Again,

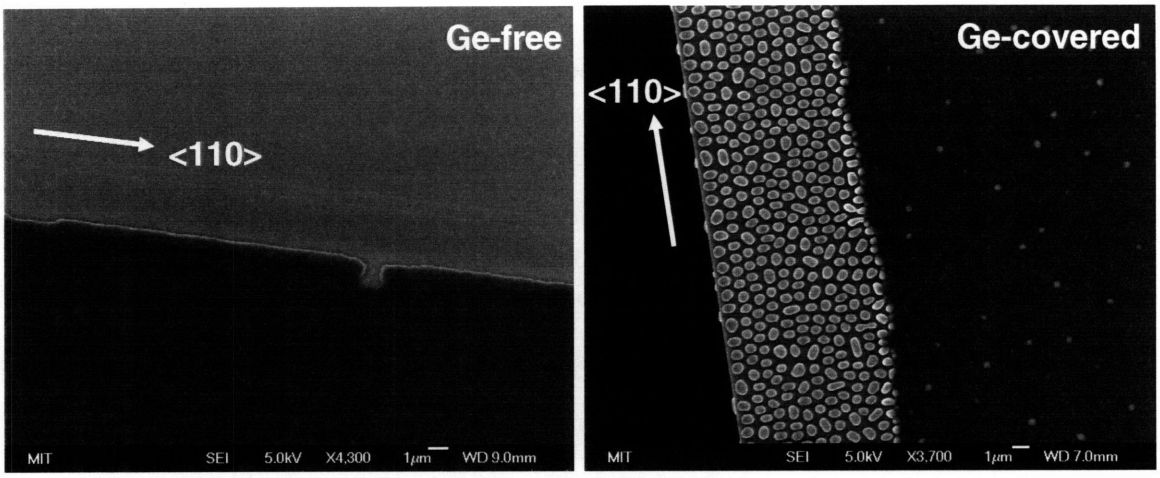

Figure B.7: SEM micrographs of dewetting at SOI film edges illustrating the significant enhancement of SOI dewetting kinetics caused by the presence of a Ge layer on the SOI surface. a) <110>-oriented patterned edge in a 35nm-thick Ge-free SOI mesa after UHV annealing at 800C for 1310min. b.) <110>-oriented cleaved edge in a 50nm-thick Ge-covered SOI mesa after UHV annealing at 800C for 125min. The edge breakdown and significant dewetting front propagation observed in the Ge-covered sample relative to the Ge-free sample, even though the Ge-covered sample is significantly thicker and has been annealed for approximately an order of magnitude less time, indicates that the presence of Ge on an SOI surface greatly enhances SOI dewetting kinetics.

due to our inability to perform controlled kinetic studies to quantitatively compare the difference in dewetting kinetics between Ge-covered and Ge-free SOI samples, we can only speculate as to the origin of this Ge-related enhancement of SOI dewetting kinetics. We speculate that the presence of Ge on the SOI top Si surface increases the Si surface diffusion coefficient, perhaps by allowing Si surface atoms to exchange to the top of the Ge-coated surface where the weaker Si-Ge bond relative to the Si-Si bond allows for easier Si surface diffusion and increased dewetting evolution rates. Again, this presents an interesting subject for future study.

Another quite interesting observed effect of the presence of Ge on SOI dewetting kinetics is that the edge dewetting propagation distance in <110>-edge-oriented SOI mesas is found to decrease with decreasing mesa width below a critical mesa width, as shown in Figure B.8. For the 35nm-thick Ge-covered patterned SOI sample annealed at

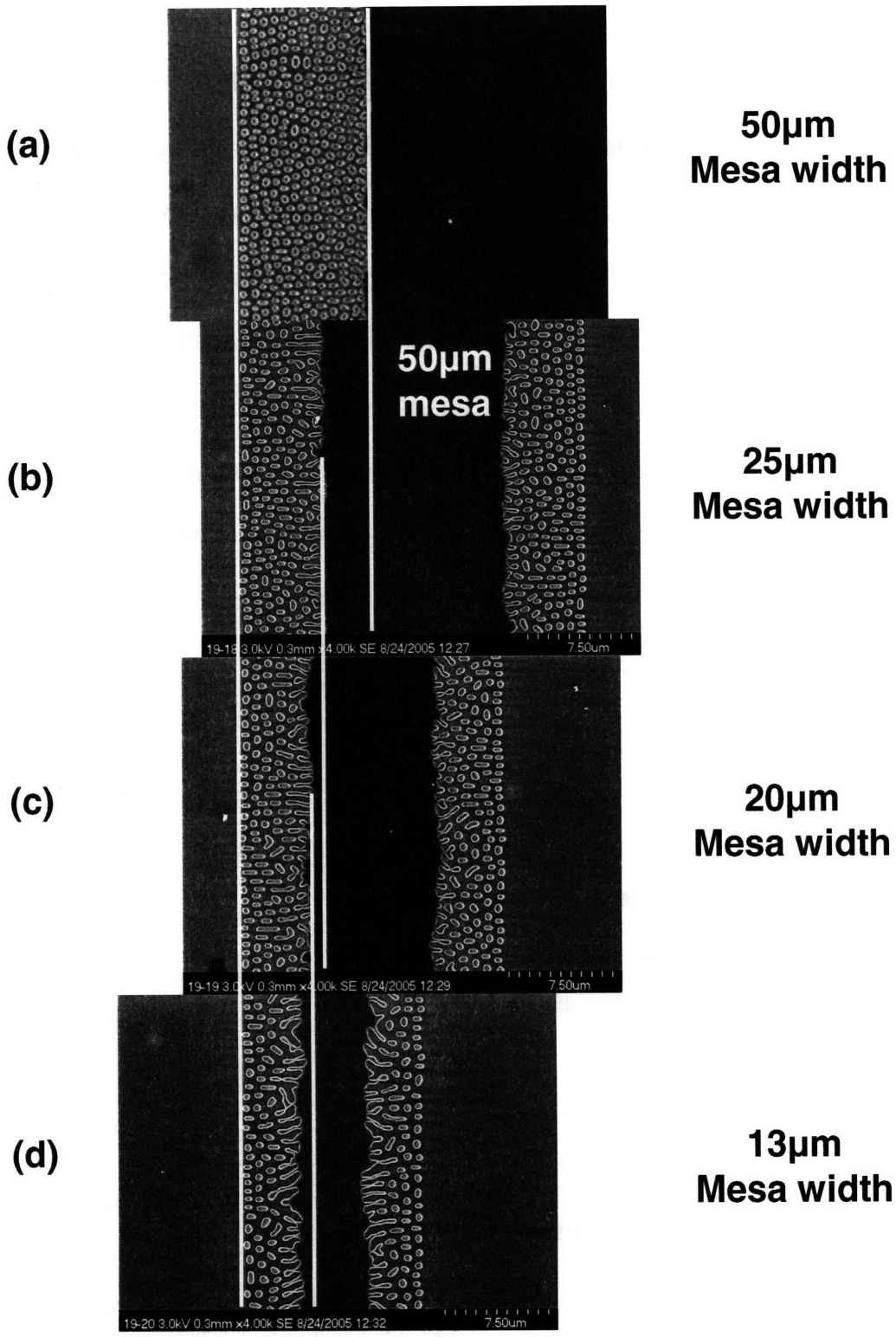

Figure B.8: SEM micrographs showing the decrease in the edge dewetting propagation distance with decreasing patterned SOI mesa width in Ge-covered samples. 35nm SOI UHV annealed at 850C for 30min. SOI mesa widths are: a.) 50µm, b.) 25µm, c.) 20µm, and d.) 13µm.

850C for 30 min shown in Figure B.8, we measured the average edge dewetting propagation distance in rectangular mesas like those shown in Figure B.8 and in square mesas as well. These results are plotted in Figure B.9. Quite interestingly, the critical mesa width below which decreases in the edge dewetting propagation distance is very similar to the critical mesa width below which complete Ge island formation and non-edge dewetting initiation suppression was observed in this sample, indicating that the two effects are somehow linked. However, at this time the origin of this effect remains unknown. Furthermore, the origin of the more pronounced decrease in the dewetting edge propagation distance in Ge-covered square SOI mesas relative to rectangular mesas is currently unknown as well. This interesting dewetting behavior in Ge-covered SOI films remains a very interesting subject for future study.

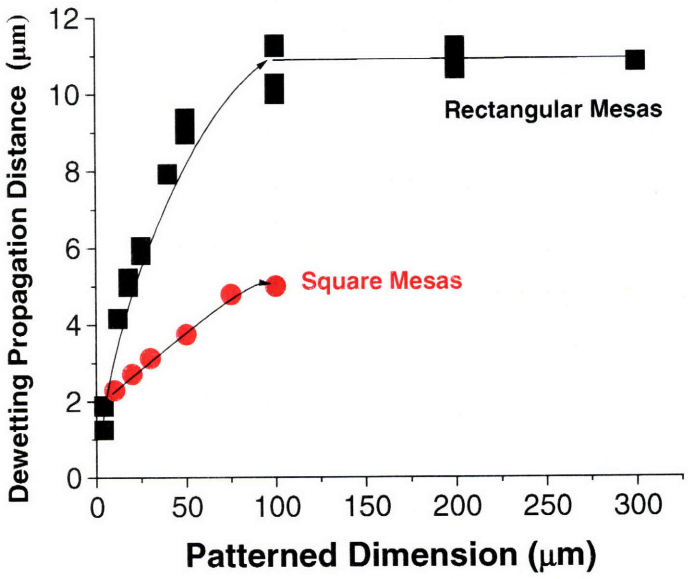

Figure B.9: Plot of the measured average edge dewetting propagation distance in etched <110>-edge-oriented Ge-covered 35n-thick SOI mesas annealed at 850C for 30min. A pronounced decrease in the edge dewetting propagation distance is observed below the same critical 50μm mesa width for which complete Ge island formation suppression and non-edge dewetting suppression was observed. The origin of this effect remains unknown and will be a subject of future study.

References

1 Y. Ono, M. Nagase, M. Tabe, and Y. Takahashi, *Japanese Journal of Applied Physics* **34,** 1728-35 (1995).

2 R. Nuryadi, Y. Ishikawa, and M. Tabe, *Applied Surface Science* **159/160,** 121-6 (2000).

3 R. Nuryadi, Y. Ishikawa, and M. Tabe, Reports of the Graduate School of Electronic Science and Technology, Shizuoka University, 111-15 (2001).

4 R. Nuryadi, Y. Ishikawa, Y. Ono, and M. Tabe, *Journal of Vacuum Science & Technology B* **20,** 167-72 (2002).

5 Y. Ishikawa, M. Kumezawa, R. Nuryadi, and M. Tabe, *Applied Surface Science* **190,** 11-15 (2002).

6 Y. Ishikawa, Y. Imai, H. Ikeda, and M. Tabe, *Applied Physics Letters* **83,** 3162-4 (2003).

7 Z. A. Burhanudin, R. Nuryadi, Y. Ishikawa, M. Tabe, and Y. Ono, *Applied Physics Letters* **87,** 121905-1 (2005).

8 Z. A. Burhanudin, R. Nuryadi, Y. Ishikawa, and M. Tabe, *Thin Solid Films* **508,** 235-238 (2006).

9 B. Legrand, V. Agache, J. P. Nys, V. Senez, and D. Stievenard, *Applied Physics Letters* **76,** 3271-3273 (2000).

10 B. Legrand, V. Agache, T. Melin, J. P. Nys, V. Senez, and D. Stievenard, *Journal of Applied Physics* **91,** 106-111 (2002).

11 C. Jahan, O. Faynot, L. Tosti, and J. M. Hartmann, *Journal of Crystal Growth* **280,** 530-538 (2005).

12 International Technology Roadmap for Semiconductors, 2006 Update, http://www.itrs.org (2006).

13 M. L. Hammond, *Semiconductor International* **27,** 51-2 (2004).

14 S. Coe, W. K. Woo, M. Bawendi, and V. Bulovic, *Nature* **420,** 800-803 (2002).

15 S. Dobrin, K. R. Harikumar, R. V. Jones, N. Li, I. R. McNab, J. C. Polanyi, P. A. Sloan, Z. Waqar, J. Yang, S. Ayissi, and W. A. Hofer, *Surface Science* **600,** L43-L47 (2006).

16 I. R. McNab and J. C. Polanyi, *Chemical Reviews* **106,** 4321-4354 (2006).

17 S. Dobrin, K. R. Harikumar, T. B. Lim, L. Leung, I. R. McNab, J. C. Polanyi, P. A. Sloan, Z. Waqar, J. S. Y. Yang, S. Ayissi, and W. A. Hofer, *Nanotechnology* **18** (2007).

18 L. Pavesi, L. Dal Negro, C. Mazzoleni, G. Franzo, and F. Priolo, *Nature* **408,** 440-444 (2000).

19 A. L. Giermann and C. V. Thompson, *Applied Physics Letters* **86,** 121903-1 (2005).

20 R. S. Wagner and W. C. Ellis, *Applied Physics Letters* **4,** 89-90 (1964).

21 M. Yudasaka, R. Kikuchi, T. Matsui, Y. Ohki, S. Yoshimura, and E. Ota, *Applied Physics Letters* **67,** 2477-2479 (1995).

22 M. Chhowalla, K. B. K. Teo, C. Ducati, N. L. Rupesinghe, G. A. J. Amaratunga, A. C. Ferrari, D. Roy, J. Robertson, and W. I. Milne, *Journal of Applied Physics* **90,** 5308-5317 (2001).

[23] J. Dufourcq, P. Mur, M. J. Gordon, S. Minoret, R. Coppard, and T. Baron, *Materials Science & Engineering C* **27,** 1496-1499 (2007).
[24] M. Kirkham, X. D. Wang, Z. L. Wang, and R. L. Snyder, *Nanotechnology* **18** (2007).
[25] W. H. Wang, T. H. Hong, and C. T. Kuo, *Carbon* **45,** 97-102 (2007).
[26] J. Y. Kwon, T. S. Yoon, K. B. Kim, and S. H. Min, *Journal of Applied Physics* **93,** 3270-3278 (2003).
[27] Y.-M. Chiang, D. P. Birnie, and D. W. Kingery, *Physical Ceramics: Principles for Ceramic Science and Engineering* (John Wiley & Sons, 1996).
[28] W. Ostwald, Lehrbruck der Allgemeinen Chemie **2** (1896).
[29] T. Young, *Philosophical Transactions* **1,** 65 (1805).
[30] D. J. Srolovitz and M. G. Goldiner, *JOM* **47,** 31-6 (1995).
[31] J. W. Gibbs, *On the Equilibrium of Heterogeneous Substances* (New Haven, 1878).
[32] W. W. Mullins, *Journal of Applied Physics* **28,** 333-339 (1957).
[33] W. W. Mullins, *Journal of Applied Physics* **30,** 77-83 (1959).
[34] D. J. Srolovitz and S. A. Safran, *Journal of Applied Physics* **60,** 255-60 (1986).
[35] R. H. Brandon and F. J. Bradshaw, Royal Aircraft Establishment (Farnborough) Technical Report 66095 (1966).
[36] E. Jiran and C. V. Thompson, *Journal of Electronic Materials* **19,** 23-28 (1990).
[37] E. Jiran and C. V. Thompson, *Thin Solid Films* **208,** 23-28 (1992).
[38] A. E. B. Presland, G. L. Price, and D. L. Trimm, *Surface Science* **29,** 435-46 (1972).
[39] A. E. B. Presland, G. L. Price, and D. L. Trimm, *Progress in Surface Science* **3,** 64-96 (1972).
[40] S. K. Sharma and J. Spitz, *Thin Solid Films* **67,** 109-16 (1980).
[41] S. K. Sharma and J. Spitz, *Thin Solid Films* **56,** 17-19 (1979).
[42] S. K. Sharma and J. Spitz, *Philosophical Magazine A* **41,** 209-17 (1980).
[43] S. K. Sharma and J. Spitz, *Journal of Materials Science* **16,** 535-6 (1981).
[44] S. K. Sharma and J. Spitz, *Thin Solid Films* **61,** 13-15 (1979).
[45] S. K. Sharma and J. Spitz, *Thin Solid Films* **65,** 339-50 (1980).
[46] R. Saxena, M. J. Frederick, G. Ramanath, W. N. Gill, and J. L. Plawsky, *Physical Review B* **72,** 115425-1 (2005).
[47] K. Sieradzki, K. Bailey, and T. L. Alford, *Applied Physics Letters* **79,** 3401-3403 (2001).
[48] H. L. Caswell, J. R. Priest, and Y. Budo, *Journal of Applied Physics* **34,** 3261-3266 (1963).
[49] H. L. Caswell and Y. Budo, *Journal of Applied Physics* **35,** 644-647 (1964).
[50] M. L. Gimpl, A. D. McMaster, and N. Fuschillo, *Journal of Applied Physics* **35,** 3572-3575 (1964).
[51] L. Bachmann, D. L. Sawyer, and B. M. Siegel, *Journal of Applied Physics* **36,** 304-308 (1965).
[52] W. M. Kane, J. P. Spratt, and L. W. Hershinger, *Journal of Applied Physics* **37,** 2085-2089 (1966).
[53] W. B. Pennebaker, *Journal of Applied Physics* **40,** 394-400 (1969).

[54] R. E. Hummel, R. T. DeHoff, S. Matts-Goho, and W. M. Goho, *Thin Solid Films* **78,** 1-14 (1981).
[55] R. R. Zito, W. S. Bickel, and W. M. Bailey, *Thin Solid Films* **114,** 241-255 (1984).
[56] I. Beszeda, I. A. Szabo, and E. G. Gontier-Moya, *Applied Physics A* **78,** 1079-1084 (2004).
[57] C. Lee, J. Meteer, V. Narayanan, and E. C. Kan, *Journal of Electronic Materials* **34,** 1-11 (2005).
[58] T. Vanypre, M. Cordeau, T. Mourier, W. F. A. Besling, J. C. Dupuy, and J. Torres, *Microelectronic Engineering* **83,** 2373-2376 (2006).
[59] C. Favazza, J. Trice, A. K. Gangopadhyay, H. Garcia, R. Sureshkumar, and R. Kalyanaraman, *Journal of Electronic Materials* **35,** 1618-20 (2006).
[60] F. Lai, L. Jing, L. Lin, L. Yongzhong, H. Zhigao, and C. Rong, *Applied Surface Science* **253,** 7036-40 (2007).
[61] A. E. B. Presland, G. L. Price, and D. L. Trimm, *Surface Science* **29,** 435-446 (1972).
[62] D. J. Srolovitz and S. A. Safran, *Journal of Applied Physics* **60,** 247-54 (1986).
[63] D. J. Eaglesham, A. E. White, L. C. Feldman, N. Moriya, and D. C. Jacobson, *Physical Review Letters* **70,** 1643-6 (1993).
[64] D. M. Follstaedt, *Applied Physics Letters* **62,** 1116-18 (1993).
[65] J. M. Bermond, J. J. Metois, X. Egea, and F. Floret, *Surface Science* **330,** 48-60 (1995).
[66] R. J. Asaro and W. A. Tiller, *Metallurgical Transactions* **3,** 1789-1796 (1972).
[67] M. A. Grinfel'd, *Sov. Phys. Dokl.* **31,** 831-834 (1986).
[68] H. Gao and W. D. Nix, *Annual Review of Materials Science* **29,** 173-209 (1999).
[69] R. Nuryadi, Y. Ishikawa, Y. Ono, and M. Tabe, *Journal of Vacuum Science & Technology B* **20,** 167-172 (2002).
[70] D. T. Danielson, D. K. Sparacin, J. Michel, and L. C. Kimerling, *Journal of Applied Physics* **100,** 10 (2006).
[71] Y. Bin, Z. Pengpeng, D. E. Savage, M. G. Lagally, L. Guang-Hong, H. Minghuang, and L. Feng, *Physical Review B* **72,** 235413-1 (2005).
[72] P. Sutter, W. Ernst, Y. S. Choi, and E. Sutter, *Applied Physics Letters* **88,** 141924-1 (2006).
[73] M. Schrems, T. Brabec, M. Budil., and H. Potz, in *Proceedings of the Internationational Conference on the Science and Technology of Defects in Semiconductors*, 1990 (Elsevier), p. 245.
[74] J. Vanhellemont and C. Claeys, *Journal of Applied Physics* **62,** 3960-3967 (1987).
[75] W. L. Winterbottom, *Acta Metallurgica* **15,** 303-310 (1967).
[76] A. Tiberj, B. Fraisse, C. Blanc, S. Contreras, and J. Camassel, *Journal of Physics: Condensed Matter* **14**, 13411-16 (2002).
[77] L. F. Giles, A. Nejim, and P. L. F. Hemment, *Electronics Letters* **29,** 788-9 (1993).
[78] D. K. Sadana, J. Lasky, H. J. Hovel, K. Petrillo, and P. Roitman, in *Proceedings of the 1994 IEEE International SOI Conference*, 1994 (IEEE), p. 111-12.
[79] C. V. Thompson, Presentation at SMA Research Conference, Singapore (2007).
[80] W. Kan and H. Wong, *Journal of Applied Physics* **97,** 043515-1 (2005).
[81] M. S. McCallum, P. W. Voorhees, M. J. Miksis, S. H. Davis, and H. Wong, *Journal of Applied Physics* **79,** 7604-7611 (1996).

[82] S. C. Jain, M. Willander, and H. Maes, *Semiconductor Science and Technology* **11,** 641-671 (1996).
[83] S. C. Jain, H. E. Maes, and K. Pinardi, *Thin Solid Films* **292,** 218-226 (1997).
[84] A. Atkinson, T. Johnson, A. H. Harker, and S. C. Jain, *Thin Solid Films* **274,** 106-112 (1996).
[85] C.-H. Hsueh, *Journal of Applied Physics* **91,** 9652 (2002).
[86] F. S. d'Aragona, *Journal of The Electrochemical Society* **119,** 948-951 (1972).
[87] J. W. Cahn, *Scripta Metallurgica* **13,** 1069-71 (1979).
[88] J. S. Stolken and A. M. Glaeser, *Scripta Metallurgica et Materialia* **27,** 449-54 (1992).
[89] C. Roland and G. H. Gilmer, *Physical Review B* **46,** 13428-36 (1992).
[90] Y. W. Mo, J. Kleiner, M. B. Webb, and M. G. Lagally, *Physical Review Letters* **66,** 1998-2001 (1991).
[91] Y. W. Mo, J. Kleiner, M. B. Webb, and M. G. Lagally, *Surface Science* **268,** 275-95 (1992).
[92] G. Brocks, P. J. Kelly, and R. Car, *Physical Review Letters* **66,** 1729-32 (1991).
[93] G. Brocks, P. J. Kelly, and R. Car, *Surface Science* **269-270**, 860-6 (1992).
[94] M. E. Keeffe, C. C. Umbach, and J. M. Blakely, *Journal of the Physical Chemistry of Solids* **55**, 965-73 (1994).
[95] A. V. Latyshev, A. B. Krasilnikov, and A. L. Aseev, *Physical Review B* **54,** 2586-9 (1996).
[96] R. E. Honig and D. A. Kramer, *RCA Reviews* **285,** 1610 (1969).
[97] M. Ichikawa and T. Doi, *Applied Physics Letters* **50,** 1141-3 (1987).
[98] A. V. Latyshev, A. L. Aseev, A. B. Krasilnikov, and S. I. Stenin, *Physica Status Solidi A* **113,** 421-30 (1989).
[99] R. F. C. Farrow, *Journal of The Electrochemical Society* **121,** 899-907 (1974).
[100] E. Kasper, *Applied Physics A* **A28,** 129-35 (1982).
[101] H. Kuribayashi, R. Shimizu, K. Sudoh, and H. Iwasaki, *Journal of Vacuum Science & Technology A* **22,** 1406-9 (2004).
[102] K. Sudoh, H. Iwasaki, H. Kuribayashi, R. Hiruta, and R. Shimizu, *Japanese Journal of Applied Physics* **43,** 5937-41 (2004).
[103] R. J. Jaccodine, *Journal of The Electrochemical Society* **110,** 524-527 (1963).
[104] D. J. Eaglesham and R. Hull, *Materials Science & Engineering B* **30**, 197-200 (1995).